NKS-287
ISBN 978-87-7893-362-1

Investigation of debris bed formation, spreading and coolability

Pavel Kudinov, Alexander Konovalenko, Dmitry Grishchenko, Sergey Yakush
Simone Basso, Nazar Lubchenko, Aram Karbojian

Royal Institute of Technology, KTH, Sweden

August 2013

Abstract

The work is motivated by the severe accident management strategy adopted in Nordic type BWRs. It is assumed that core melt ejected from the vessel will fragment, quench and form a coolable debris bed in a deep water pool below the vessel. In this work we consider phenomena relevant to the debris bed formation and coolability.

Several DEFOR-A (Debris Bed Formation – Agglomeration) tests have been carried out with new corium melt material and a melt releasing nozzle mockup. The influence of the melt material, melt superheat, jet free fall height on the (i) faction of agglomerated debris, (ii) particle size distribution, (iii) ablation/plugging of the nozzle mockup has been addressed.

Results of the DECOSIM (Debris Coolability Simulator) code validation against available COOLOCE data are presented in the report. The dependence of DHF on system pressure from COOLOCE experiments can be reproduced quite accurately if either the effective particle diameter or debris bed porosity is increased. For a cylindrical debris bed, good agreement is achieved in DECOSIM simulations for the particle diameter 0.89 mm and porosity 0.4. The results obtained are consistent with MEWA simulation where larger particle diameters and porosities were found to be necessary to reproduce the experimental data on DHF. It is instructive to note that results of DHF prediction are in better agreement with POMECO-HT data obtained for the same particles. It is concluded that further clarification of the discrepancies between different experiments and model predictions.

In total 13 exploratory tests were carried out in PDS (particulate debris spreading) facility to clarify potential influence of the COOLOCE (VTT) facility heaters and TCs on particle self-leveling process. Results of the preliminary analysis suggest that there is no significant influence of the pins on self-leveling, at least for the air superficial velocities ranging from 0.17 up to 0.52 m/s. Further confirmatory tests might be needed at lower gas injection rates.

Key words

Severe accident, Nordic BWR, debris bed formation, debris bed coolability

NKS-287
ISBN 978-87-7893-362-1
Electronic report, August 2013

NKS Secretariat
P.O. Box 49
DK - 4000 Roskilde, Denmark
Phone +45 4677 4041
www.nks.org
e-mail nks@nks.org

APRI-8, NKS-DECOSE

Report 1/2012

Investigation of debris bed formation, spreading and coolability

Pavel Kudinov, Alexander Konovalenko, Dmitry Grishchenko,
Sergey Yakush, Simone Basso, Nazar Lubchenko, Aram Karbojian

Division of Nuclear Power Safety
Royal Institute of Technology (KTH)
10691 Stockholm, Sweden

June 17, 2013
Stockholm

Contents

1 Introduction

1.1 Motivation and background

The project is motivated by Severe Accident (SA) Mitigation Strategy adopted in several designs of light water reactors (LWR) and specifically in Nordic type BWRs. The LWR SA management strategy considered hereafter is based on ex-vessel melt coolability in the reactor cavity filled up with water. It is assumed in the design that, in case of severe core melt accident, reactor pressure vessel (RPV) lower head can fail and molten core materials (corium) can be poured into a several meters deep reactor cavity filled with water. It is assumed further that decay heat can be removed from the debris bed by natural circulation. However, coolability of such bed is contingent upon the properties of the debris bed, such as particle size distribution, porosity and geometrical configuration of the bed. A tall, mound shape debris bed can be hardly coolable, while the same mass of the debris can be easily cooled if the bed is spread uniformly over the area of the reactor cavity [7], [10].

Generally, the SA management strategy has to be proven robust (insensitive to scenarios and conditions of melt release from the vessel). Yet, there is apparent significant influence of the accident scenario on the success of the SA management strategy. Specifically, melt release mode defines conditions and effectiveness of melt fragmentation, spreading and thus coolability. There are several characteristic modes of vessel failure and melt release that might result in completely different ex-vessel melt configurations. It is instructive to mention that even within one scenario of accident progression the melt is expected to be released in more than one shot with different (a) sizes of the vessel breach, (b) different melt compositions (oxidic or metallic), (c) melt superheats. Respective configuration of the debris bed can be completely fragmented particles (small vessel breach, small superheat of the melt), mixture of liquid and solid particles promoting formation of non-coolable “cakes” (medium size breach) and mostly liquid melt (large size breach, large melt superheat). A prove of the robustness of the management strategy implies systematic and consistent analysis of different scenarios of melt release modes, their consequences for the ex-vessel melt arrest and coolability and associated epistemic and aleatory uncertainties. It is expected that some melt release scenarios will result in formation of non-coolable debris configurations threatening containment integrity.

Although the strategy of melt quenching in a pool is known for decades and has been a subject for intensive research since ’80s, the main questions persist: whether or not decay heated porous debris bed can be cooled by natural circulation in the reactor cavity pool; and is there a threat to containment integrity due to energetic steam explosion, which can occur during melt pouring into water.

The APRI (Accident Phenomena of Risk Importance) research program was initiated at the Royal Institute of Technology (KTH) to help bring to the resolution the long standing severe accident issues: ex-vessel coolability and steam explosion for the Swedish-type BWRs. Advanced experimental infrastructure for tests with high melting temperature core melt simulant materials was developed at the division of Nuclear Power Safety (NPS) during last two decades with continuous support from Swedish nuclear power utility and safety authority. The focus of the previous APRI-7 (2009-2011) and current APRI-8 (2012-2016) at NPS-KTH is development of understanding and predictive capabilities for the debris bed formation and coolability phenomena in the process of melt pouring into coolant.

The research program on debris bed formation (DEFOR) carried out in the framework of APRI-7 projects includes experimental studies [28], [29], [30], [22], [32], [34], [21], [36], [37], [12], [33] in the DEFOR facility and comprehensive analytical research [48], [35], [13], [26], [23], [47], [50], [24], [49], [14], [27], [37], [38], [16], [25]. Sophisticated experimental techniques and multiphysics computational approaches were developed over the last years to understand and model the process of particle bed formation when a melt jet is released in a pool of water. The pool depth and water subcooling can be varied and so can be the melt jet height and the volume discharged into the water pool. The melt materials and compositions employed can be varied also, e.g. ceramic and glass type melts at temperatures up to 1500°C with different melt viscosities can be employed.

This work aims at further experimental investigation of the debris bed formation phenomena and resulting properties of the debris bed using new melt simulant materials at higher temperatures. We consider the effect of the jet free fall height on the particle size distribution and agglomeration. Potential ablation or plugging of the melt release nozzle is also addressed in this work.

Boiling and two-phase flow inside the bed is a source of mechanical energy which can help to flatten the debris bed by so called “self-leveling” phenomenon. However, to be effective in providing a coolable geometrical configuration, self-leveling time scale has to be smaller than the time scale for drying out and onset of re-melting of the bed.

COOLOCE facility at VTT [1], [2] has been used in the past for analysis of debris bed coolability. As a pool type facility, it can be used not only for analysis of coolability of different 2D and 3D geometries of the debris bed, but also for investigation of particulate debris spreading. However, there is a concern if presence of the vertical heaters and thermocouples can affect spreading of the bed.

In this work we clarify the concerns about the effect of the heaters and thermocouples on particulate debris spreading using PDS-C (particulate debris spreading closures) experiment at KTH with the same particles and mockups of heaters and thermocouples used in the COOLOCE facility.

DECOSIM is a thermo-hydraulic code being developed at KTH for simulation of debris bed formation and coolability [47], [48]. In the framework of this work, validation of DECOSIM code is being performed against the COOLOCE data.

2 Investigation of melt jet fragmentation, debris bed formation and melt-structure melt-coolant interactions in DEFOR-A facility

2.1 GOALS AND TASKS

The goal of the research project is to provide experimental data and develop analytical methods and approaches which can be used to facilitate technical decision making on development of general severe accident mitigation strategy for LWR in case of corium melt release through a breach in lower head into the flooded drywell. The emphasis is thus on the interaction of the melt with vessel lower head and debris bed formation.

The main tasks of the research project are to produce experimental data, and to develop and validate analytical models for assessment of:

i. Effectiveness of liquid melt jet fragmentation and debris bed formation in different conditions of
    i. melt release (jet diameter, free fall height etc.)
    ii. melt superheat
    iii. water subcooling
    iv. and water pool depth
ii. Radial, axial ablation and plugging of the nozzle (sample) for melt release.

In the following we provide the main results of the 4 new tests of the DEFOR-A series A10-A13. The review of the previous DEFOR-A01-09 tests can be found in [31], [32] and [33].

The DEFOR-A10 - A13 tests have been performed with new simulant material (ZrO_2-WO_3). Its application was mainly motivated by the need for the improvement of the melt fragmentation visualization: used in previous DEFOR-A tests mixture of Bi_2O_3-WO_3 as corium melt simulant produced an opaque cloud when interacting with water. The cloud was hindering observations of the melt jet fragmentation process and prevented observation of the debris bed formation.

Primary tasks of the DEFOR-A10-A13 tests are as follows:

i. Validate prototypic behavior of the new simulant material in terms of melt jet fragmentation and debris bed formation:
   - compare experimental data on debris bed agglomeration and melt jet fragmentation with previous DEFOR-A and DEFOR-S test results obtained with already validated Bi_2O_3-WO_3 simulant,
   - compare experimental particle size distribution with FARO tests results obtained on prototypic oxidic corium.

ii. Assess the effect of the melt jet free fall height on the particle size distribution.

iii. Assess the effect of the direct melt release into water (through a submerged conical shell) on the melt fragmentation and debris bed formation.

iv. Study axial and radial ablation of the immersed in water nozzle (sample) upon melt release.

v. Investigate possibility of melt freezing inside the sample and late nozzle plugging.

Task (i) and (ii) were addressed in the A10 and A11 tests respectively; remaining tasks (iii-v) were evaluated in tests A12 and A13.

2.2 EXPERIMENTAL FACILITY

DEFOR (Debris Bed Formation) facility was developed for studies of melt fragmentation, particle and debris bed formation and agglomeration in deep water pool.

The installation consists of (i) an induction furnace for melt generation, (ii) a funnel for melt deliver, (iii) a test section with optional metallic sample, and (iv) external water heating system. The scheme of the installation is given in the Figure 1a and Figure 3a. The furnace is composed of a (i) SiC crucible inductively heated with a 45kW medium-frequency (up to 30 kHZ) generator and (ii) an opened housing connected to a tilting mechanism for crucible leaning and melt delivery into the funnel.

The furnace can provide melting of corium simulant materials at temperatures up to 1600°C and melt volume up to 10 liters. It is equipped with three bottom thermocouples and one lateral thermocouple for temperature control.

The funnel is equipped with nozzle which allows jet diameters from 10 to 25 mm. A K-type thermocouple is positioned inside the nozzle for the temperature measurement of the delivered melt.

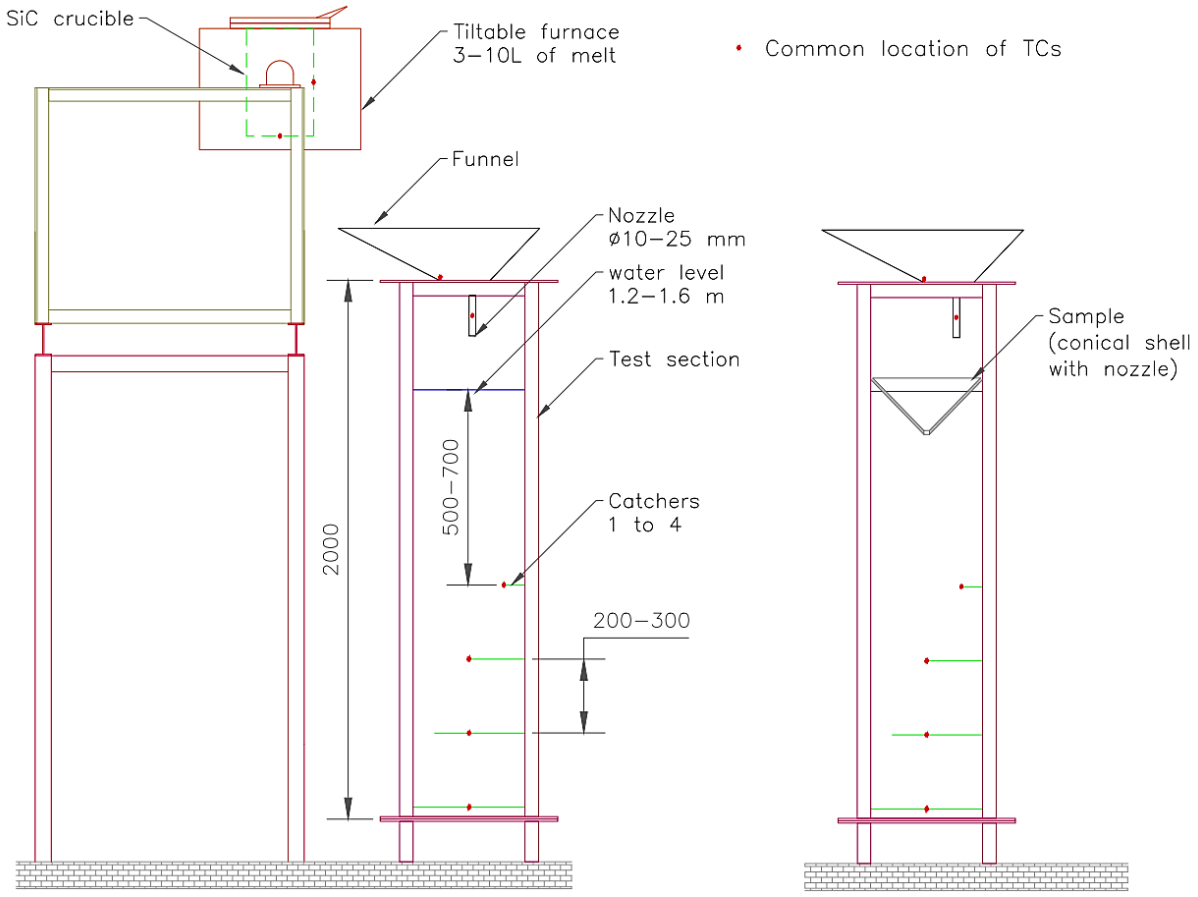

Figure 1: DEFOR experimental facility: a – common setup for DEFOR-A01-12; b – common setup for DEFOR-A12-13

The DEFOR test section is a vertical 2.0 m tank with approximately rectangular cross section 0.5x0.5 m filled up with tap water. The water for the tests is heated in an external tank to a predefined temperature and is poured into the test section shortly before the melt delivery.

Visual observation of the melt release and melt-coolant interaction is performed through a number of rectangular Plexiglas windows installed on lateral sides of the test section. Commonly up to five cameras are used to record the melt-coolant interaction, including a number of high-speed cameras with up to 735 frames per second.

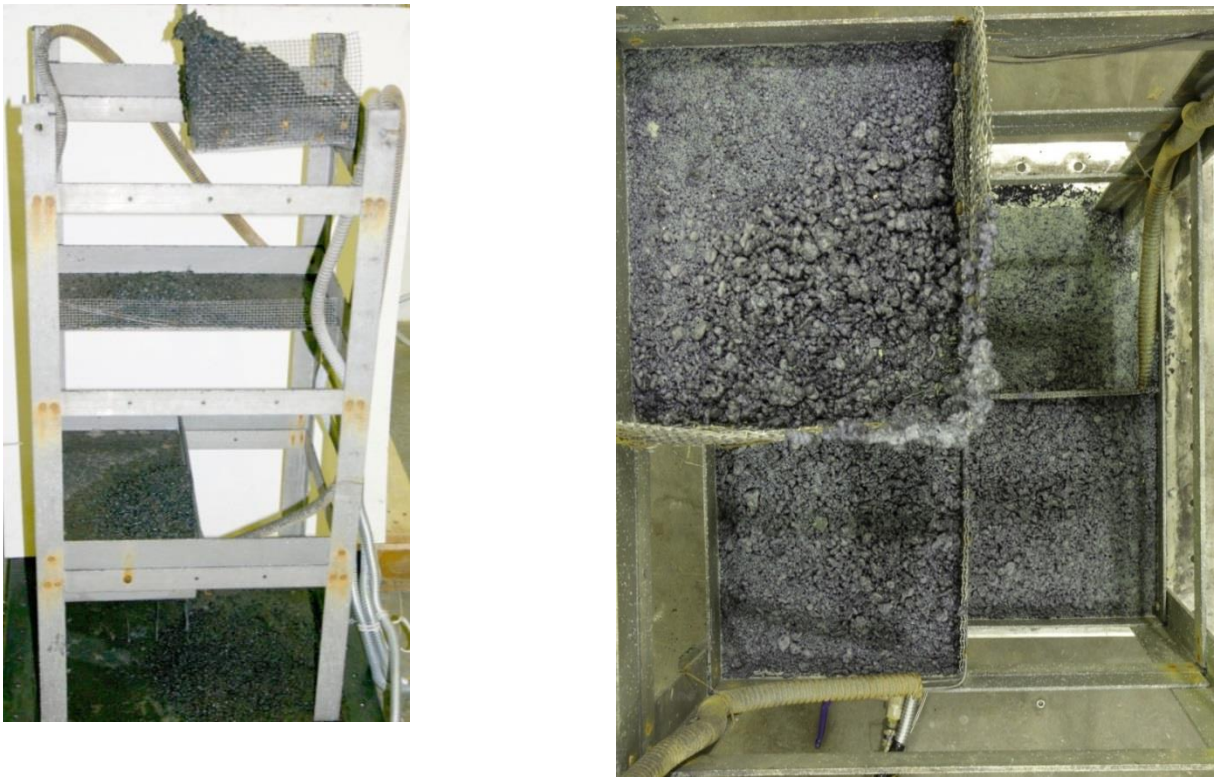

a b

Figure 2: DEFOR catchers with debris: a – side view; b – top view

Inside the test section 4 debris catchers are positioned at different elevations (Figure 2). Vertical location of the catcher can be adjusted according to test requirements. Each catcher is covering one of four quadrants of the test vessel cross section and collects melt fragments ejected from the jet. This allows assessment of the water pool depth on debris bed formation: agglomeration and local particle size distribution. The water pool depth and depth of the top catcher are chosen to ensure complete breakup of the melt jet. This is required to avoid the possible effect of the catchers on jet fragmentation and breakup length.

The water temperature inside the test section is measured along the walls at several elevations; the debris temperature is measured on every catcher by 2 thermocouples installed in the vicinity of the jet. In addition several TCs can be placed above the water level. The exact positioning and number of thermocouples varies from test to test.

The installation is placed inside a concrete containment for personnel safety (danger of steam explosion, melt splashes etc.) and is controlled remotely.

a b

Figure 3: DEFOR-A experimental setup without (a) and with (b) sample

In the DEFOR-A12-13 configuration (Figure 1b and Figure 3b) a test sample is installed at the top of the water pool to study (i) wall and nozzle ablation during melt release and (ii) effect of melt release directly into water on resulting debris size distribution and agglomeration. The test sample is designed as a conical shell with 90 degree angle and with single hole at the bottom (apex). Being partially immersed into water and provided 45° inclination angle of the lateral surface allows efficient heat removal due to intense natural convection flows increasing the critical heat flux limit in comparison with a not-inclined (horizontal) surface.

The material of the sample (lead) has melting temperature (327°C) lower than that of the melt (870°C or 1231°C), but higher than Leidenfrost temperature to allow for dryout on the wall. The difference between melting temperatures of the melt simulant and the sample material is 540°C for Bi_2O_3-WO_3 and 1000°C for ZrO_2-WO_3 eutectic mixtures respectively.

After each test the debris beds from every catcher undergo systematic analysis for debris bed topology, total porosity, agglomerated vs non-agglomerated mass, mass of cake and particle size distribution. The obtained data is than plotted as a function of catcher depth and compared to other tests in terms of the melt superheat, water subcooling, melt release conditions and melt material.

Ranges of varied experimental parameters of the whole DEFOR-A series are summarized in Table 1.

Table 1: Ranges of the DEFOR-A tests parameters

Parameter	Unit	Range
Test section parameters		
Pool depth: H_{pool}	m	1.1-1.75
Water temperature	°C	70 – 93
Debris catchers	-	4 catchers installed at different elevations inside the test section
Melt parameters		
Material and meting temperature	-	ZrO_2-WO_3 (eutectic), 1231°C; Bi_2O_3-WO_3 (eutectic), 870°C

Melt superheat	°C	50-200
Melt volume	liters	3-6
Jet free fall height: H_j	m	0.2-0.9
Jet diameter: D_{jet}	mm	10 – 25
Sample parameters		
Sample geometry	-	Conical shell with a nozzle at the tip of the cone
Initial conditions inside the sample	-	Wet (filled with water through open nozzle);
Sample material and melting temperature	°C	Lead, 327°C
Base diameter of the sample	mm	400 mm
Free volume inside the sample	liters	8.4
Water pool depth in the sample:	mm	150
Water pool volume	liters	3,5
Sample wall thickness	mm	5 – 20
Sample nozzle diameter	mm	5 – 30

2.3 RESULTS AND DISCUSSION

2.3.1 DEFOR-A10-A13 tests conditions and parameters

The experimental tests conditions are summarized in Table 2. In all tests 20.6 kg (~3 liters) of ZrO_2-WO_3 eutectic mixture was melted and delivered into 25 °C subcooled water through a ∅20 mm nozzle. The 25°C water subcooling has been chosen based on previous experience so that fracture of solidified debris upon quenching (due to thermal stress) could be avoided and resulting particle size distributions of the debris was representative of that established in liquid melt fragmentation and solidification regime.

In A10 and A11 tests the melt was released into the water pool; two experimental parameters were varied: melt superheat and jet entrance velocity. In the A10 test the actual melt superheat was 150 °C and free fall height was 20 cm; in A11 these values were 102°C and 70 cm respectively.

The increased free fall height has been established by decreasing the water level in the DEFOR test section by 50 cm. This also required shifting of the debris catchers with respect to the water surface, except for the top one, which position (depth with respect to the free surface) has been preserved.

Table 2: Experimental parameters of DEFOR-A tests

Parameter		DEFOR-A tests			
		A10	A11	A12	A13
Melt material		ZrO_2-WO_3 (eutectic)			
Eutectic melt composition (mass fraction, %)		16.43%-83.57%			
Melt parameters					
Initial melt volume, liters		3	3	3	3
Initial melt mass, kg		20.6	20.6	20.6	20.6
$T_{eutectic}$, °C		1231	1231	1231	1231
Maximal melt temperature in the funnel, °C		1371	1333	1345	1293
Actual melt superheat, °C		150	102	114	62
Pool parameters and experimental conditions					
Jet free fall height, m		0.2	0.7	0.13	0.13
Initial water temperature, °C		75	75	75	75
Final water temperature, °C		91	89		
Water pool depth H_{pool}, m		1.55	1.1	1.85	1.85
Jet diameter D_{jet}, mm		20	20	20	20
H_{pool}/D_{jet}		75	55	75*	150*
Estimated melt jet velocity near water surface, m/s		~2	~4	~1	~1
Pouring time, s		~13	~12	~11**	6.4**
Debris catchers					
Number of catchers		4	4	4	4
Catchers elevations (water depths), cm	C1: C2: C3: C4:	90 (65) 60 (95) 30 (125) 0 (155)	45 (65) 30 (80) 15 (95) 0 (110)	120 (50) 80 (90) 40 (130) 0 (170)	120 (50) 80 (90) 40 (130) 0 (170)
Sample parameters					
Geometry		-	-	Conical shell	
Initial conditions inside the sample		-	-	Wet***	
Material and melting temperature, °C		-	-	Pb, 327	
Difference between melting temperature of the sample material and melt maximum temperature, °C		-	-	1018	966
Base innner diameter, mm		-	-	400	
Wall thickness, mm		-	-	10	5
Outlet diameter, mm		-	-	20	10
Capacity, liters		-	-	8.36	
Water pool depth inside the sample, mm		-	-	150	
Water pool volume inside the sample, liters				3.53	

*estimated with respect to the diameter of the sample outlet and its elevation; **duration of melt release from the sample; ***Wet: filled with water through open nozzle;

The common for DEFOR-A12 and A13 test assembly is demonstrated in Figure 4. Note that water is not yet supplied into the DEFOR test section, its level is supposed to reach ~2/3 of the test sample cone height. The sample is placed inside the DEFOR test section and fixed by four stainless steel 10 mm thick holders (Figure 4c). The outlet of the sample is aligned with the test section vertical axis. The funnel for delivery of melt into the sample is placed above it in a way that the jet is shifted from the center of the sample and melt impingement point is on the underwater part of the sample conical wall.

In the Figure 5 the detailed designs of two samples manufactured for A12 and A13 tests respectively are provided. Main difference in samples geometry is in the nozzle diameter and wall thickness. Other geometrical parameters have been preserved the same. For A12 test the test sample has been manufactured with thick 10 mm walls and large 20 mm outlet diameter (the same as used in the funnel for melt delivery). Such configuration is expected to be more resistant to the wall ablation while enlarged nozzle diameter should provide easier melt release decreasing the duration of melt residence time in the sample and thus decreasing possibility of nozzle plugging. For A13 test, sample has been manufactured with thinner 5 mm walls and decreased 10 mm outlet diameter. Such configuration favors longer melt residence time, provides decreased sample to melt mass ratio speeding up sample heat up during interaction. Also thinner wall is more susceptible to onset of dryout.

Following some of the LWR designs (which implies wet cavity) the test sample is partially immersed into water (including melt impingement point). Water reaches 150 mm level measured from the sample outlet and is 130 mm away from the funnel nozzle outlet.

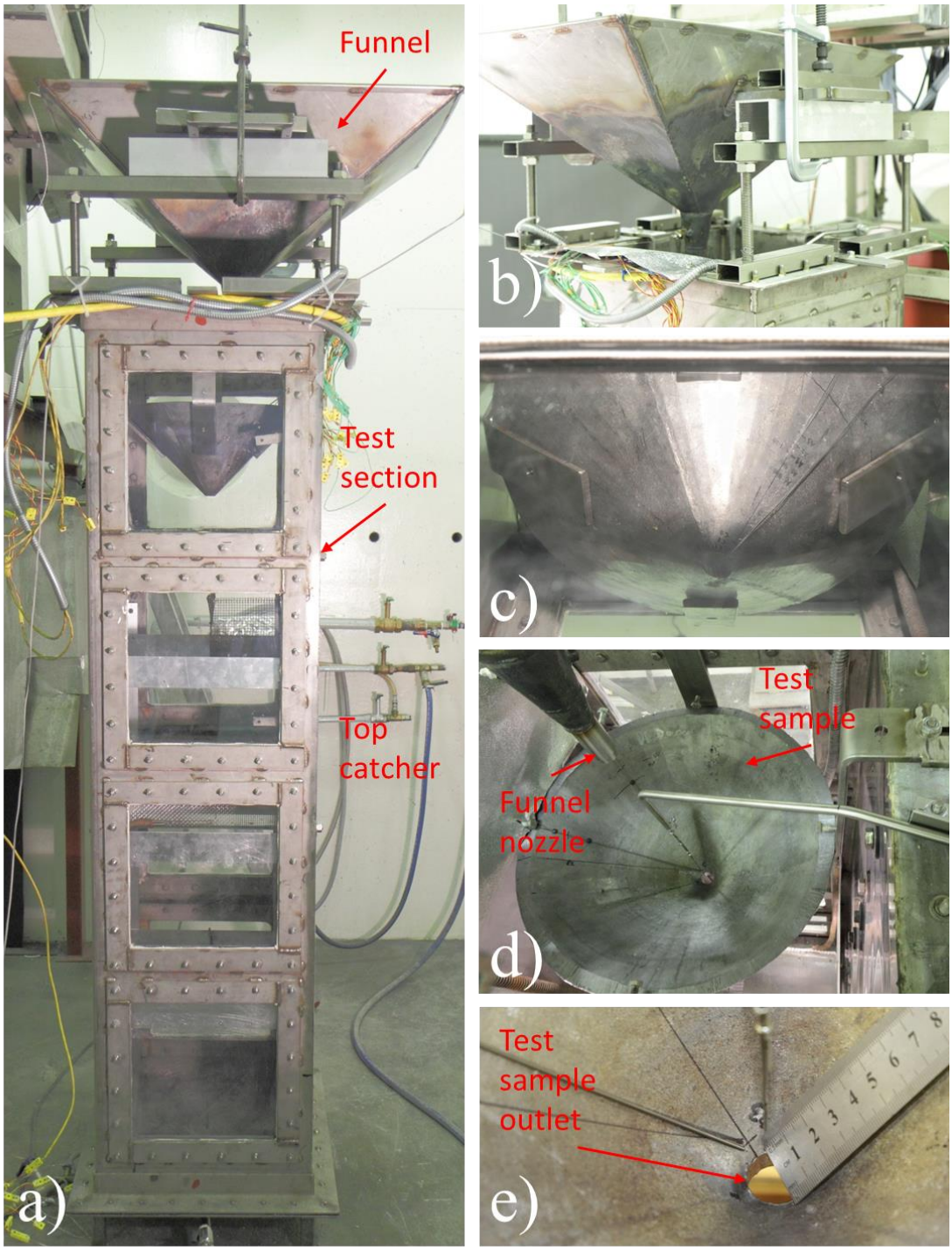

Figure 4: Common for DEFOR-A12 and A13 tests assembly (by example of the A12 test): general view (a), funnel (b) and melt granulation device (c-e) bottom, top and inside views respectively.

Several groups of thermocouples have been installed in the sample: around melt impingement point, around outlet and inside the water pool along the vertical axis. The junctions of the outside superficial TCs have been peened into the conical sample as close as possible to the

surface, while the inside TCs have been flushed to the surface (see below Figure 6 for illustrations). The bodies of the TCs have been secured by feeding through rivets or screws fixed around the circumference of the sample above the water level.

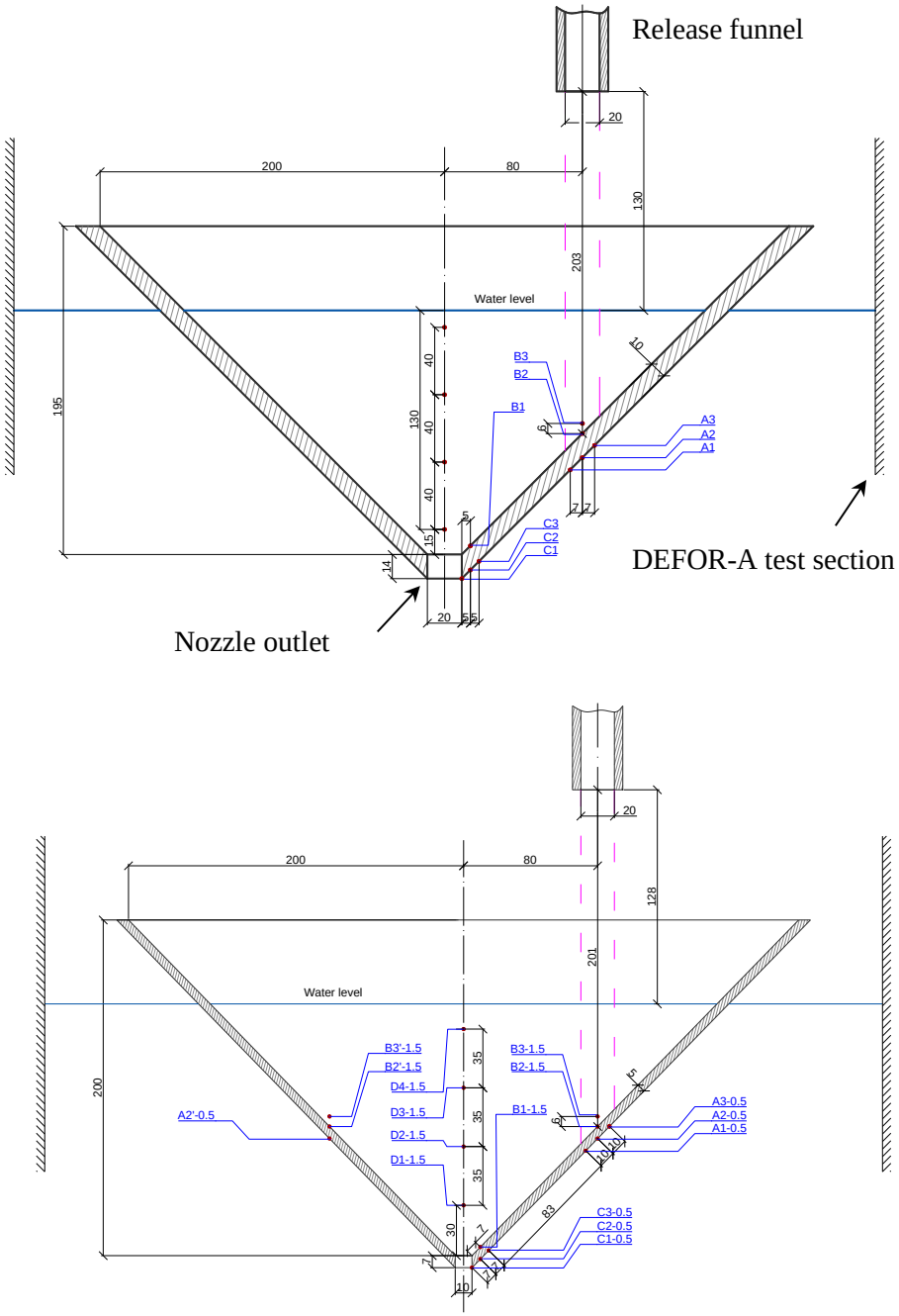

Figure 5: Design and instrumentation of the test sample in A12 (top) and A13 (bottom) tests

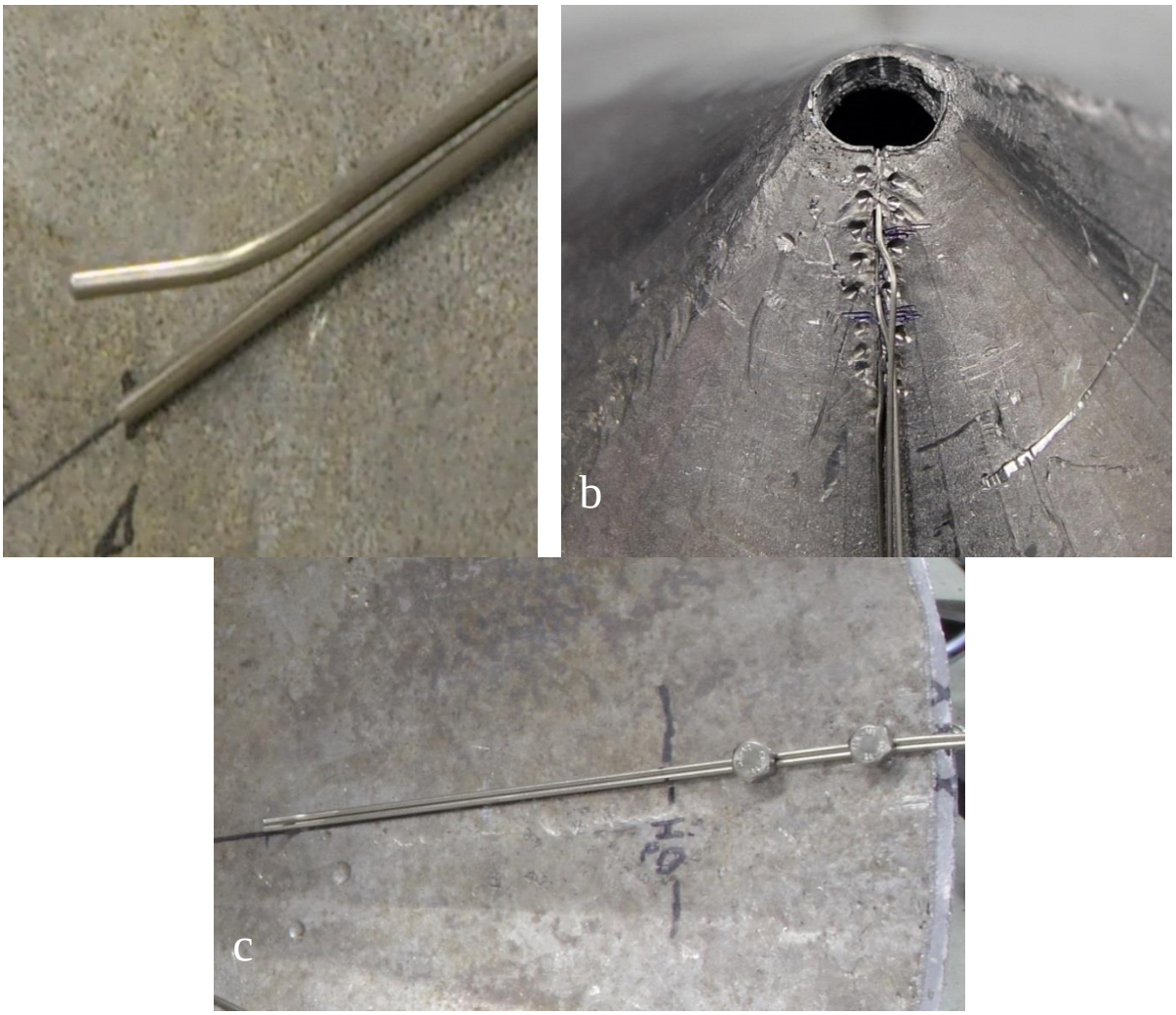

Figure 6: Setup of TCs inside the test sample common for A12 and A13 tests: a – B2 and B3 TCs; b – C1-C3 TCs; c – TCs feeding through screws fixed in the sample wall.

The TCs flushed to the outer surface are ∅0.5 mm and those in direct contact with the melt are ∅1.5 mm. Notice that B3 thermocouple is bended 6 mm upward from the surface to measure the temperature of the impinging jet. Also notice that in A13 test 3 TCs: B2', B3' and A2' have been added symmetrically to B2, B3 and A2 for comparison.

2.3.2 Melt pouring

DEFOR A10 and A11 tests

In A10-11 tests melt release took around 12-13 sec. Out of 20.6 kg of the initial melt charge, in A10 test 17.08 kg of melt has been delivered into water, in the A11 this value has been somewhat smaller 13.39 kg. The difference can be attributed to the lower melt superheat in the A11 test.

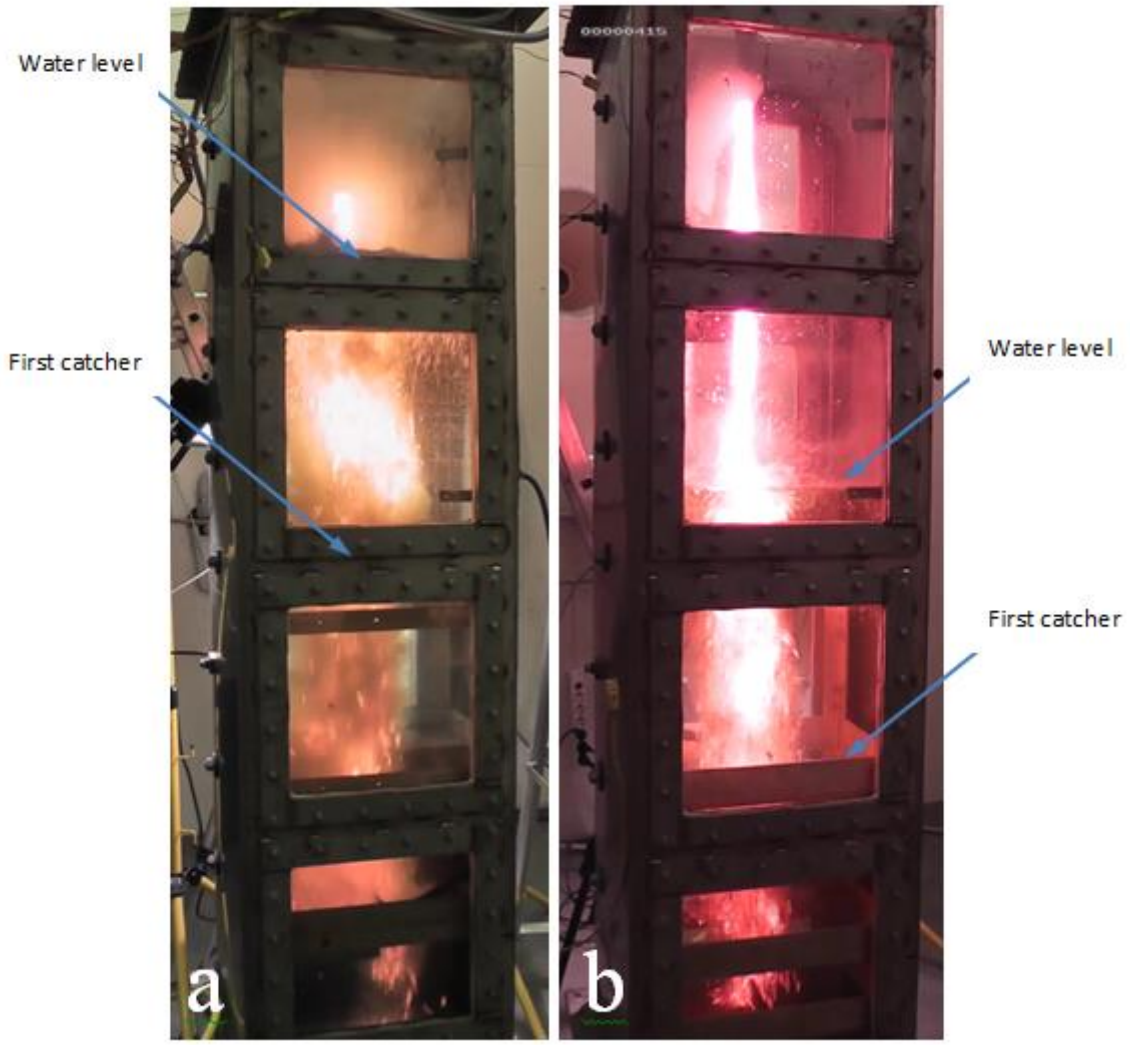

Figure 7: Melt pouring in A10 (a) and A11 (b) tests

Note that due to different melt masses delivered into the test section, the melt to water mass ratio has been preserved almost the same in both tests: 0.044 in A10 and 0.049 in A11. This allowed for similar temperature evolution of the bulk water during melt release providing similar values of water temperature after the test 91 and 89 °C respectively.

Comparison of melt delivery into water for A10 and A11 is provided in the Figure 7. In both snapshots a straight and coherent jet can be seen above the water level as well as its fast break up and fragmentation upon entrance into water.

The melt front velocity at the initial water level (estimated assuming free fall acceleration from the nozzle outlet) is at least 2.0 and 3.7 m/sec for A10 and A11 tests respectively. The

corresponding jet diameter (by mass conservation) is ~2 and ~1.5 cm. Thus, expected jet breakup level is above the level of the top catcher in both tests.

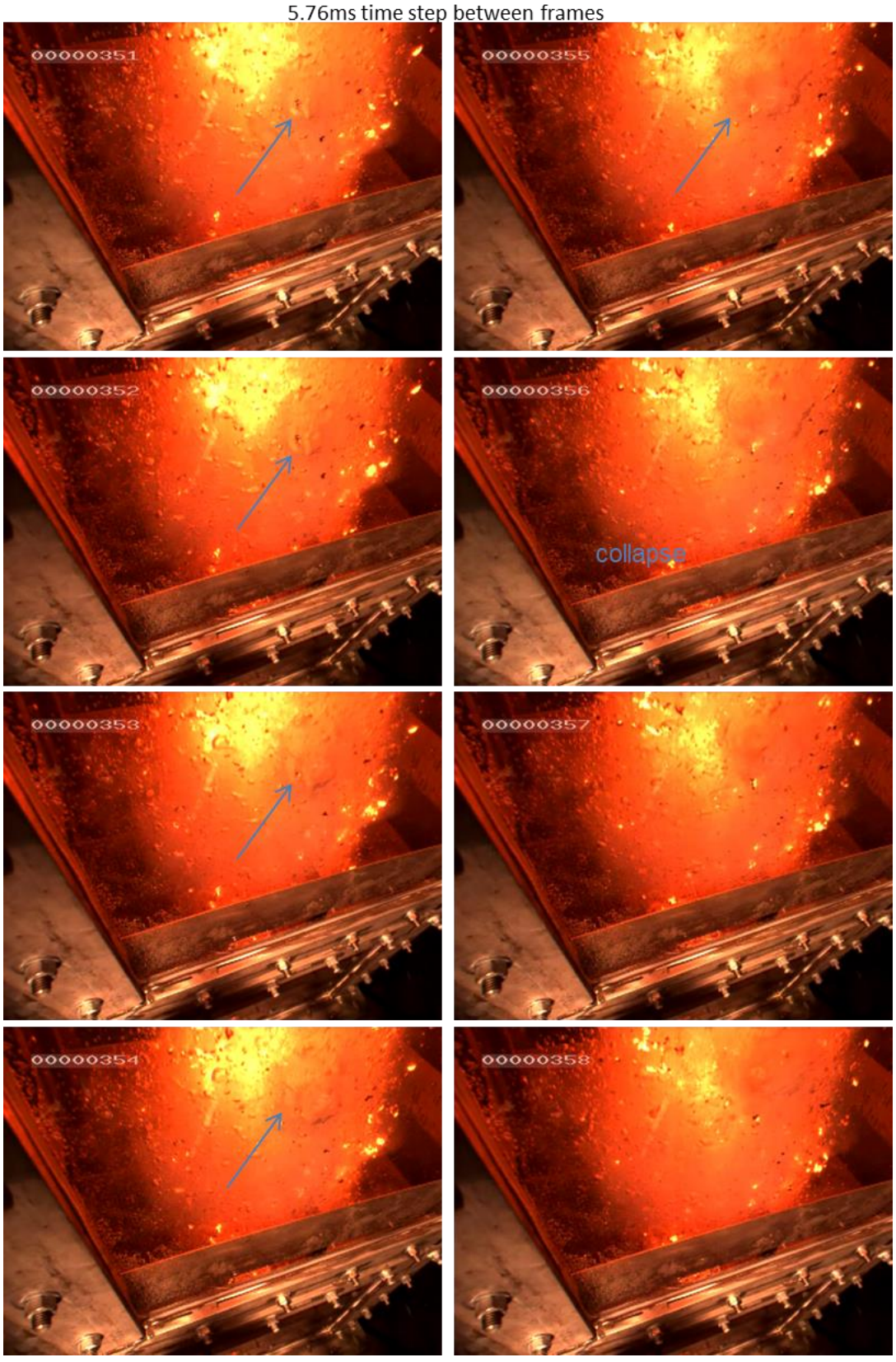

Figure 8: Three phase melt-water-steam dynamics recorded in A11 test at the top catcher by fast camera (170 fps).

During the pouring process, considerable vibrations of the DEFOR test section walls have been observed. The periodic “bulging” of the test section walls is attributed to the effect of dynamic growth and collapse of the vapor bubbles, phenomena common for boiling or steam injection into subcooled water.

Improved visualization due to application of the new melt simulant allows verification of this hypothesis. The dynamics of bubble growth and collapse is shown in the Figure 8. Growth of a bubble starts around a hot fragment or next to the melt puddle where local water temperature is close to the saturation point. Once the buoyancy exceeds surface tension forces that keep the bubble attached to the heat source, the bubble starts to move upward. Small bubbles merge together into large bubbles. Since the heat source is no more supplying energy to the bubble, the steam rapidly cools down. Due to subcooled state of surrounding water the condensation process rapidly develops leaving virtually an empty bubble at absolute pressure close to zero. Driven by the surrounding pressure the bubble collapses. Converging flow of water develops a pressure pike behind the moving interface.

By video recordings we could estimate that characteristic time of steam bubble collapse is quite short while the size is quite large (~10 ms and ~10 cm respectively). During the rapid bubble collapse, water is accelerated inwards at the velocity of about 10 m/s and collides closing the void left from the condensed steam.

It is instructive to note that dynamics of individual bubbles growth/collapse events in rather confined geometry of the DEFOR test section are affected by neighboring bubble growth/collapse events and thus become correlated.

DEFOR-A12 and A13 tests

Application of the lead (Pb) sample has significantly affected the duration of the melt release. Out of initial 20.6 kg of the load, in A12 test 15.32 kg of melt has been delivered into the water (including 2.35 kg solidified inside the sample) within 34 sec – duration almost 3 times longer than in previous A10 and A11 tests (12-13 sec). In contrast, in the A13 test melt delivery has been interrupted 6.3 seconds later after the start of the release. Mass of solidified inside the sample melt is 5.7 kg and only a small portion of 1.04 kg has been collected from

the catchers. About 12.1 kg of melt was found in the melt delivery funnel. The difference between melt delivery in A12 and A13 is surely due to the low melt superheat in the A13 test (64 °C) resulting in early plugging of the sample. It is interesting to note that despite lower melt superheat in A13 test melting through of the test sample wall occurred providing additional opening for the melt release.

At the very beginning of the melt release the jet released from the test sample is slightly inclined due to horizontal momentum obtained by the flow inside the sample (see for example Figure 9a and Figure 10a for A12 and A13 tests respectively). Later the release stabilizes, forming vertical coherent jet, slightly pulsating in case of the A13 test due to smaller jet diameter.

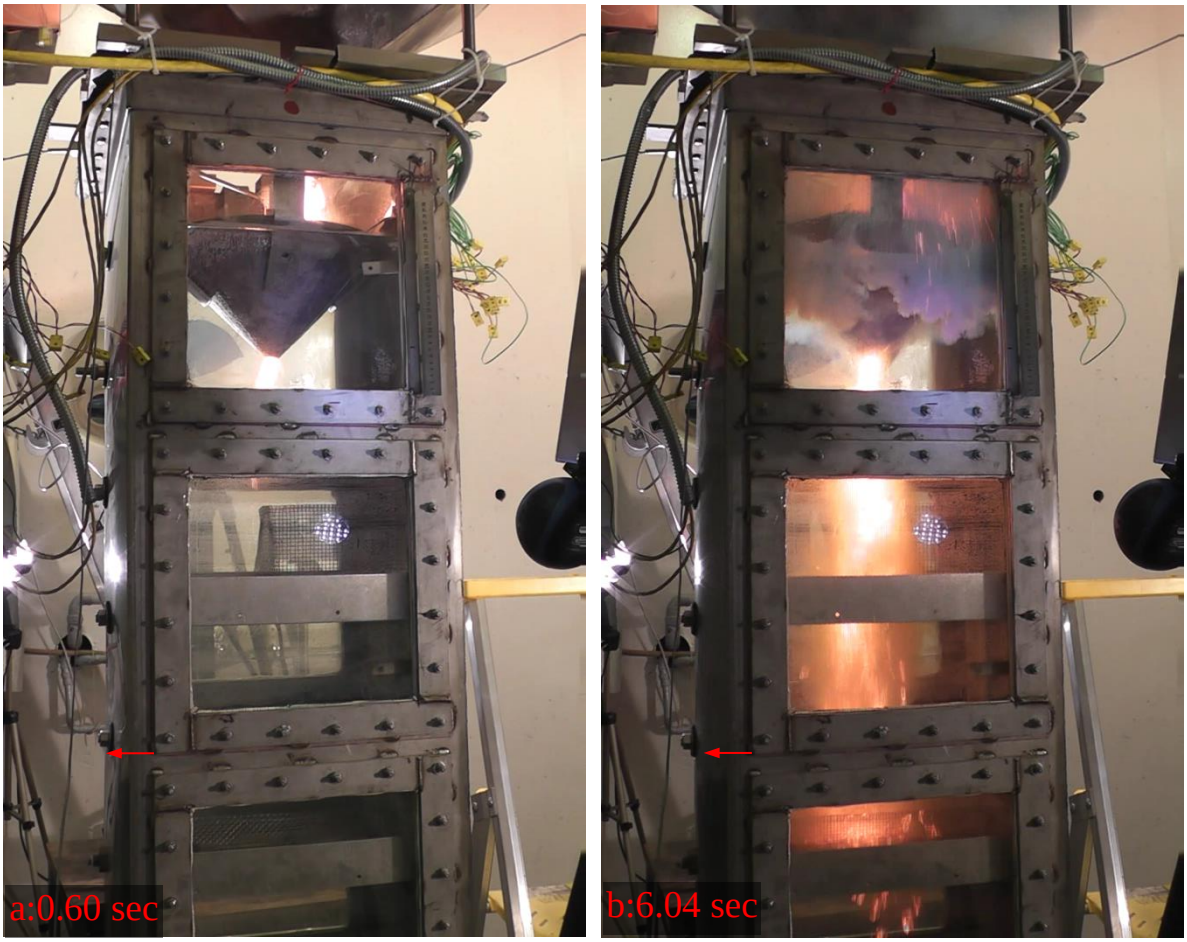

Figure 9: Melt release in A12 test (time stamp in the images is relative to the start of melt release from the test sample)

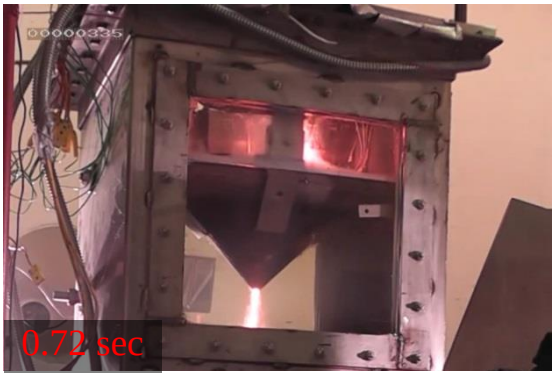

a)

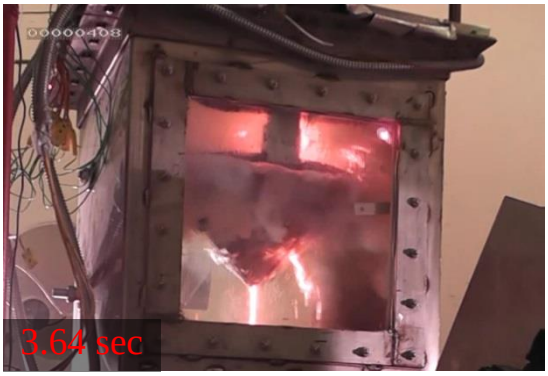

e)

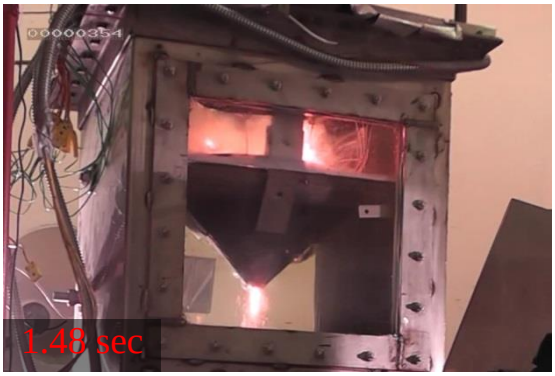

b)

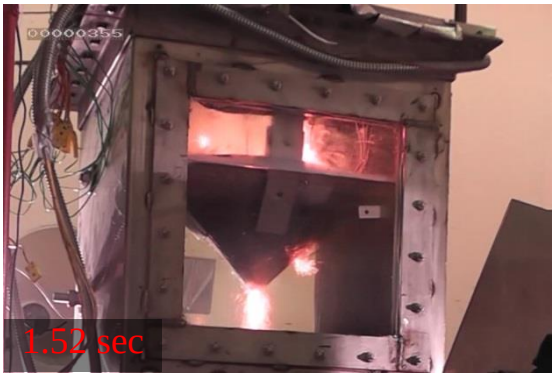

c)

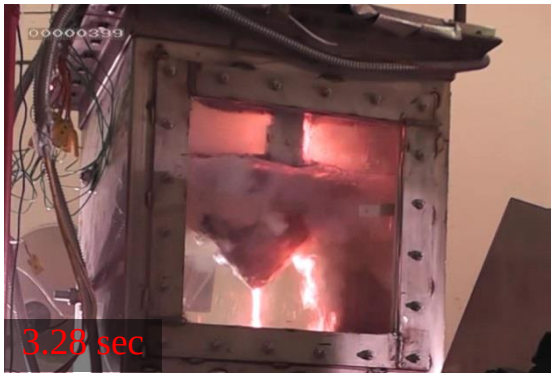

d)

f)

Figure 10: Melt release in A13 test (time stamp in the images is relative to the start of melt release from the test sample) (frame 308).

In A12 test the melt-water interactions are more intense compared to the A10 test. Periodic bulging (notice red arrow in the Figure 9a and Figure 9b) and even shaking of the DEFOR test section has been observed. Such behavior can be attributed to the effect of the test sample which partially confines the water pool in the test section. Nucleate boiling regime has been established below the melt impingement point at 1.38 sec after the melt release from the sample, no film boiling could be seen on the video footages. After the 34 sec of the release the test sample has been plugged.

In the A13 tests the melt-water interaction has been more moderate (Figure 10a and Figure 10f) in terms of bulging and shaking of the test section, which is attributed to the decreased instantaneous amount of melt in the premixture. After around 1.02 sec (from the start of the melt release from the sample) film boiling is established below the melt impingement point. Just 0.44 sec later a melt splash is observed inside the sample (Figure 10b) followed by (at 1.46 sec) melt through of the sample wall (Figure 10c). The melt jet released through the ablated hole in lateral direction is disturbed by rising convective flows and by the evolution of the melting-through geometry (Figure 10d and Figure 10f). Melt release continued only for 6.26 sec. At first the lateral jet has been plugged (at 5.58 sec) and shortly after that, the melt release from the sample nozzle was stopped.

2.3.3 Posttest debris analysis

The comparison of the debris beds established in DEFOR- A10-A13 tests is shown in Figure 11. Size of the debris particles in DEFOR-A10 (at least at the top catcher) is apparently bigger than that in the A11 test indicating higher fraction of the agglomerated debris. Notice that little amount of debris collected in A13 is insufficient to provide statistically reliable data on the debris agglomeration, total porosity and particle size distribution.

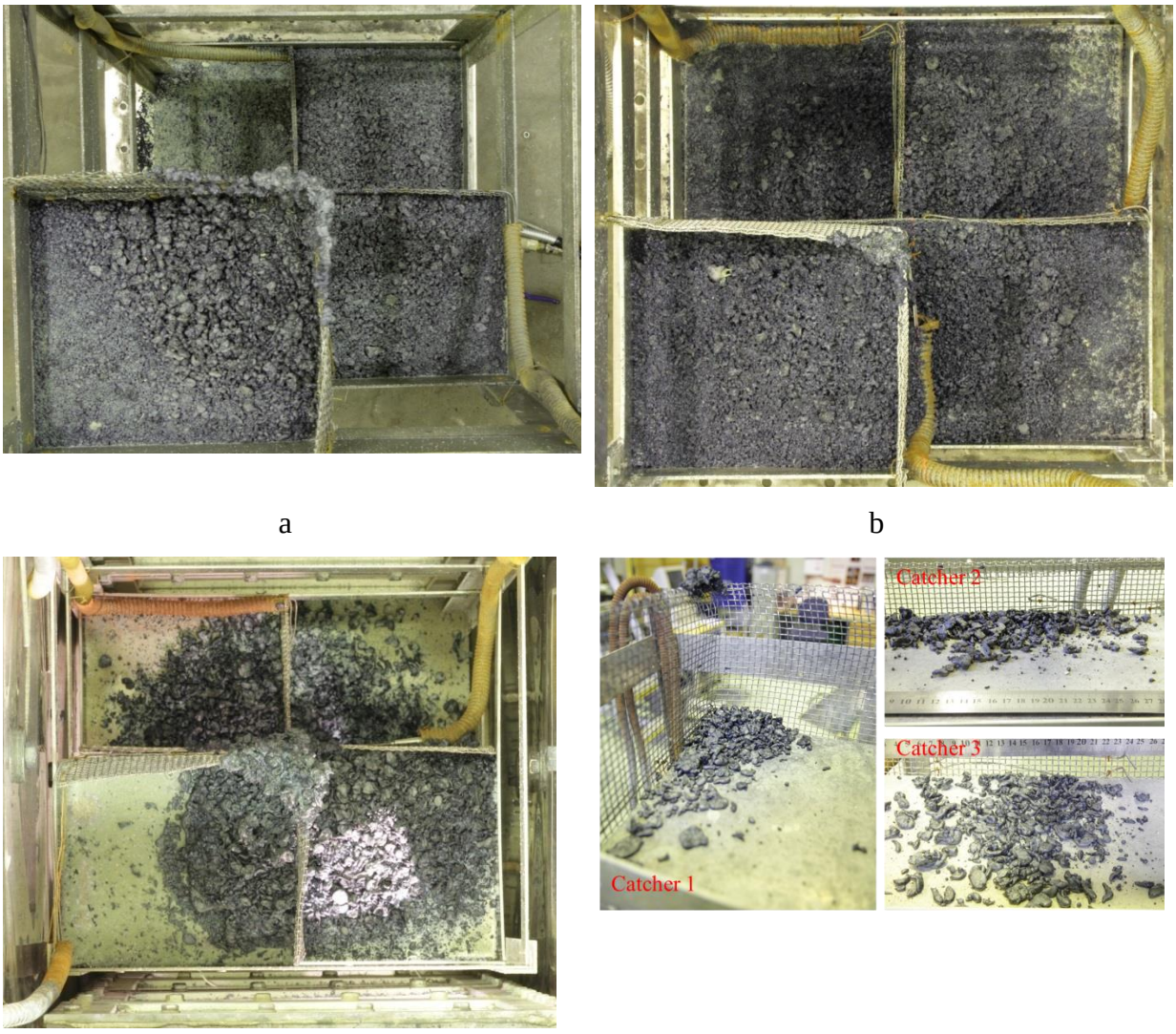

a b

c d

Figure 11: Debris beds in A10 (a), A11 (b) , A12 (c) and A13 (d) experiments

In general, morphology of the fragmented debris in A10-11 tests appeared to be very similar, in spite of the differences in agglomeration and size. The debris are characterized by relatively large agglomerated pieces, moderate size solidified cakes, roundish closed and opened hollow particles and absence of the cracked particles. The latter indicates that thermal stresses induced on the fragments upon quenching in water at 75 °C have been small enough not to alter the particle size distribution established in the liquid state during jet fragmentation. Thus only agglomeration phenomenon can alter the final particle size distribution.

Remarkably bigger particles can be seen in case of the A12 test, as well as apparently larger amount of the agglomerates. Comparison of the photographic images of the debris beds from each catcher in A12 and A10 tests (clarify Figure 12) leads to the same conclusion.

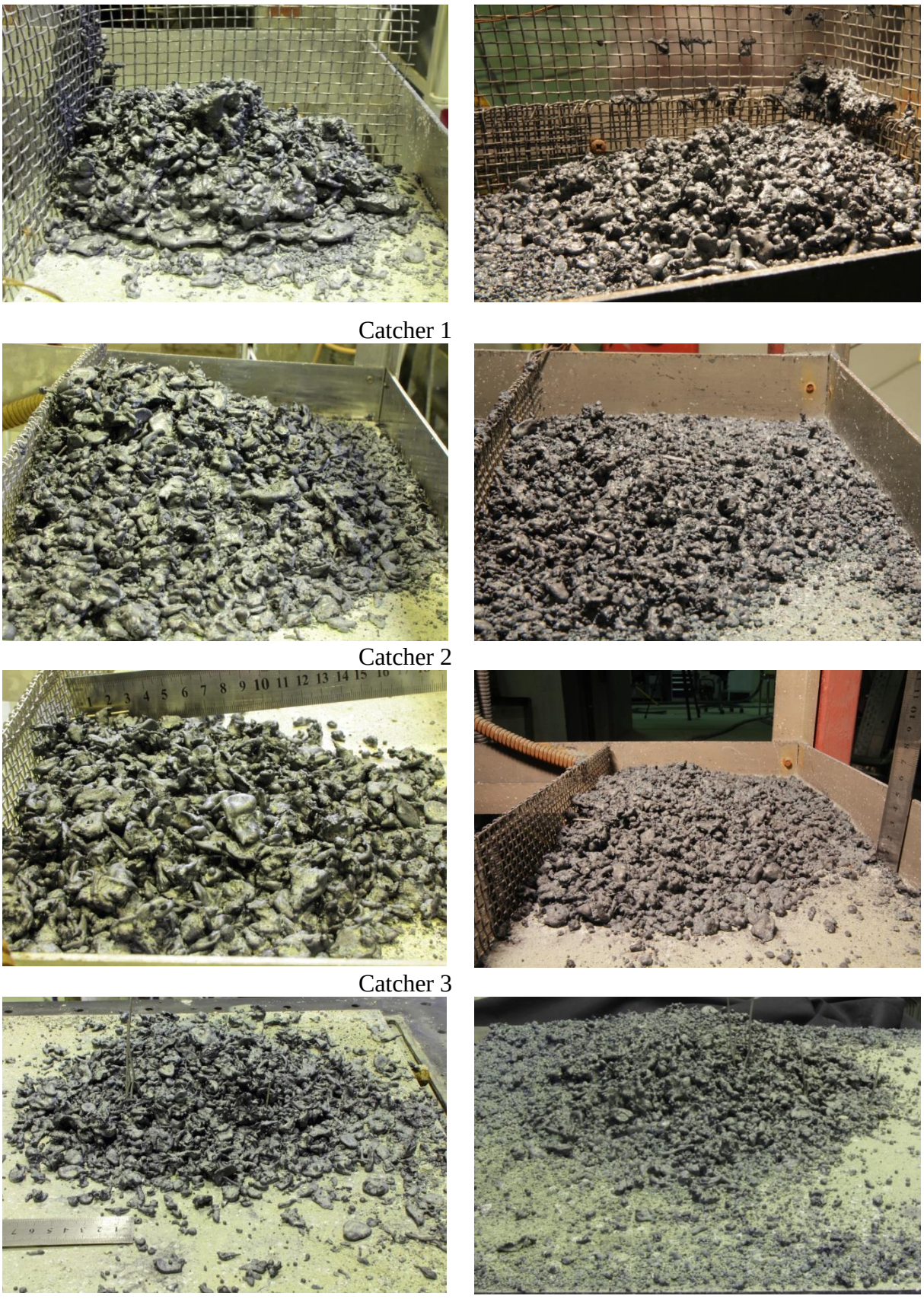

Catcher 1

Catcher 2

Catcher 3

Catcher 4

Figure 12: Debris beds in A12 (left) and A10 (right) catchers 1 (top) to 4 (bottom)

Another visual observation is that in A12 test number of small particles (~1 mm) is much less than in A10. Significant mass of agglomerated debris has been observed on the first catcher in A12. A thick layer which consists of agglomerates along with relatively large (about 1 cm) particles has been found atop of the solid cake in catcher-1. Some agglomerated debris but no cake were found in catcher-2.

The morphology of the fragmented debris in A12-13 is noticeably different from those found in A10-11 tests. Comparison of the debris fragments from the bottom catchers of A12 and A10 is provided in Figure 13. Neither fractured particles, nor considerable agglomeration of the fragments was observed in all tests on the bottom catcher.

Figure 13: Debris morphology at the bottom catcher in the tests A10 (left) and A12 (right)

As seen from these images in addition to typical round, elongated and irregular shapes we also observe relatively large oblate particles. Such particles are clearly seen in all catchers (Figure 12). Apparently application of the conical sample slows down melt release velocity and changes melt breakup mode. Decreased velocity decreases drop Weber number. Smaller Weber number increases the size of a stable droplet. Consequently larger droplets (i) require longer time for solidification, (ii) do not preserve round shape during sedimentation. Therefore we observe (i) higher fraction of agglomerates at the first catcher and (ii) oblate particles on lower catchers.

In the Figure 14 the results of the debris bed total porosity measurements are provided as a function of the pool depth (catcher elevation from the initial water level). Other debris bed parameters are detailed in the Table 3.

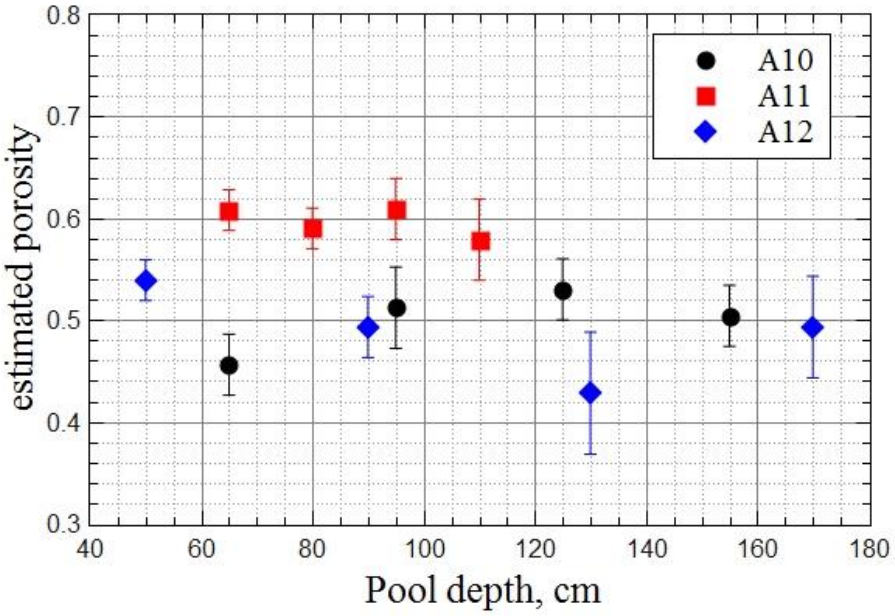

Figure 14: Volumetrically estimated total debris porosity per catcher in DEFOR-A10 and A11 tests.

The difference in total porosity between the catchers within one experiment is insignificant to draw any solid conclusion with respect to the possible dependence of the pool depth on porosity.

However, as the fraction of agglomerated debris rapidly decreases with the water depth (Figure 15), one would expect porosity to change as well. In reality agglomeration of the debris has a more complex effect on the porosity: total porosity (measured here) might presume upon agglomeration but instead the opened porosity can rapidly drop. The phenomenon that can affect the total porosity is cake formation: in the limiting case of very high melt superheat agglomeration mode can change from formation of separate porous agglomerates to material complete melting together into a cake.

Standalone comparison of the debris agglomeration in A11 and A12 tests (similar melt superheat) emphasize the importance of the droplet size effect (fragmentation) on the crystallization rate and consequently on debris agglomeration.

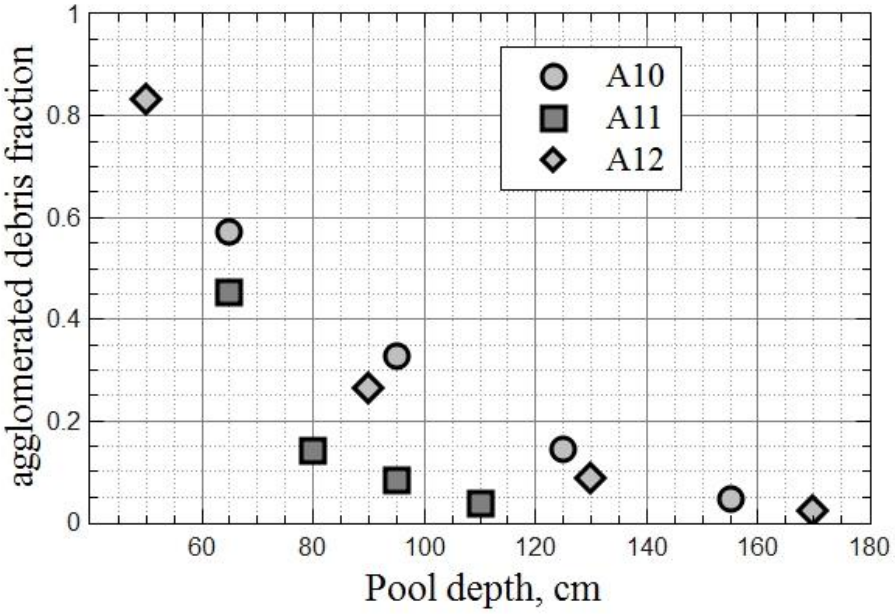

Figure 15: DEFOR-A10 and A11 agglomerated debris mass fraction

Comparison of the resulting particle size distribution is provided in the Figure 16. Higher melt jet entrance velocity into the water might affect melt fragmentation, causing formation of smaller particles. However, the effect of melt jet velocity doesn't appear evident from A10-11 tests comparison (clarify Figure 16a). The data from the comparison of A10 and A11 tests is insufficient to draw a solid conclusion about possible effect of jet velocity at the entrance to the water on (i) particle size distribution, (ii) fraction of agglomerated debris and (iii) porosity of the debris bed. In order to clarify such effects a more systematic study has to be carried out.

In contrast, comparison of the cumulative particle size distribution obtained in A12 vs A10 (Figure 16b) emphasize clear differences. The particle size distribution in A12 test has significantly lower fraction of small fragments and consequently higher amount of large ones. These results agree with our previous visual observations and with regard to debris morphology and agglomeration.

One can speculate that particle size distribution in cases where agglomeration and fracture are not important is governed in our experiment by two parameters: (i) melt temperature and (ii) jet velocity. Low superheat will promote fast crystallization and consequently large fragments, higher jet velocity will enhance hydrodynamic instabilities in the pool, provoke faster fragmentation and, consequently, smaller particles.

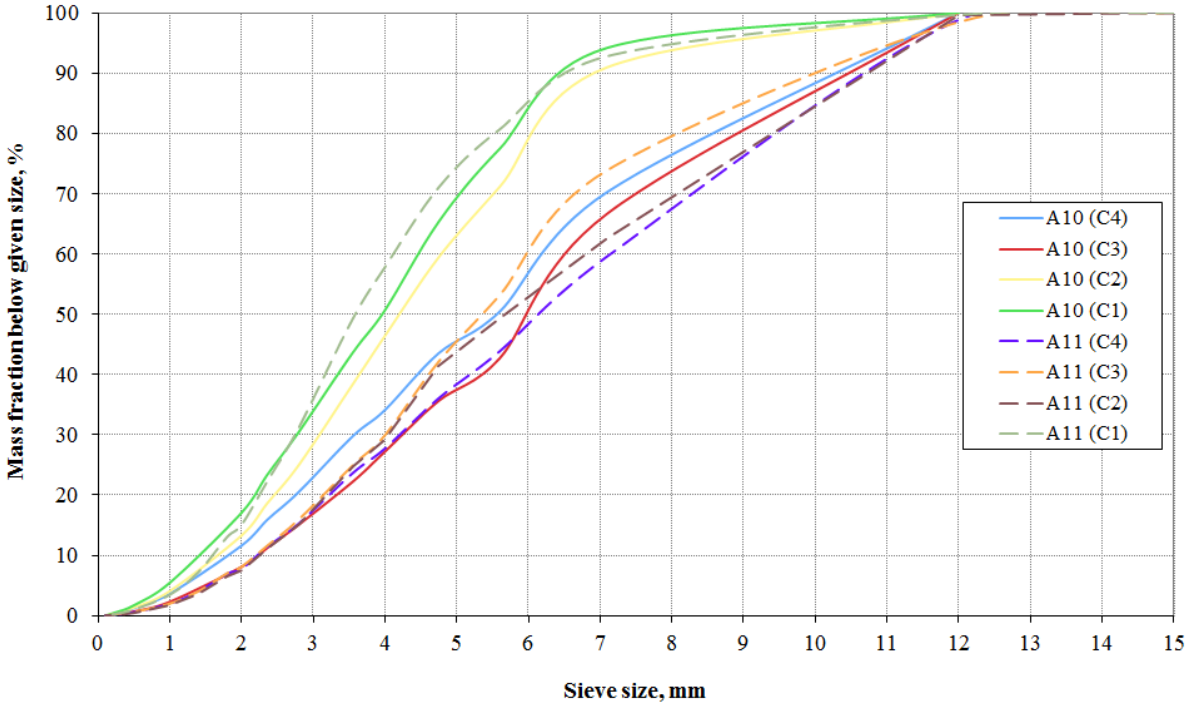

A10 vs A11

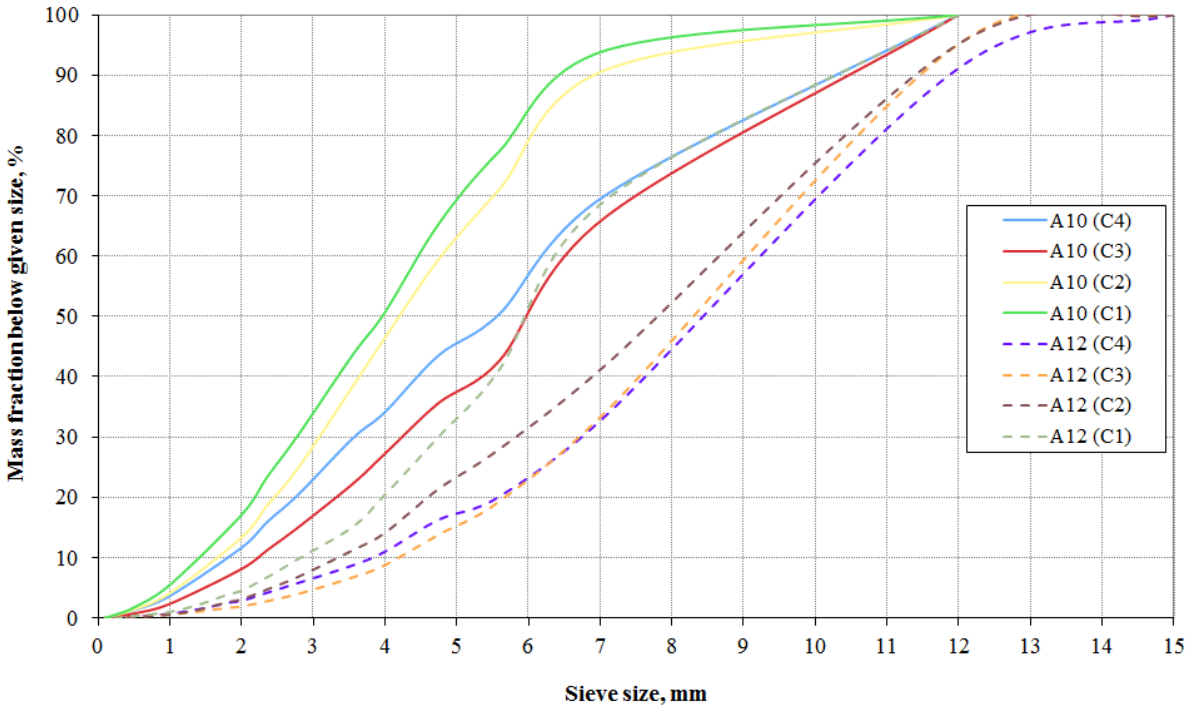

A10 vs A12

Figure 16: Cumulative mass fractions per catcher established in A10-13 tests

It is instructive to note that size distribution of fragmented particles (excluding agglomerates) measured in each catcher correlates with the fraction of agglomerated debris. In the Figure 16

one can notice a gap separating two groups of particle size distributions in both tests. Higher mass fraction of agglomerated debris in the first catchers corresponds to smaller particles.

Data in Figure 16 suggests that once the mass fraction of agglomerates is greater than certain value (above 20-30 %), the effect of the fraction of agglomerated debris on the particle size distribution becomes dominating.

In the following table we summarize the results of debris bed analysis; notice the total mass of the debris per catcher in terms that corresponding quantitative data can be less or more representative in comparison with others catchers.

Table 3: Comparison of the estimated and measured parameters in DEFOR-A10-13 tests

	DEFOR-A10				**DEFOR-A11**				**DEFOR-A12**				**DEFOR-A13**			
Melt superheat, ºC	150				102				114				62			
Catcher	C1	C2	C3	C4	C1	C2	C3	C4	C1	C2	C3	C4	C1	C2	C3	C4
Water depth*, cm	65	95	125	155	65	80	95	110	50	90	130	170	50	90	130	170
Debris mass, kg	2.90	3.29	4.02	2.06	5.82	1.99	3.10	3.73	2.06	5.82	1.99	3.10	0.34	0.26	0.32	0.07
Fragmented particles mass, kg	1.24	2.21	3.45	0.35	4.29	1.82	3.03	3.59	0.35	4.29	1.82	3.03	-	-	-	-
Agglomerated debris mass fraction, %	56.2	32.8	14.4	83.0	26.3	8.4	2.2	3.7	83.0	26.3	8.4	2.2	-	-	-	-
Heap lateral size along X, mm	230	390	230	120	200	180	280	300	120	200	180	280	-	-	-	-
Heap lateral size along Y, mm	190	190	320	190	390	280	310	340	190	390	280	310	-	-	-	-
Debris bed area, m^2	0.05	0.08	0.08	0.03	0.08	0.06	0.1	0.11	0.03	0.08	0.06	0.1	-	-	-	-
Max bed height, mm	39.1	37.1	40.9	61.6	64.0	36.6	44.0	66.5	61.6	64.0	36.6	44.0	-	-	-	-
Mass averaged bed height, mm	25.8	19.7	22.6	38.7	35.3	20.3	22.1	35.4	38.7	35.3	20.3	22.1	-	-	-	-
Estimated debris bed volume, liters	0.79	0.98	1.25	0.65	1.67	0.51	0.89	1.29	0.65	1.67	0.51	0.89	-	-	-	-
Error in the volume, %	±12	±17	±13	±8	±10	±22	±22	±17	±8	±10	±22	±22	-	-	-	-
Estimated total porosity, -	0.46	0.51	0.53	0.54	0.49	0.43	0.49	0.58	0.54	0.49	0.43	0.49	-	-	-	-
Error in total porosity, %	±3	±4	±3	±2	±3	±6	±5	±4	±2	±3	±6	±5	-	-	-	-

From the above observations we can also conclude that qualitative behavior of the new melt in terms of agglomeration and particle size distribution with respect to applied experimental procedure agrees well with available knowledge and general understanding of these phenomena typical for binary oxidic melt mixtures, which makes promising application of this material as a candidate for corium simulant material.

2.3.4 Posttest analysis of the samples

Results of post-test analysis of the test sample and debris solidified inside it are summarized in Table 4. This analysis is based on visual inspection of the sample and solidified melt in the sample. After every test the test sample is removed from the test section, dried, photographed and then cut into two pieces. The section is obtained along the vertical axis of the sample in a way preserving intact the ingot inside it. The cutting is done along the melt impingement point. The following objectives are perused:

- Assessment of the sample nozzle ablation;
- Assessment of the sample wall ablation;
- Analysis of the ingot, in terms of its mass and morphology.

Table 4: Test sample and debris properties in DEFOR-A12 and A13 tests

Parameter or property	Measured value or characteristic description	
	DEFOR-A12	DEFOR-A13
Nozzle diameter, mm	20	10
Wall thickness, mm	10	5
Solidified debris mass left inside sample, kg	2.35	5.446
Debris characteristics	Hollow shell ingot with large multiple cavities	Cake-like ingot, with a shrink cavity
Visible ablation of the sample nozzle	No	No
Ablation in the vicinity of jet impingement point	Up to 1.5 mm	Local melt through, severe erosion of the internal surface

In both experiments (A12 and A13) considerable amount of melt has been solidified inside the test sample. However in A13 the amount of the remaining melt was more than twice bigger than in A12. The posttest photographs of the test sample before cutting are shown in Figure 17. In A12 test melt pool has been established inside the sample, resulting in a smooth flat crust formation on the top upon solidification. A shrinking cavity crack can be seen at the top of it. Comparison of its mass to overall volume indicates that obtained ingot is a hollow shell. In contrast the morphology of debris bed in A13 test is completely different. One can see a rough surface looking like an agglomerated cake with a column of solidified melt under

the jet impingement location. The formation of the 10 cm stalagmite-like structure is due to low melt superheat and mushy, high viscosity melt flow at the end of the melt release.

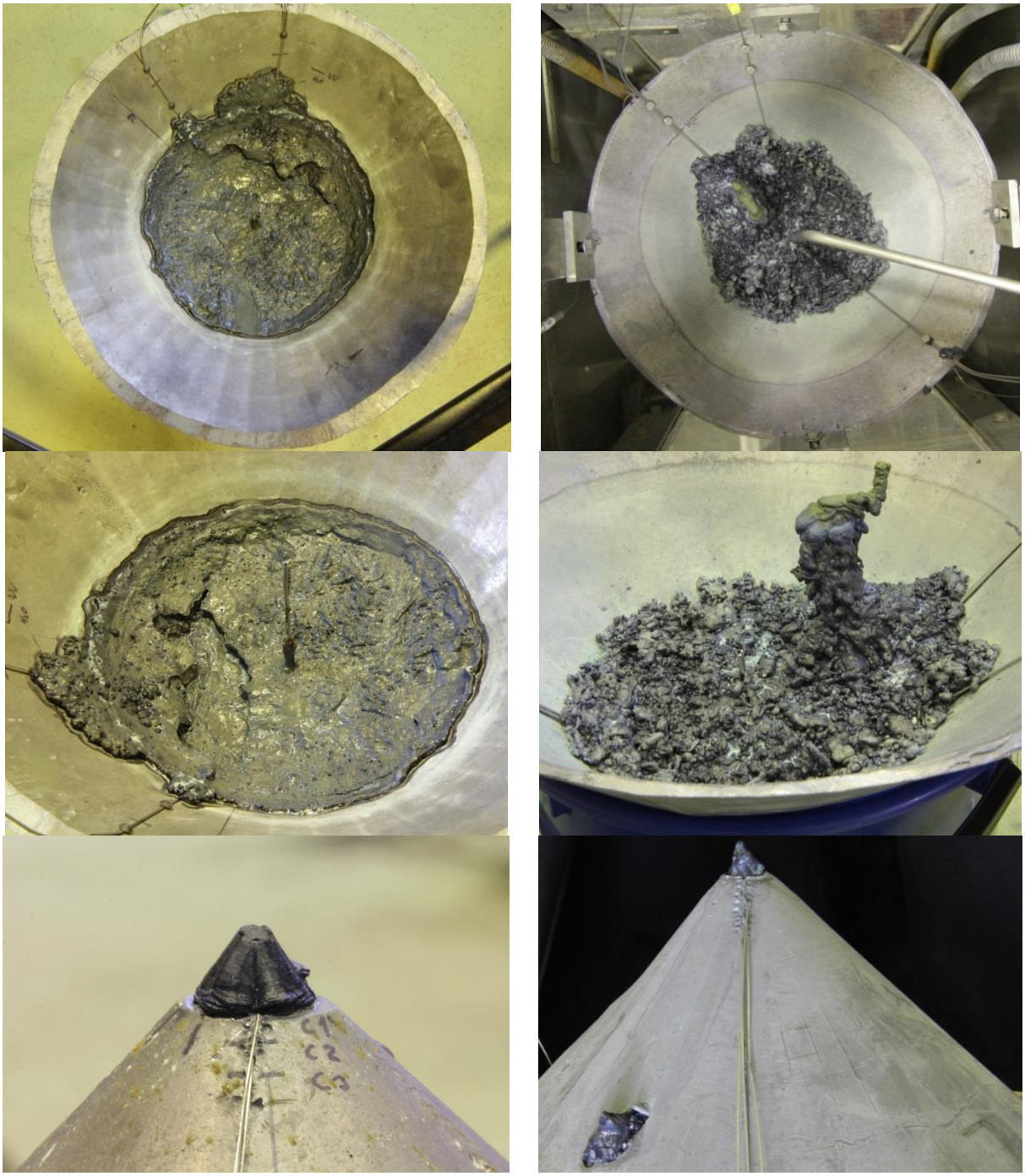

Figure 17: Debris bed solidified inside the sample in A12 (left) and A13 (right) tests

In both A12 and A13 tests the sample nozzle was plugged at the end of the melt release from the sample. In A13 test the wall of the sample was melted-through and the opening was also plugged by the melt. The location of the wall melt-through is shifted by few centimeters aside

from the jet impingent point (Figure 17, Figure 18, Figure 19). In Figure 19 severe erosion in the vicinity of the melt impingement point and melt through of the wall are clearly visible.

Figure 18: Test sample of A13 test after cutting: outlet and ablation hole

The results of the sample cutting are provided in Figure 20. Remarkably, no ablation of the sample nozzle was observed in A12 and A13 tests Figure 20. It is instructive to note the tightness of the plug in A12 test. Similar plugging occurred in A13 test, but the plug was shattered during cutting. Such crystallization without shrinkage cavity is possible if continuous supply of liquid melt can compensate for shrinkage. According to the video observation, formation of the plug is a relatively fast phenomenon. In A13 test it took less than 7 seconds to completely block the flow, while solidification of the bulk melt in the sample continued for the following several minutes. It is important to clarify how much sample nozzle plugging by solidified melt depends on the geometrical characteristics of the nozzle and on the melt flow rate. This should help to clarify if continuous melt release out of the sample can be interrupted while superheated melt is still being supplied into it.

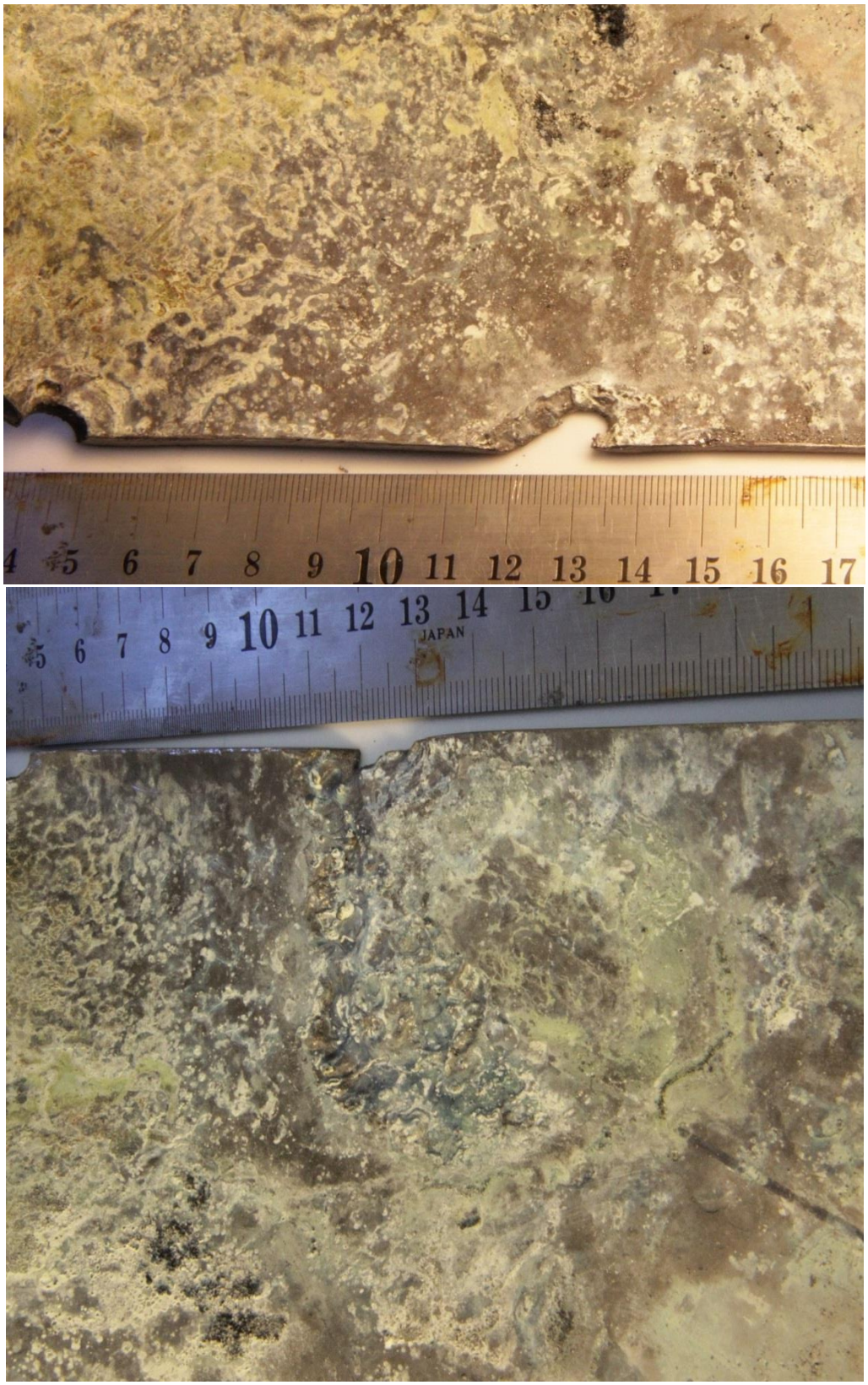

Figure 19: Test sample wall ablation in A13

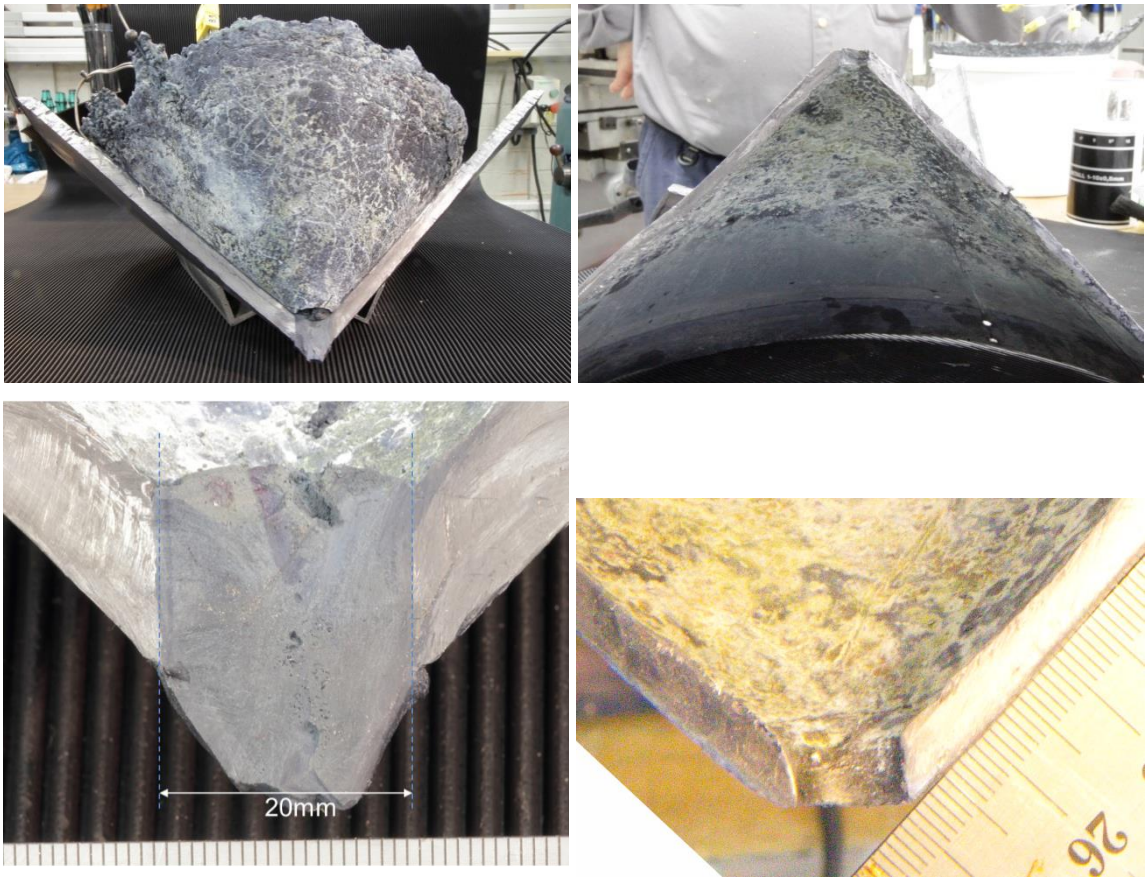

Figure 20: Test sample after cutting (left – A12, right – A13)

In general, ablation of the internal surface of the test sample in A13 test is much more pronounced than in A12 (Figure 21). These observations can be explained using below equations for the heat flux through the sample wall:

$$Q_{MG3} = k_{wall}\frac{\left(T_{wall\_sol} - T_{water\_sat}\right)}{\Delta_{wall}} = 35.3 \cdot \frac{227}{0.01} = 0.8\ MW/m^2$$

$$Q_{MG4} = 35.3 \cdot \frac{227}{0.005} = 1.6\ MW/m^2$$

The heat flux through the sample wall in A12 test is twice smaller than in A13 test. Dryout heat flux on such inclined surface can be estimated about 1 MW/m^2, thus the heat flux in A13 exceeded the dryout heat flux, leading to burnout of the wall with subsequent ablation of the opening.

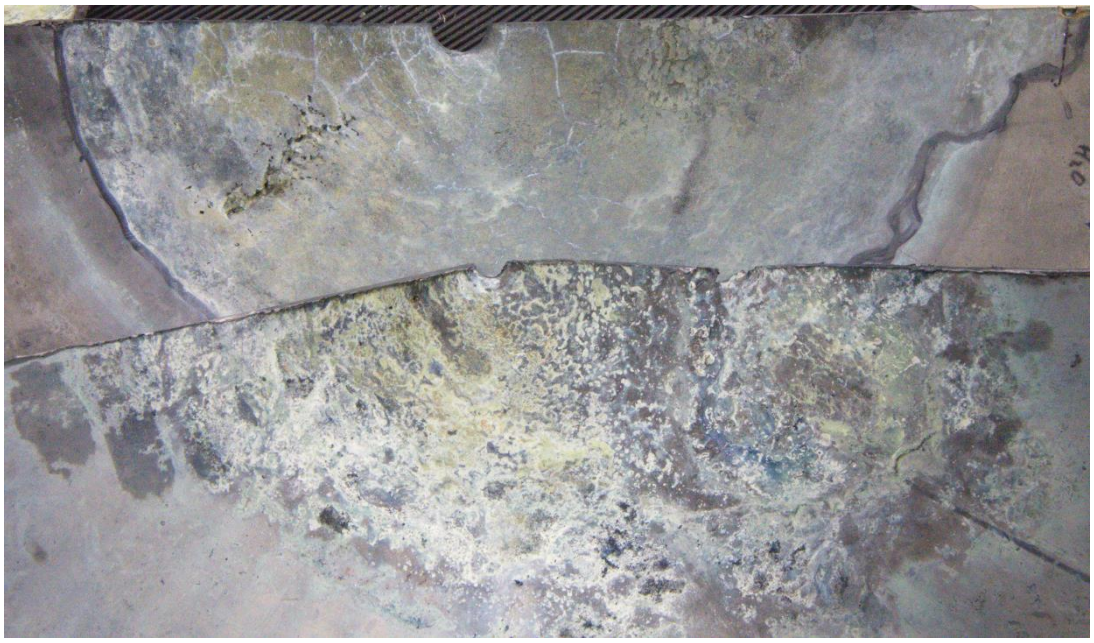

Figure 21: Test sample after cutting, comparison of surface erosion A12 at the top part of the image and A13 in the lower part

2.3.5 Comparison of the DEFOR-A10,A11 tests with FARO experiments and previous DEFOR test series

In Figure 22 we compare mass fraction of agglomerated debris as a function of the pool depth in the A10 and A11 tests to those obtained in the previous DEFOR-A and DEFOR-S experiments performed with another melt simulant material (Bi_2O_3-WO_3). In terms of the melt superheat and jet diameter the A10 and A11 tests can be compared to DEFOR-A7, A2, and A6.

For the sake of clarity in the Table 5 we provide relevant tests conditions. Note that exact value of water subcooling is of minor importance until thermal stresses start to induce solid particle fracture. For simplicity we can consider tests to be similar if subcooling is below 30 °C.

In the Figure 22 one can see that agglomeration curve of DEFOR-A10 test lies in between the curves of A7 and A2 tests being slightly closer to A2. This behavior agrees well with both melt superheat (A10 - 150 °C, A7 - 200 °C and A2 - 110 °C) and jet diameter (A10 – 20 mm, A7 – 25 mm and A2 – 20 mm).

Table 5: Relevant experimental parameters for DEFOR-A tests comparison to selected DEFOR-A tests

DEFOR test	Jet diameter, mm	Melt superheat, °C	Melt temperature, °C	Water subcooling, °C	Water pool depth, cm	Simulant
A10	20	150	1371	25	152	ZrO_2-WO_3
A11	15	102	1333	25	110	ZrO_2-WO_3
A7	25	206	1076	17	142	Bi_2O_3-WO_3
A2	20	103	973	7	152	Bi_2O_3-WO_3
A6	12	136	1006	27	152	Bi_2O_3-WO_3

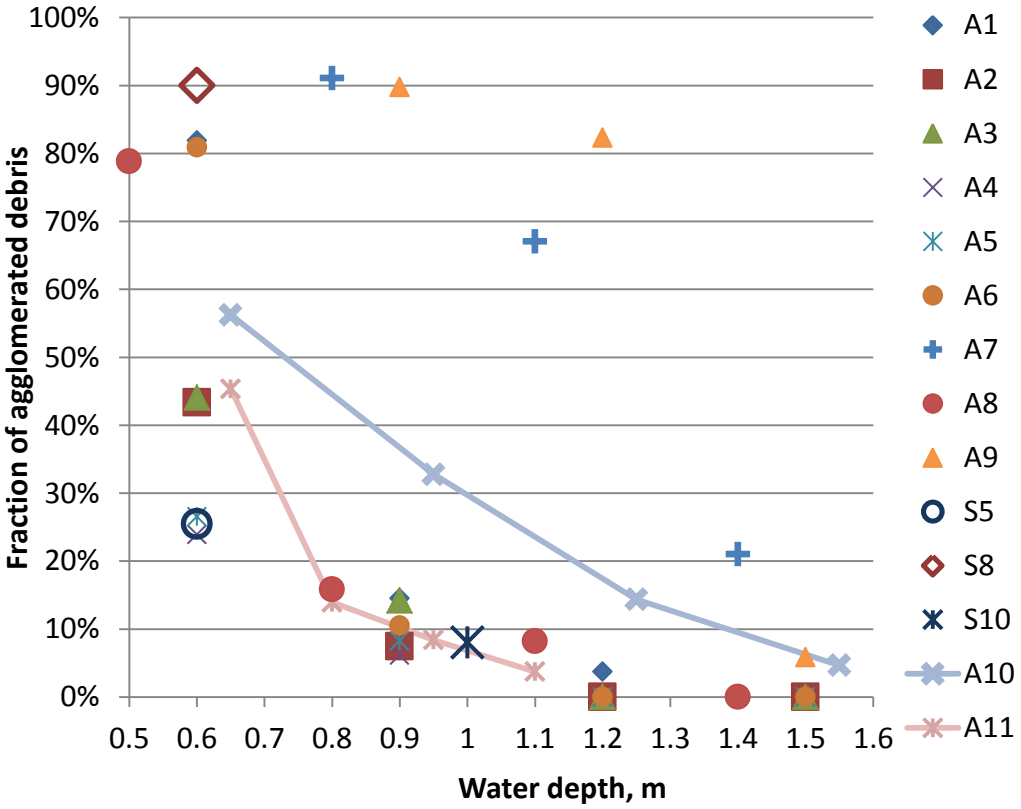

Figure 22: Comparison of the agglomerated debris fraction obtained in DEFOR-A10,A11 to previously performed DEFOR-A and DEFOR-S experiments

Direct comparison of A2,6,7 with A11 test is less straightforward due to higher velocity of the jet at the entrance into the water in A11 test. Therefore, we have chosen the jet diameter at the water level as the main similarity parameter. In terms of water subcooling and jet diameter at the water level, the closest to the A11 test is DEFOR-A6. It has slightly higher agglomeration on the top catcher which can be attributed to the higher melt superheat and experimental uncertainty due to proximity of the first catcher to the inherently instable position of the jet

leading edge in this test. With respect to other catchers DEFOR-A6 is in a good agreement with the A11 test.

From the above considerations we can conclude that behavior of the new simulant material in terms of agglomeration reasonably agrees with results from the previous DEFOR-A tests series.

In the following analysis we will compare the particle size distributions. The representative particle size distribution that describes accomplished melt fragmentation should be taken from the catcher with the smallest fraction of the agglomerates, in other words the one obtained from the debris bed collected at the bottom of the DEFOR test section. In the Figure 23 one can see that particle size distribution measured in new tests shows significantly higher fraction of larger particles compared to any of the previous DEFOR-A tests. Such important difference cannot be attributed to the differences in experimental conditions and can be explained only by application of different simulant melts.

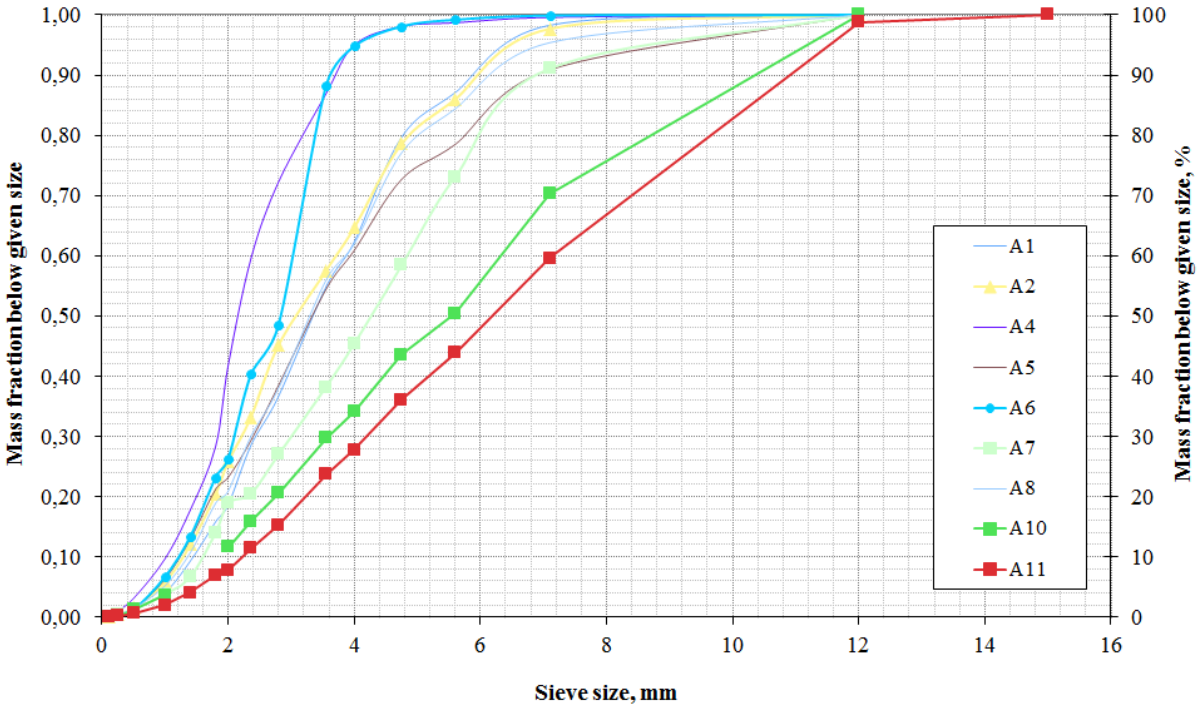

Figure 23: Comparison of the particle size distributions from DEFOR-A tests to DEFOR-A tests (only data from the bottom catcher is plotted)

In the Figure 24 we provide comparison of the ranges of particle size distributions from the A10-11 tests against FARO L28, L31 experiments performed with prototypical corium melts.

One can see a very good agreement between new DEFOR-A and FARO data. Some difference still remain but it can be attributed to such features of FARO tests as different initial jet diameter (50 – 100 mm) and agglomeration of the debris that alter the resulting particle size distribution (with the exception of FARO L31).

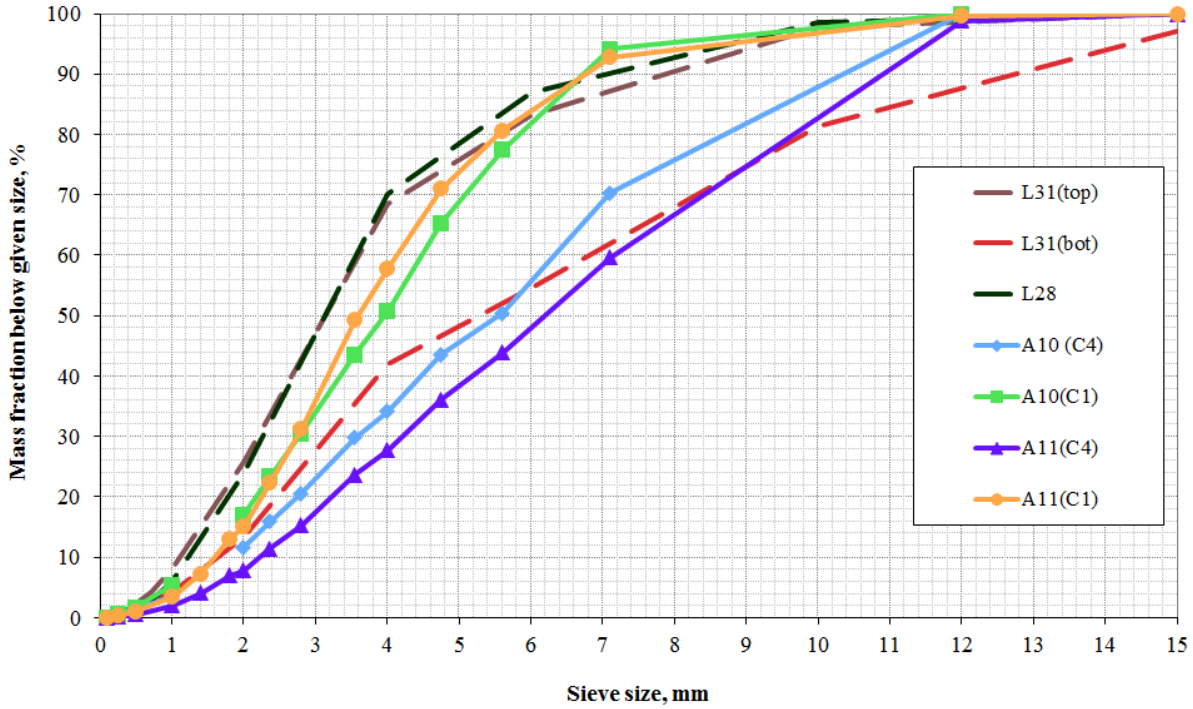

Figure 24: Comparison of the particle size distributions of DEFOR-A tests to FARO experiments

Note that debris bed in FARO L31 has been divided into 3 parts and sieved separately; the top and bottom parts distribution appeared to cover the full range of all FARO debris size distributions coming from non-explosive tests; in the figure the L31(top) and L31(bot) are used to span the range of FARO debris size distributions.

For the sake of clarity we provide the comparison of previous DEFOR-A to FARO tests in Figure 25. Previous DEFOR-A test series is also in a good overall agreement with FARO results. However, the DEFOR-A particle size distribution is closer to L28 data with smaller fraction of large particles, which could be reasonable given smaller jet diameters used in DEFOR-A tests.

Overall, from the comparison between DEFOR-A01-09, DEFOR-A10-13 and FARO data we can conclude that the influence of jet diameter and free fall height on the particle size distribution is less important than the influence of melt material. Indeed the difference

between FARO vs DEFOR-A10-13 and FARO vs DEFOR-A01-09 is smaller than the difference between DEFOR-A01-09 vs DEFOR-A10-13, although melt pouring conditions in DEFOR-A are much closer to each other (10-25 mm jet diameter and 20-70 cm jet free fall height) and quite different from FARO conditions (50-100 mm jet diameter and ~1-2 m jet free fall height).

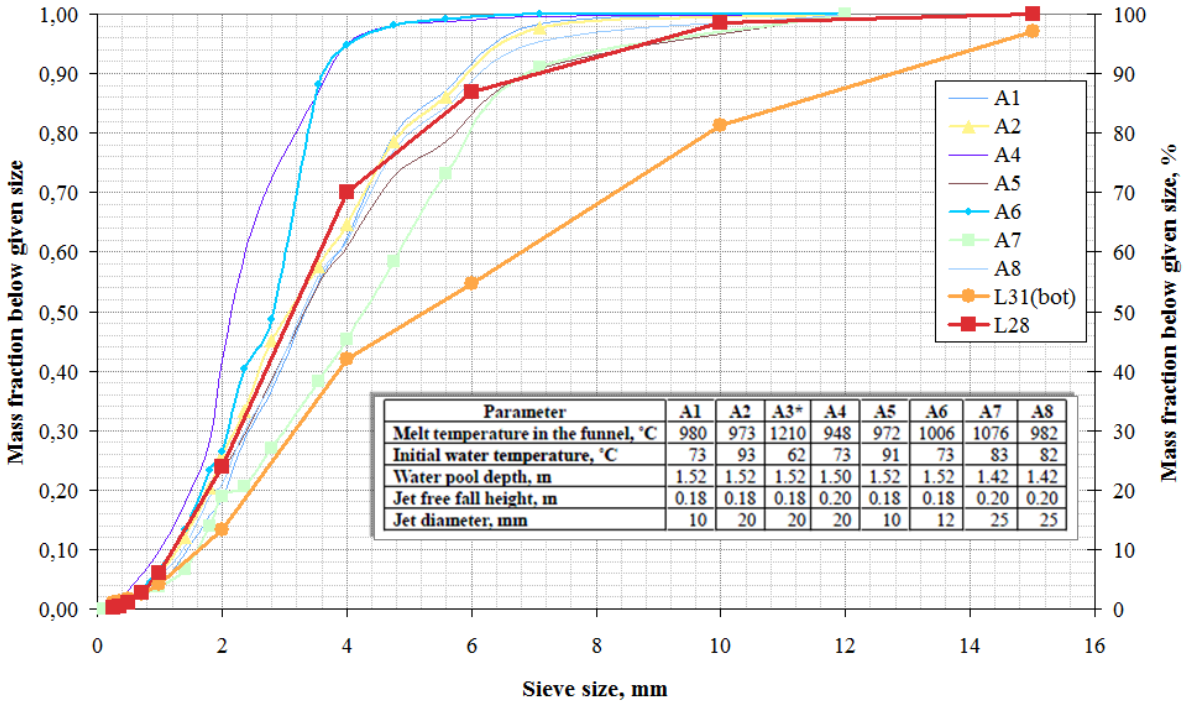

Parameter	A1	A2	A3*	A4	A5	A6	A7	A8
Melt temperature in the funnel, °C	980	973	1210	948	972	1006	1076	982
Initial water temperature, °C	73	93	62	73	91	73	83	82
Water pool depth, m	1.52	1.52	1.52	1.50	1.52	1.52	1.42	1.42
Jet free fall height, m	0.18	0.18	0.18	0.20	0.18	0.18	0.20	0.20
Jet diameter, mm	10	20	20	20	10	12	25	25

Figure 25: Comparison of the particle size distributions of DEFOR-A tests to FARO experiments

2.4 CONCLUSIONS

DEFOR-A10 and A11 tests have demonstrated that:

- Obtained with ZrO_2-WO_3 simulant material results in terms of agglomeration and fragmentation agrees well with previously established understanding of the respective phenomena.
- ZrO_2-WO_3 simulant does not produce opaque cloud upon release into water and indeed improves visualization of melt fragmentation.
- Obtained data on mass fraction of agglomerated debris as a function of water pool depth is in a good agreement with the data from the previous DEFOR-A tests series.
- In general there is a good reproducibility of the results in terms of agglomeration even with respect to different experimental parameters including melt material.

- Obtained data on particle size distribution shows overall larger ZrO_2-WO_3 particles than in the previous DEFOR-A tests with Bi_2O_3-WO_3.
- The particle size distribution from DEFOR-A10 and A11 tests is in a better agreement with FARO experiments performed with prototypic corium mixtures making it a better simulant material from this point of view.
- Particle size distribution seems to be more affected by melt material than by jet characteristics (diameter and water entrance velocity), as it stems from cross comparison of DEFOR-A01-09, DEFOR-A10-13 and FARO.

Results of the DEFOR A10 and A11 tests (i) have confirmed that application of the new simulant material for investigation of melt fragmentation and agglomeration is plausible, and (ii) have provided reliable reference data necessary for comparison with results from DEFOR-A12 and DEFOR-A13 tests.

Our primary conclusions with respect to the obtained experimental data in exploratory A12 and A13 tests are as follows:

1. Comparison of the A10 and A12 test in terms of debris bed total porosity and particle size distribution demonstrate that for the test sample with 20 mm outlet diameter the obtained debris bed has similar total porosity but considerably higher average size of the particles. Large size particles are better for coolability, but can hinder particulate debris spreading and increase chances for debris agglomeration due to longer time for solidification of larger particles. In general, the fraction of agglomerated debris in A12 test with test sample and with melt superheat about 100 °C is almost the same as in A11 tests without the sample and with melt superheat of about 150 °C.
2. Plugging of the test sample nozzle was observed in both A12 and A13 tests. Considerable mass of melt was entrapped inside the test sample due to this phenomenon. It should be stressed that plugging has occurred in cases of rather small nozzle outlets and further experiments are required to verify relevance of this phenomena for larger nozzles.
3. Ablation of the sample wall is dependent on the wall thickness. Very little erosion of the inner surface of the sample wall was observed in A12 with 10 mm wall and melt-through and ablation of the 5 mm wall were observed in A13 test in the vicinity of melt jet impingement point.

4. No noticeable radial nozzle ablation was observed in both A12 and A13 tests. This is currently attributed to the effect of the external convective cooling of the nozzle. Further study of the wall ablation in conditions of external convective cooling is required to identify onset conditions for nozzle radial ablation.
5. It should be kept in mind that in the last A13 test wall melt through did not occur precisely at the jet impingement point.

3 DECOSIM code development and validation against the experimental results produced in COOLOCE and POMECO-HT facilities.

3.1 Overview of DECOSIM code

DECOSIM is a thermohydraulic code being developed at KTH for simulation of debris bed formation and coolability [47], [48]. In the framework of DECOSE project, validation of DECOSIM code is being performed against the existing COOLOCE data.

DECOSIM has been developed to take into account not only the flows in the porous medium, but also natural convection flows in the pool, where turbulence models and discrete particle models apply [49], [50]. In this work, only a subset of all models was used: the space beyond the debris bed was filled with an artificial porous medium with low drag, so that the flow in the whole computational domain was calculated from the filtration equations. Also, saturated conditions are assumed in the debris bed and above it, so that the governing equations to be solved are the continuity equations for each phase.

Under the assumption of saturated conditions, the criterion employed to detect the local dryout is based on the analysis of the void fraction distribution, rather than the temperature field. A special algorithm for finding the dryout boundary has been developed and implemented in DECOSIM. For each given shape and properties of the debris bed (input parameters), a set of calculations was carried out in which the specific heat power released in the porous material was varied. First, two values of the specific heat power were set by the user, the higher of which results in the dryout, and the lower of which corresponds to steady-state cooling (no dryout). Then, the next value of the specific heat power was taken as the arithmetic mean of the two powers, and simulation was run with this new power to find out if dryout occurs or now. Depending on the outcome of the simulation, either the lower, or the upper boundary of the heat power interval was set to the last heat power, and the procedure was repeated. This algorithm is similar to the well-known bisection algorithm for finding the root of a function, the iterations are repeated until the upper and lower boundaries of the interval become close enough (i.e., their difference become smaller than some prescribed tolerance).

To speed up calculations, the intermediate solutions were not run to convergence; rather, empirical rules based on the observations of the behavior of the maximum void fraction in the debris bed were formulated and implemented in the code to decide if dryout is going to occur or not. This enabled the dryout boundary to be found much more efficiently than in the original version of the algorithm where all intermediate solutions were run to convergence.

It should be noted that the capability to solve the energy equations for the liquid and gas phases has been recently implemented in DECOSIM, together with the solver for heat transfer in the solid phase. These new capabilities will be utilized in the further validation studies, including the simulations of debris bed coolability in an initially subcooled water pool.

3.2 Governing Equations and Numerical Solver

Consider a debris bed submerged in a water pool. Transient distributions are sought for the volume fractions α_i, superficial velocities $\mathbf{j}_i$ of liquid and gas phases (subscripts L and G, respectively), and pressure P.

The phase continuity and momentum equations are

$$\frac{\partial \rho_G \alpha_G}{\partial t} + \nabla\left(\rho_G \mathbf{j}_G\right) = \Gamma, \qquad \frac{\partial \rho_L \alpha_L}{\partial t} + \nabla\left(\rho_L \mathbf{j}_L\right) = -\Gamma \tag{3.1}$$

$$-\nabla P + \rho_G \mathbf{g} = \frac{\mu_G}{K K_{rG}} \mathbf{j}_G + \frac{\rho_G}{\eta \eta_{rG}} |\mathbf{j}_G| \mathbf{j}_G \tag{3.2}$$

$$-\nabla P + \rho_L \mathbf{g} = \frac{\mu_L}{K K_{rL}} \mathbf{j}_L + \frac{\rho_L}{\eta \eta_{rL}} |\mathbf{j}_L| \mathbf{j}_L \tag{3.3}$$

Here, $\mathbf{g}$ is the gravity acceleration, ρ_i and μ_i are the densities and viscosities of the liquid and gas phases ($i = L, G$). The right-hand sides of Eqs. (3.2) and (3.3) contain the phase drag due to porous medium with linear and quadratic terms (with the absolute, K, η, and relative, K_{ri}, η_{ri}, permeabilities and passabilities). Commonly, saturated conditions are assumed in the debris bed, with the volumetric evaporation rate being $\Gamma = Q/\Delta H_{ev}$, where Q is the heat release rate per unit volume of debris bed, ΔH_{ev} is the latent heat of evaporation (i.e., decay heat goes to water evaporation). Under this assumption, the fluid properties ρ_i and μ_i are functions of the pressure P. The properties of water in liquid and vapor states (densities ρ_i,

enthalpies h_i, viscosities μ_i, thermal conductivities λ_i) as functions of pressure and temperature are implemented as polynomials according to IAPWS-IF97 formulation ("Steam tables") [57].

The drag force due to solid debris (see the first and second terms on the right-hand sides of Eqs. (3.3) is characterized by the permeability K and passability η depending on the properties of the porous medium. For monodisperse spherical particles, these are related to the porosity ε and particle diameter d [57]:

$$K = \frac{\varepsilon^3 d^2}{150(1-\varepsilon)^2}, \qquad \eta = \frac{\varepsilon^3 d}{1.75(1-\varepsilon)} \tag{3.4}$$

These relations can also be used for particles of arbitrary shapes, provided that d is substituted by a properly averaged effective mean particle diameter. The relative permeabilities K_{ri} and passabilities η_{ri} are functions of the void fraction α, they are commonly described by power-law relations:

$$\begin{aligned} K_{rL} &= (1-\alpha)^{nL}, \quad \eta_{rL} = (1-\alpha)^{mL} \\ K_{rG} &= \alpha^{nG}, \qquad \eta_{rG} = \alpha^{mG} \end{aligned} \tag{3.5}$$

In Reed's model [58], the interphase drag is neglected, the exponents in the relative permeabilities are $nL = nG = 3$, and those in the relative passabilities are $mL = mG = 5$.

In DECOSIM, all transport equations are discretized on a staggered orthogonal grid in the 2D axisymmetric geometry. On each time step, the momentum equations are solved first to find out the preliminary velocity components of each phase. The velocity corrections are expressed in terms of pressure and volume fraction corrections, with the phase change terms taken into account implicitly. They are then substituted into the phase continuity and energy equation which are solved in a fully coupled manner by an efficient ILUT-preconditioned PGMRES solver from SPARSKIT package. Global iterations are performed on each time step until convergence with prescribed accuracy is reached. The time step is varied adaptively, depending on convergence success or failure.

DECOSIM has been validated with respect to various separate effects, including two-phase drag in porous media and coolability of flat and axisymmetric (cone-shaped) ex-vessel debris

beds in configurations. The models and closures involved are similar to those of WABE/MEWA code [59] with which some cross-code verifications have been carried out. At the moment, no reactor-scale experiments are available to enable integral validation of this (or similar) codes.

3.3 Search Algorithm for Determination of Coolability Boundary

To study the debris bed coolability, an algorithm for automatic search for the dryout boundary is required. A straightforward algorithm is the following: the heat release rate (HRR) is gradually increased with some step, and for each HRR transient simulation is run for a long enough time period. The minimum HRR causing the dryout is considered to be the boundary. The dryout criterion is based on the monitoring the void fraction in the debris bed. Dryout was detected if the void fraction in any cell of the grid reached the critical value (0.95–0.975), after that the heat release rate was ramped to zero because evaporation becomes inefficient for such high void fractions.

This approach has several drawbacks. Firstly, it requires long and useless calculations far from dryout, when the flow reaches the steady state. Secondly, it can miss the dryout HRR, since the time between the HRR increase and actual dryout can be very long, especially for a flat layer (see [60]). Thirdly, the accuracy of the dryout boundary detection is of the order of HRR step, and to increase the accuracy it is required to use smaller steps in HRR and, therefore, more simulations are required.

To improve the efficiency, an algorithm was proposed which makes possible an automatic search of the dryout boundary. Its main idea is to vary the HRR using the bisection algorithm and use certain semi-empirical criteria to determine whether the current state of the debris bed is likely to lead to steady state cooling, or to dryout. In what follows, the algorithm is described in detail.

The debris bed is initially filled with water in the saturated conditions. The heat released in the porous material causes the production of water vapor, which results in the development of water and vapor flows. The void fraction in the bed increases gradually, and, finally, two scenarios are possible: either the debris bed is coolable (steady-state conditions are attained), or dryout can occur at some point. Theoretically, the final state can only be checked in an

infinitely long calculation (because the time to dryout can be quite long and is not known beforehand). To make the algorithm efficient, criteria were proposed for the following:

1. Convergence of all fields (velocities, pressure, volume fractions) in the debris bed to steady-state distributions with some tolerance.
2. The maximum void fraction in the debris bed.

These criteria were chosen as they are close to the physical meaning of steady-state cooling and dryout. Other criteria checked during the coolability simulations are the convergence of all fields on the whole grid, which happened to give almost the same results as that inside the bed, and the average void fraction.

After some trial runs, the following parameters were chosen for the search:

1. To check if the fields converged to some steady state, they were averaged over the last ten steps in order to reduce the effect of possible fluctuations of the numerical nature. The averaged values were compared every 10 seconds. Then, for each of the seven monitored variables the maximum change was found and normalized. For normalization, the pressure and volume fractions were divided by the maximum value of the corresponding field in the bed; the velocity components were divided by the absolute values of the superficial velocity vector. The highest value of the normalized increments was compared to the steady state criterion (SSC); if it happened to be lower than SSC, the debris bed was assumed to be in its steady state.

   The SSC was chosen after several runs on the test problems. It strongly depends on the time between criterion checks, since the larger is the time interval the smaller should be the criterion. It should be noted that high SSC (10^{-3} or higher) leads to significant misses of the dryout, especially for flat debris bed. Very low SSC (10^{-6} and lower) leads to high computation time, and sometimes the problem doesn't converge to meet such an accuracy criterion at all. After all trials, the following formula was chosen for the SSC:

$$\mathrm{SSC} = \min\left(10^{-4}, 10^{-5} \cdot \frac{\text{HRR Dry} - \text{HRR Wet}}{\text{target HRR accuracy}}\right)$$

   where HRR Dry and HRR Wet are the currently available boundaries of the Dryout HRR (DHRR).
2. The maximum void fraction (AMax) is a very useful criterion for the assessment of the states close to DHRR. It was shown that, for example, for a flat debris bed without bottom water injection the maximum void fraction for steady-state cooling is approximately equal

to 0.8. Any higher values lead to gradual increase in the void fraction and, finally, to dryout. For non-flat configurations, or in the presence of water inflow from below, the maximum void fraction in the coolable state can reach 1.0, but it very quickly increases with the increase in HRR. Thus, the value of 0.95 was chosen as the critical value, indicating dryout in the bed.

Another important issue is to determine if the state became coolable after the HRR has been decreased. Simulations show that decrease of the AMax below 0.92 from the dryout state always indicate rewetting and show that current HRR corresponds to coolable state. But this criterion is not very efficient since the process of rewetting may take very long time, and it is hard to determine if the state is coolable or not since the fields are not converged to the steady state. To prevent this, after 500 s the current HRR is decreased, however, no conclusion is made about the state of the bed.

The full algorithm based on these two criteria is shown in Figure 26. The input data for the algorithm are the initial heat release rate, and the wet-state HRR (optional). In the initial state, DECOSIM runs until the steady state is reached, or dryout occurs. If the steady state is reached, the current value of HRR is considered as “wet” and the HRR is increased by a factor of 1.3. This multiplier was chosen since large HRR increase can lead to states far from the wet state, which converge very slowly, while small multipliers lead to slow convergence if the initial HRR is far below the dryout boundary.

After the first dryout has occurred, the main part of bisection algorithm is executed, in which there are two known states corresponding to coolable and non-coolable bed, and their arithmetic mean is used as the next current HRR to be checked. After each change of wet and dry limits, their difference is compared with the user-defined target HRR accuracy. Once the difference becomes smaller than the prescribed HRR accuracy, the average of the wet and dry-state HRR is taken as the coolability boundary.

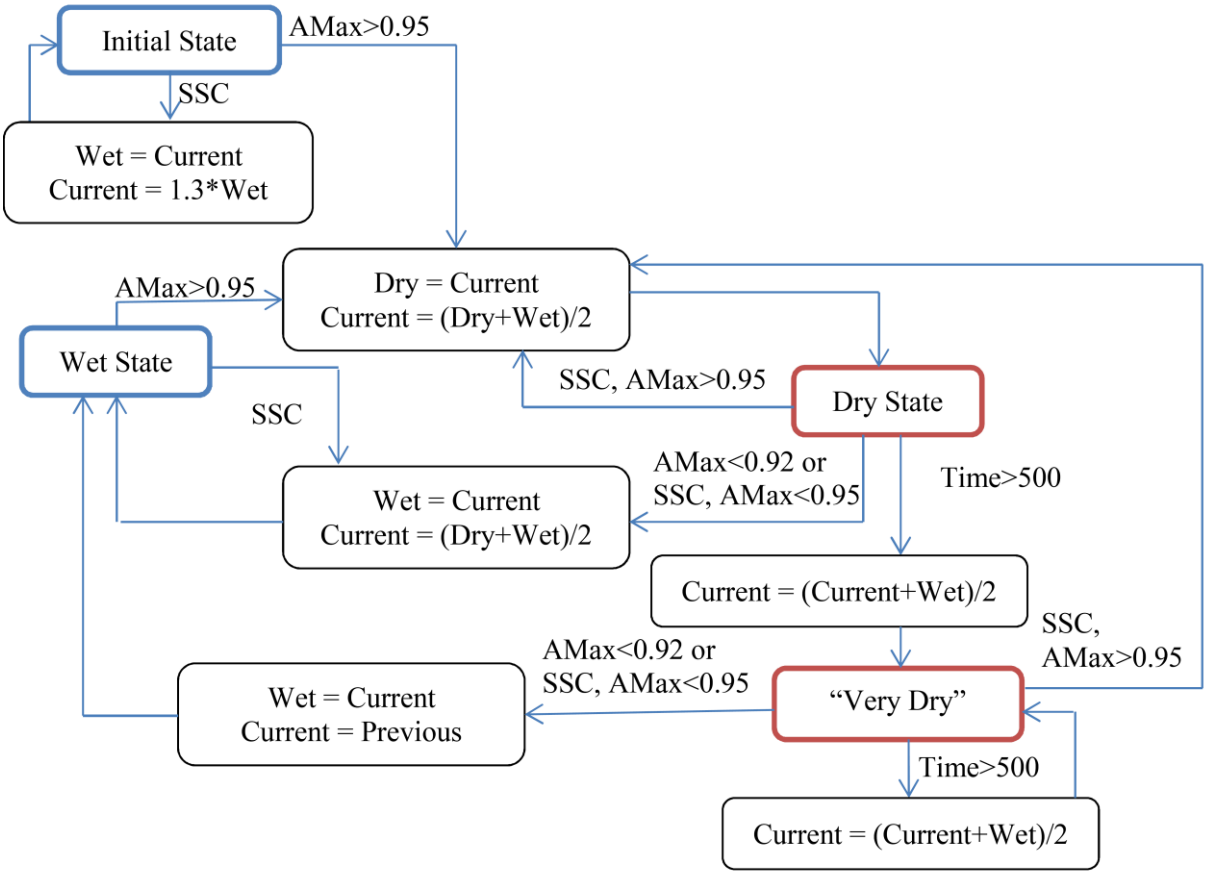

Figure 26: Bisection search algorithm for the dryout boundary.

Before the algorithm was applied to real problems, its sensitivity to computational parameters was studies in test calculations. There are three main parameters of the algorithm which may affect the final result: the steady state criterion, dryout and ramping void fractions, and initial values of heat release rate.

All data given below are obtained for the conical COOLOCE configuration with system pressure of 1.1 bar using Reed's model [58]. The grid had 31×57 cells, and the cell size was 1.0×1.0 cm. It should be noted that the method was also tested on many other configurations, including real pool simulations with different particle diameters, porosities, system pressure, and shape of the bed.

Before the algorithm was applied to validation simulations, its sensitivity to computational parameters was studies in the test calculations. There are three main parameters of the

algorithm which may affect the final result: the steady state criterion, dryout and ramping void fractions, and initial values of heat release rate.

All data given below are obtained for the conical COOLOCE configuration with system pressure of 1.1 bar using Reed's model. The grid had 31×57 cells, and the cell size was 1.0 cm×1.0 cm. It should be noted that the method was also tested on many other configurations, including real pool simulations with different particle diameters, porosities, system pressure, and shape of the bed.

Dependence on Steady State Criterion (SSC)

The dependence on SSC is non-monotonic and is significantly affected by all input parameters and starting HRR values. There were found many parameters and starting points for calculations which misinterpreted the state as steady using the criterion $10^{-2} - 10^{-3}$. It was shown that, in order to obtain the boundary with precision ~1%, it is enough to take steady state criterion equal to 10^{-4}.

Dependence on dryout and ramping void fractions

The results of changing the void fractions are shown in the figure. As was noted above, the maximum void fraction in the bed at steady state increases quickly with increase of the HRR. One can see from the table that the difference in results is higher than target HRR accuracy, however, it is still quite small.

Dryout void fraction	Ramping void fraction	DHRR, W/kg
0.93	0.965	199.5
0.95	0.975	200.8
0.97	0.985	201.8

Dependence on initial HRR

The algorithm is almost insensitive to the initial heat release rates. The results are shown in the table; one can see that their difference is less than target HRR accuracy.

Initial HRR, W/kg	Initial wet HRR, W/kg	DHRR, W/kg
250	130	200.8
223	115	200.6
220	190	200.8
240	170	200.9

Grid convergence

The grid convergence was also checked on the conical COOLOCE configuration with system pressure of 1.1 bar using Reed model. The grid was uniform in first 5 cases (see the Table below), the values of DHRR are shown in Figure 27.

Cell size, cm	Grid size	Grid Type	DHRR, W/kg
2.0	16×29	uniform	216.1
1.0	31×57	uniform	200.8
0.70	45×85	uniform	189.8
0.40	77×143	uniform	184.7
0.20	154×286	uniform	183.4
2.0-0.70	31×40	non-uniform, 1/3 dense	192.9

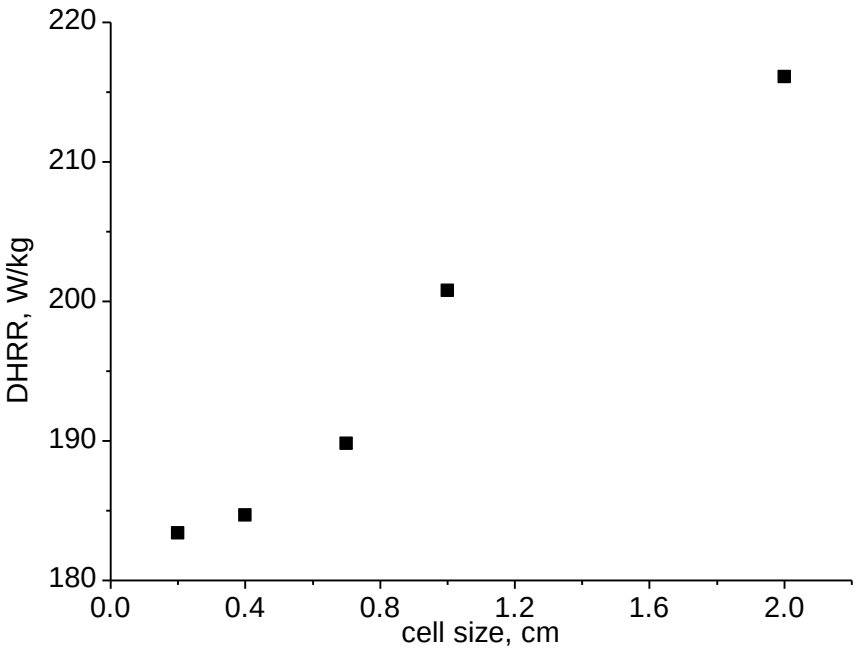

Figure 27: Grid convergence results: dependence of dryout heat release rate on cell size.

One can see that the difference in DHRR values obtained on grids with cell sizes 0.70 cm and 0.20 cm (the finest grid) is within 4%. However, simulations on the finest grid and require too much computational time because of large number of cells. To reduce the computational cost, a non-uniform grid was used with the refined area near the tip of the cone, since this region determines the coolability of the debris bed. The dryout heat release rate obtained on this grid

is almost the same as on third grid, at the same time, the number of cells is three times smaller.

3.4 Parameters of DECOSIM Simulations

In the current validation studies, the data from the COOLOCE experiments performed at VTT in 2010-2011 (see [1], [2], [63], [64], [65], [66]) were used. Simulations were carried with Reed's model [58] for the phase drag in the porous medium. Parameters of the calculations are listed in Table 6.

Table 6: Parameters used in DECOSIM simulations of COOLOCE experiments.

Fixed Parameters		
Water pool geometry	Radius: Height:	0.306 m 0.57 m
Cylindrical Geometry (COOLOCE-3,4,5) (impermeable side wall)	Height: Diameter: Surface area: Volume:	0.27 m 0.31 m 0.07548 m^2 0.02038 m^3
Conical Geometry (COOLOCE-6,7)	Height: Diameter: Volume:	0.27 m 0.50 m 0.01767 m^3
Friction model	Reed	
Variable Parameters		
System pressure	P_{sys}:	1.1-6.95 bar
Particle diameters	d	0.8–1.07 mm
Porosity	ε	37–40%

The system pressure was varied in accordance with the conditions of each COOLOCE experiment. The debris bed porosity and mean particle diameter, however, were varied in order to take into account the existing uncertainties in the properties of the debris bed. The debris bed particles used in the COOLOCE tests were spherical beads of Zirconium silicate whose sizes vary between 0.8 mm to 1 mm. The porosity of the debris bed reported by VTT was 37%. However, measurements performed in POMECO-FL facility for the same particles

gave a higher value of porosity close to 40%, while the mean particle diameter determined from the particle size distribution analysis was higher than 0.8 mm, see Figure 38.

In the current simulations, the baseline debris bed properties were taken to be the lowest values of particle diameter $d = 0.8$ mm and porosity $\varepsilon = 37\%$. It was obtained that this case gives underestimates the dryout boundary in comparison with the COOLOCE experiments. Therefore, simulations were repeated with the porosity determined from POMECO-FL tests (40%) and the particle diameter 0.89 mm, as well as for the porosity reported by VTT (37%) and particle diameter 1.07 mm. In the latter cases, the effective particle diameter was found from the best agreement of DHF predictions from one-dimensional debris bed model with COOLOCE experiments performed for cylindrical debris bed.

3.5 Summary of Results

The simulation cases and the results obtained are summarized in Table 7 (for cylindrical debris bed) and Table 8 (for conical debris bed). For the conical debris bed, simulations have only been performed so far for two combinations of particle diameter and porosity, and only one point was obtained for the third combination.

The respective dependencies of the calculated dryout heat power on the system pressure are plotted in Figure 28 (for cylindrical debris bed, presented as the dryout heat flux DHF, W/m^2) and Figure 29 (for conical debris bed). On the same graphs, results of numerical simulations by MEWA code reported in [67] are plotted for comparison, with the respective particle diameters and porosities indicated in the legends. Note that in [67] MEWA simulations of the cylindrical debris bed were carried out with Reed's model for the drag in porous medium [58], the same as used in the current DECOSIM simulations. However, for the conical debris beds, the model by Tung and Dhir [68] with the modifications for small particles proposed in [69] was used; this model takes into account the interphase drag which is neglected in Reed's drag model [58].

Experimental data from COOLOCE tests are presented in Figure 28 and Figure 29 by the black points. Also, in Figure 28, an experimental point is plotted (green dot) corresponding to the measurement of dryout heat flux in POMECO-HT experiment [62] performed for the same spherical beads as in COOLOCE experiments.

Table 7: DECOSIM simulations of COOLOCE experiments with cylindrical debris bed.

Case No.	**Experiment**	**Pressure P_{sys}, bar**	**Experimental dryout power, kW**	**Calculated dryout power, kW**	**Comments**
1	COOLOCE-3	1.1	19.0	11.5	$d = 0.8$ mm, $\varepsilon = 37\%$
	COOLOCE-3R		20.4	19.0	$d = 0.89$ mm, $\varepsilon = 40\%$
				19.2	$d = 1.07$ mm, $\varepsilon = 37\%$
2	COOLOCE-4	1.6	23.4	14.7	$d = 0.8$ mm, $\varepsilon = 37\%$
				22.8	$d = 0.89$ mm, $\varepsilon = 40\%$
				23.0	$d = 1.07$ mm, $\varepsilon = 37\%$
3	COOLOCE-4	1.9	26.1	16.0	$d = 0.8$ mm, $\varepsilon = 37\%$
	COOLOCE-4bR	1.95	26.2	24.8	$d = 0.89$ mm, $\varepsilon = 40\%$
				24.9	$d = 1.07$ mm, $\varepsilon = 37\%$
4	COOLOCE-5	3.0	31.9	20.1	$d = 0.8$ mm, $\varepsilon = 37\%$
				30.6	$d = 0.89$ mm, $\varepsilon = 40\%$
				30.6	$d = 1.07$ mm, $\varepsilon = 37\%$
5	COOLOCE-5	4.0	34.6	23.1	$d = 0.8$ mm, $\varepsilon = 37\%$
				34.8	$d = 0.89$ mm, $\varepsilon = 40\%$
				34.7	$d = 1.07$ mm, $\varepsilon = 37\%$
6	COOLOCE-5	4.95	37.2	25.5	$d = 0.8$ mm, $\varepsilon = 37\%$
				38.1	$d = 0.89$ mm, $\varepsilon = 40\%$
				37.9	$d = 1.07$ mm, $\varepsilon = 37\%$
7	COOLOCE-5	6.95	42.3	29.6	$d = 0.8$ mm, $\varepsilon = 37\%$
				43.8	$d = 0.89$ mm, $\varepsilon = 40\%$
				43.4	$d = 1.07$ mm, $\varepsilon = 37\%$

Table 8: DECOSIM simulations of COOLOCE experiments with conical debris bed.

Case No.	**Experiment**	**Pressure P_{sys}, bar**	**Experimental dryout power, kW**	**Calculated dryout power, kW**	**Comments**
8	COOLOCE-6	1.1	26.0	18.0 27.8 28.1	$d = 0.8$ mm, $\varepsilon = 37\%$ $d = 0.89$ mm, $\varepsilon = 40\%$ $d = 1.07$ mm, $\varepsilon = 37\%$
9	COOLOCE-7	1.6	31.8	22.6 34.0 –	$d = 0.8$ mm, $\varepsilon = 37\%$ $d = 0.89$ mm, $\varepsilon = 40\%$ $d = 1.07$ mm, $\varepsilon = 37\%$
10	COOLOCE-7	2.0	36.0	25.5 38.2 –	$d = 0.8$ mm, $\varepsilon = 37\%$ 1.914.9mm, $\varepsilon = 40\%$ $d = 1.07$ mm, $\varepsilon = 37\%$
11	COOLOCE-7	3.0	42.9	31.5 46.7 –	$d = 0.8$ mm, $\varepsilon = 37\%$ $d = 0.89$ mm, $\varepsilon = 40\%$ $d = 1.07$ mm, $\varepsilon = 37\%$

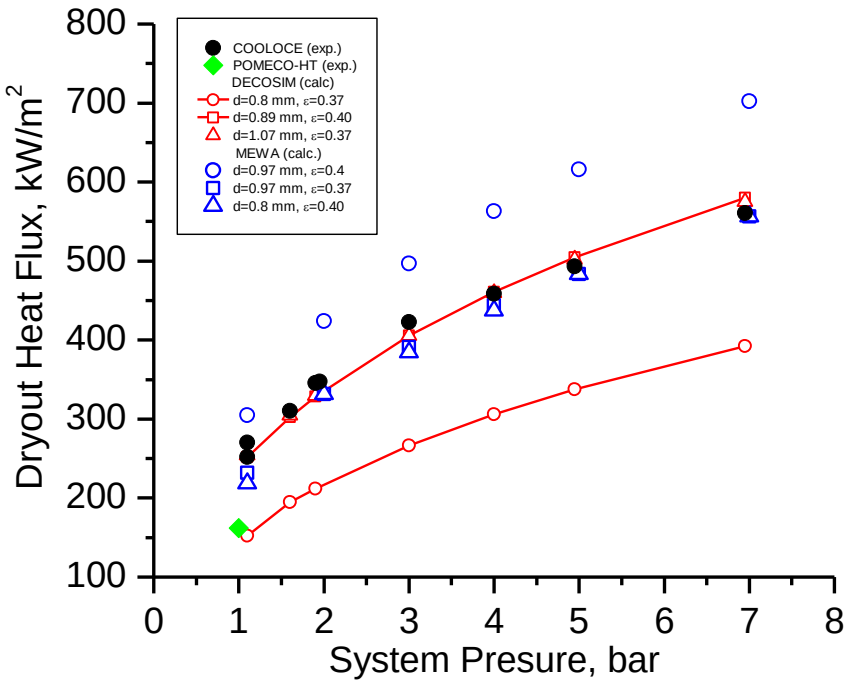

Figure 28: Comparison of calculated dryout heat power as function of system pressure (cylindrical debris bed) with COOLOCE experimens.

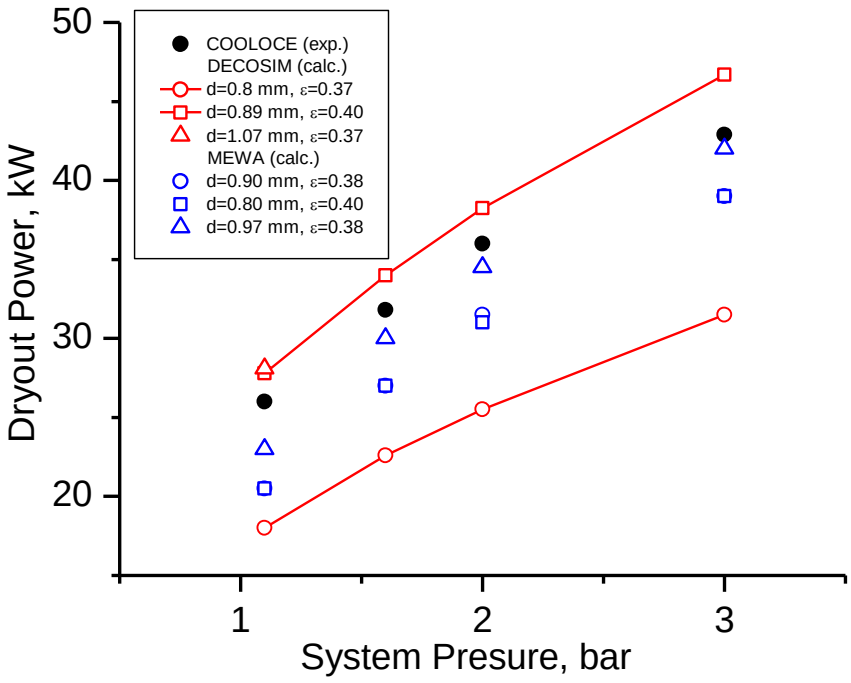

Figure 29: Comparison of calculated dryout heat power as function of system pressure (conical debris bed) with COOLOCE experimens.

3.6 Discussion of Results

The following conclusions can be derived from the experimental and simulation results presented in Figure 28 and Figure 29.

There is a clear discrepancy between the experimental dryout heat fluxes obtained in COOLOCE and POMECO-HT facilities at the atmospheric pressure. The dryout heat flux of 270 kW/m^2 was measured in COOLOCE facility at the system pressure 1.1 bar (see [63], [67]), while in POMECO-HT facility a significantly lower value of DHF 161.8 kW/m^2 was obtained [62] for the same material, though at a slightly lower system pressure 1.0 bar (see experimental point in Figure 28). The difference is of the order of 100 kW/m^2, or about 40% of the higher DHF value. The following possible reasons for this discrepancy can be named:

1. Difference in the system pressures (1.1 vs 1.0 bar). Judging from the experimental behavior of DHF as a function of system pressure, as well as simulations presented in Figure 28, this can be ruled out as the factor responsible for the difference in DHFs (e.g., two-fold increase in DHF can be reached only by increasing the system pressure from 1 to 5 bars).
2. Differences in debris bed properties. Experiments in both facilities were carried out with similar (although, technically, not the same) particles, Zirconium-silicate beads, which are analyzed in Section 4.2.1. The particles were purchased from the same manufacturer [4]. The size distributions analyzed by VTT and KTH teams turned out to be somewhat different, see Figure 38, with the average particles size estimated by VTT and KTH are 0.97 and 0.95 mm respectively, with the standard deviation 0.07 mm. The porosity estimated (although not measured directly) by VTT was 0.37 [1], whereas in the POMECO-HT facility the porosity obtained from the measured filled volume, density of material and the weight of the bed was found to be 0.371 [62]. The figures quoted imply that the properties of debris beds in both facilities were close enough and, per se, cannot be the main reason for the difference in measured DHFs.
3. Differences in geometry and heater arrangement. In COOLOCE facility, the debris bed was cylindrical (0.31 m in diameter, top surface area 0.07548 m^2, height 0.27 m, total volume 20 litres) and immersed in a water pool. In POMECO-HT facility, the debris bed was square in plan (0.2 m side, top surface area 0.04 m^2, height 0.25 m, total volume 10 litres), its side walls were thermally insulated. Therefore, the geometries seem to be comparable. However, the heaters in COOLOCE facility are

6.3 thicker mm and are oriented vertically, with the top 40 mm of the bed being unheated. In POMECO-HT, on the contrary, the heaters are 3mm thick and horizontal. It is estimated that the heaters occupy 2.5% of debris bed volume in COOLOCE, and 0.7% in POMECO-HT. It can be argued that vertical heaters can effectively create local "channels" in the debris bed providing pathways for vapor evacuation from the bed, which can explain higher dryout heat fluxes observed in COOLOCE facility. Also, effects of anisotropy of debris bed properties due to the presence of heaters are not clear at the moment.

The simulations carried out by DECOSIM code with the porosity 37% and effective particle diameter 0.8 mm determined from POMECO-FL experiments gave the dryout heat flux at the atmospheric pressure close to that measured in POMECO-HT facility (see the bottom curve in Figure 28). This might imply that the experimental conditions in POMECO-HT were close to those assumed in simulations (homogeneous debris bed with uniform heating of the material over the volume).

The dependence of DHF on system pressure from COOLOCE experiments can be reproduced quite accurately if either the effective particle diameter or debris bed porosity is increased. For a cylindrical debris bed, good agreement is achieved in DECOSIM simulations for the particle diameter 0.89 mm and porosity 0.4, see Figure 28. The results obtained are consistent with MEWA simulation results reported in [67] where larger particle diameters and porosities were found to be necessary to reproduce the experimental data on DHF.

For the conical debris bed, DECOSIM simulations with the baseline parameters (particle diameters of 0.8 mm and porosity 37%) underestimate the dryout heat flux, see Figure 29. On the other hand, simulations with the particle diameter 0.89 mm and porosity 0.4 overestimate the dryout heat flux by about 8%.

It is interesting to note that, despite the difficulty in predicting the absolute values of dryout heat flux due to high sensitivity of results to the values of debris bed porosity and particle diameter, the relative improvement of debris bed coolability for conical debris bed in comparison with flat (or cylindrical, behaving effectively as a flat) debris bed is captured quite well in the simulations. As an example, consider the results of recent DECOSIM simulations [70] performed for prototypic reactor conditions, rather than for small-scale

COOLOCE experiments. As the reference case, the following parameters were taken: $d = 1.5$ mm, $\varepsilon = 0.4$, pressure above the water level 1 bar, hydrostatic head of water at the cone tip 0.602 bar, mass of melt released is $M = 256$ t. Calculations were carried out in a cylindrical pool of the diameter $D_P = 12$ m, the density of corium was taken $\rho = 8285.1$ kg/m^3. The slope angle of the bed θ was varied from zero to 45^o, and depending on the slope angle, the debris bed was either conical (for large enough θ), or was comprised of a cone on a cylindrical base.

In Figure 30, the ratio of the dryout heat fluxes DHF for a conical debris bed, and the dryout heat flux for a flat debris bed with the same properties, DHF_0, is plotted. This ratio characterizes the relative improvement coolability of non-flat debris bed due to side ingress of water into the bed. On the same graph, points are shown for the slope angle θ = 47° of four COOLOCE experiments corresponding to system pressures of 1.1, 1.6, 1.9, and 3.0 bar. In the latter case, the experimental value of dryout heat flux for the cylindrical bed was taken as DHF_0. One can see that the agreement is quite reasonable, which can be regarded as partial validation of DECOSIM code and, as well, as an indication that the relative increase in DHF due to shape effects are captured correctly.

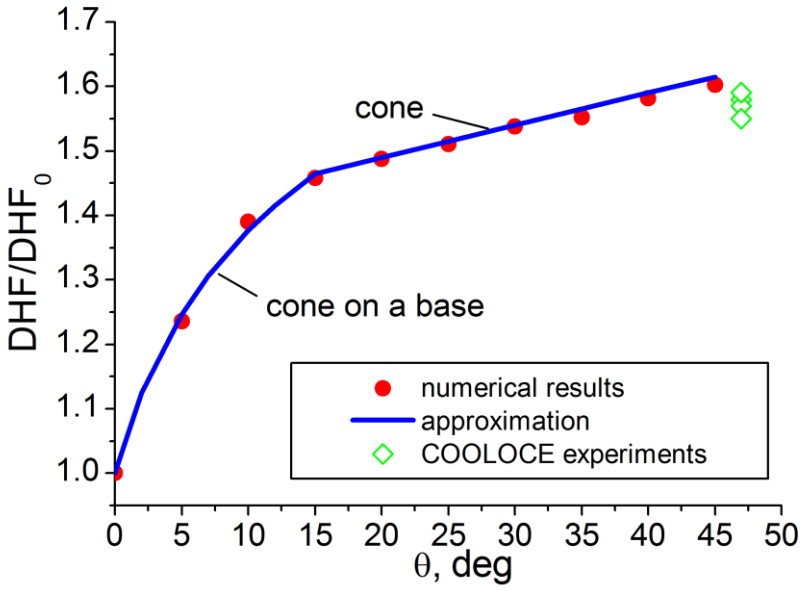

Figure 30: Dependence of ratio DHF/DHF_0 on the slope angle.

3.7 Further work

Further work will be focused on the application of drag model (modified Tung and Dhir's model) which takes into account the interphase drag; this will give an indication of the uncertainties related to the mathematical model. Cross-verification of DECSOIM and MEWA codes is planned by running more simulations of cone-shaped debris bed from COOLOCE experiments.

Simulations of cylindrical debris bed with permeable walls are under way, which will be compared with the experimental results from COOLOCE facility as they become available. Validation is also to be continued as new data will become available from POMECO-HT and POMECO-FL facilities.

4 Investigation of particulate debris spreading: possible effect of the heaters and thermocouples in COOLOCE facility

4.1 Goals and tasks

The goal of this task is to quantify time scale for particulate debris spreading. Experimental studies are performed at KTH in PDS-C facility with air injection from the bottom of the debris bed:

(i) to produce data for development and validation of the model for prediction of particulate debris spreading;
(ii) to assess the influence of the heaters and thermocouples on spreading of the particles used in COOLOCE facility at VTT.

4.2 Experimental approach and procedure

The geometry and total mass of the particle bed has no effect on the mass flux caused by the two-phase flow through the bed [3]. Until onset of fluidization, the bulk of the bed is immobile and the spreading is determined by relatively slow particle motion in a thin topmost layer of the bed. Thus the physical processes governing the spreading of the topmost layer are the same for any size of the bed. Therefore, there is no need to reproduce actual conical shaped of the bed used in COOLOCE test section. In the planar geometry of the PDS-C facility a slice of the COOLECE conical debris bed [1], [2] is considered. A few significant differences between the previous tests performed by VTT [2] and tests presented here are:

- VTT tests are focused on dryout of the non-movable conical bed;
- The geometry of the bed is realized by a conical net keeping the slope angle at about 45° well exceeding the critical angle of repose of spherical particles.
- In PDS tests air injection at the bottom of the bed is used to simulate steam flow.

4.2.1 Experimental facility

Experimental facility consist of the PDS-C test section and a mockup of the heaters and thermocouples (TC) used in COOLOCE tests performed by VTT [2].

PDS-C test section

PDS-C is a medium size experimental setup for separate effect tests on basic phenomena of particulate debris spreading at elevated gas-flow rates. It has been designed to provide

closures for particulate debris spreading at different gas injection flow rates. The closures are necessary for particulate debris spreading model validation and development.

The scheme of the setup is given in the Figure 31, Figure 32 and Figure 33. It is a vertical rectangular in cross section container made of Plexiglas with the dimensions of the active zone 73x405x915 mm. The bottom plate through which the air is injected into the active zone has 287 orifices ∅1.5 mm evenly distributed over the surface. The bottom plate is a part of aluminum rectangular pressurized compartment allowing gas fluxes up to 2.4 m/sec (flow rate up to 70 liters per second). The minimum gas flux providing the uniform gas injection over the injection plate is about 0.17 m/s (~5 L/s of the flow rate). The tests section commonly accommodates debris mass around 30-40 kg or volume up to 10 liters.

As an addition to test section, there is also a top flange (not shown in figures) mounted on top of the acrylic water tank. The flange prevents water being splashed out of the water tank. The flange has geometry of the box without two opposite sides through which injected air escapes. It's front and back sides are made of 3 mm thick aluminum plates.

PDS-C Facility Design Parameters (see Figure 31) are:

1. Fixed parameters:
   - Facility type: room temperature water/air facility.
   - Facility tests section material: Plexiglas.
   - Air injection provided through a perforated plate at the bottom.
2. Ranges of variable parameters:
   - Debris particles material:
     - Sand and gravel
     - Stainless steel.
     - Zirconium-silicate, ceramic or glass.
   - Volume of the debris bed (with porosity): up to 9 liters.
   - Air flow rate up to 70 L/s or 2.4 m/s superficial air velocity
   - Initial debris bed shape:
     - Right triangle
     - Isosceles triangle

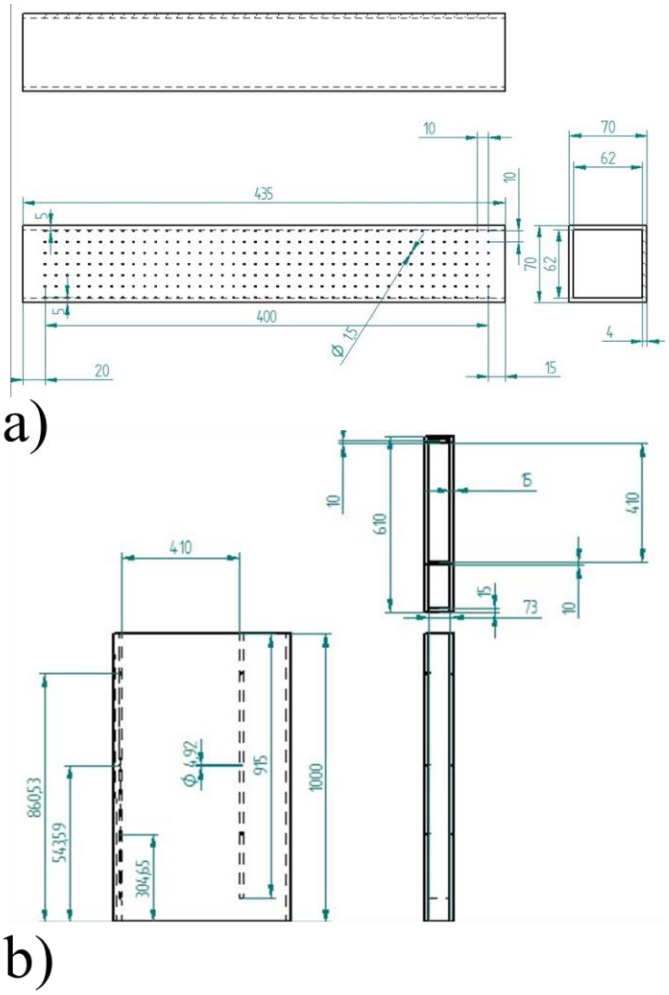

Figure 31: PDS-C drawings: air injection chamber (a) and acrylic body (b).

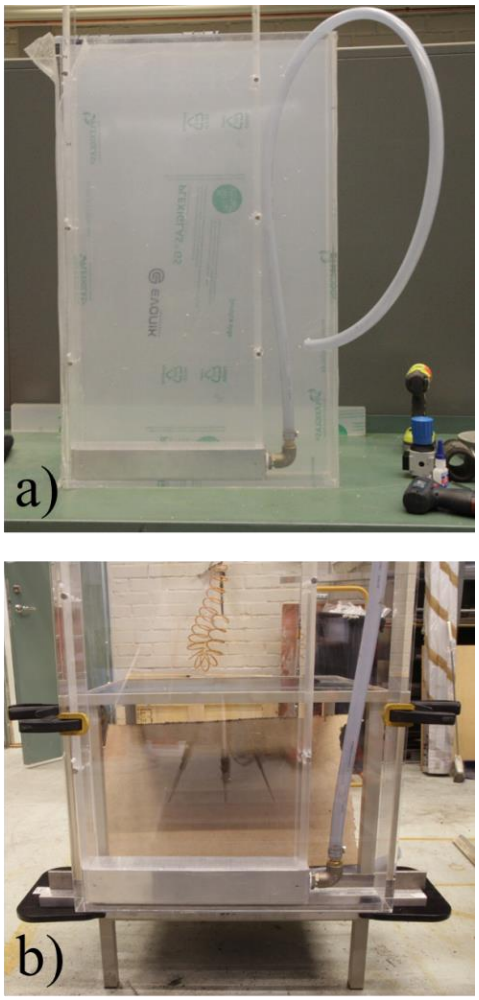

Figure 32: PDS-C facility: Manufactured (a) and installed (b).

Mockup of the COOLOCE heaters and TCs

In order to design the mockup of the heaters and TCs pins we followed the original arrangement of the heaters and TCs in COOLOCE-1 facility provided in the VTT report [1]. The scheme and photographic image of the heaters and TCs in COOLOCE-1 is shown in Figure 34(a-b). The pitch size between the mockups of the heaters and TCs is 25 mm. The external diameter of the heaters and TCs mockups is 6 and 2 mm respectively. As seen from Figure 34(a), the locations of the heater and TC pins are almost regular. Therefore, the mockup has two regular meshes of the pins corresponding to the 6 mm thick heaters and 2 mm thick TCs. The schematic of the pins holding plate of the mockup is shown in Figure 34(c). The plate lateral dimensions correspond to the:

- Dimensions of the PDS-C facility and its air injection chamber;
- Length of the slope of the silica-zirconia bed having a critical angle of repose close to 22º;

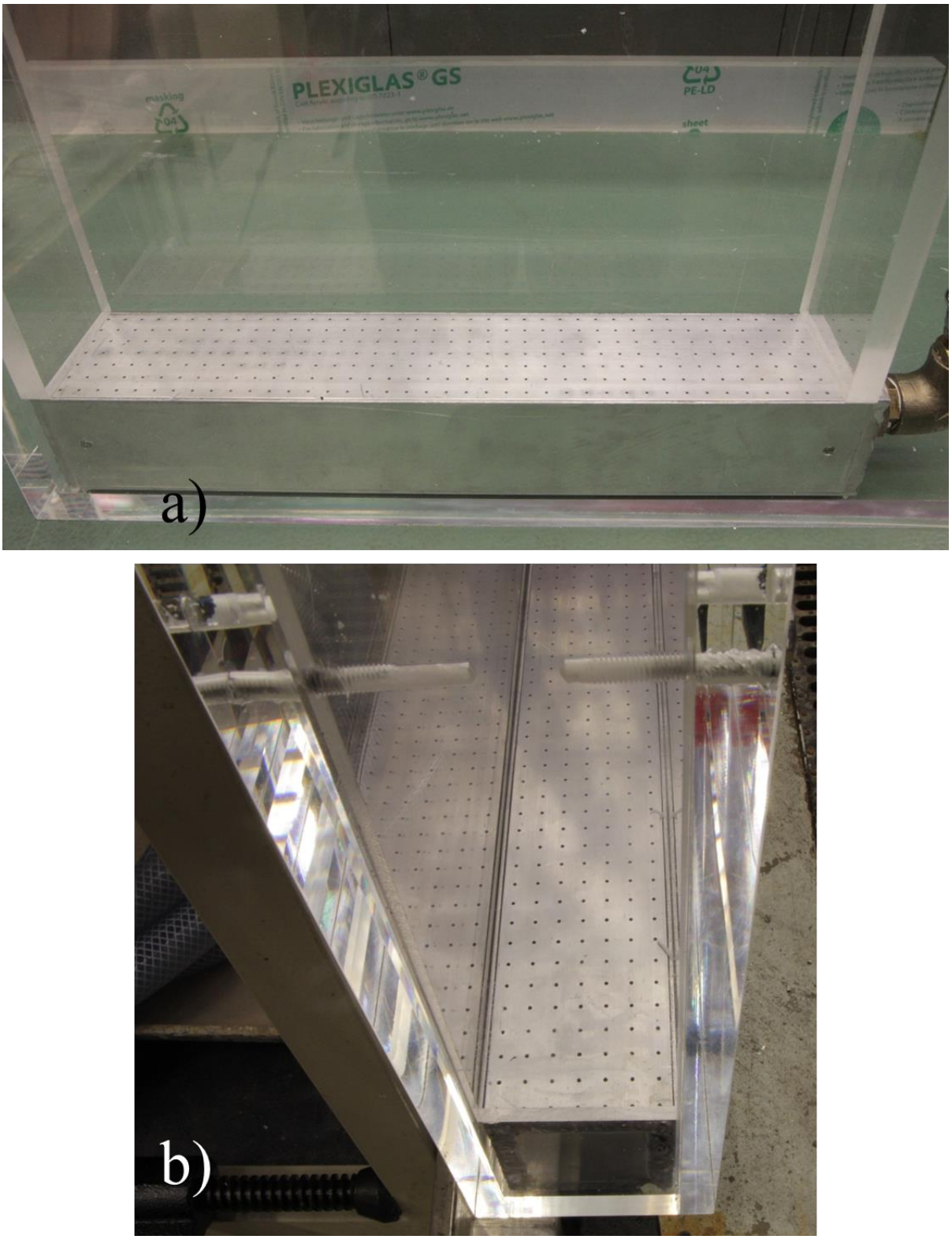

Figure 33: PDS-C test section (a) and its spreading plate (b).

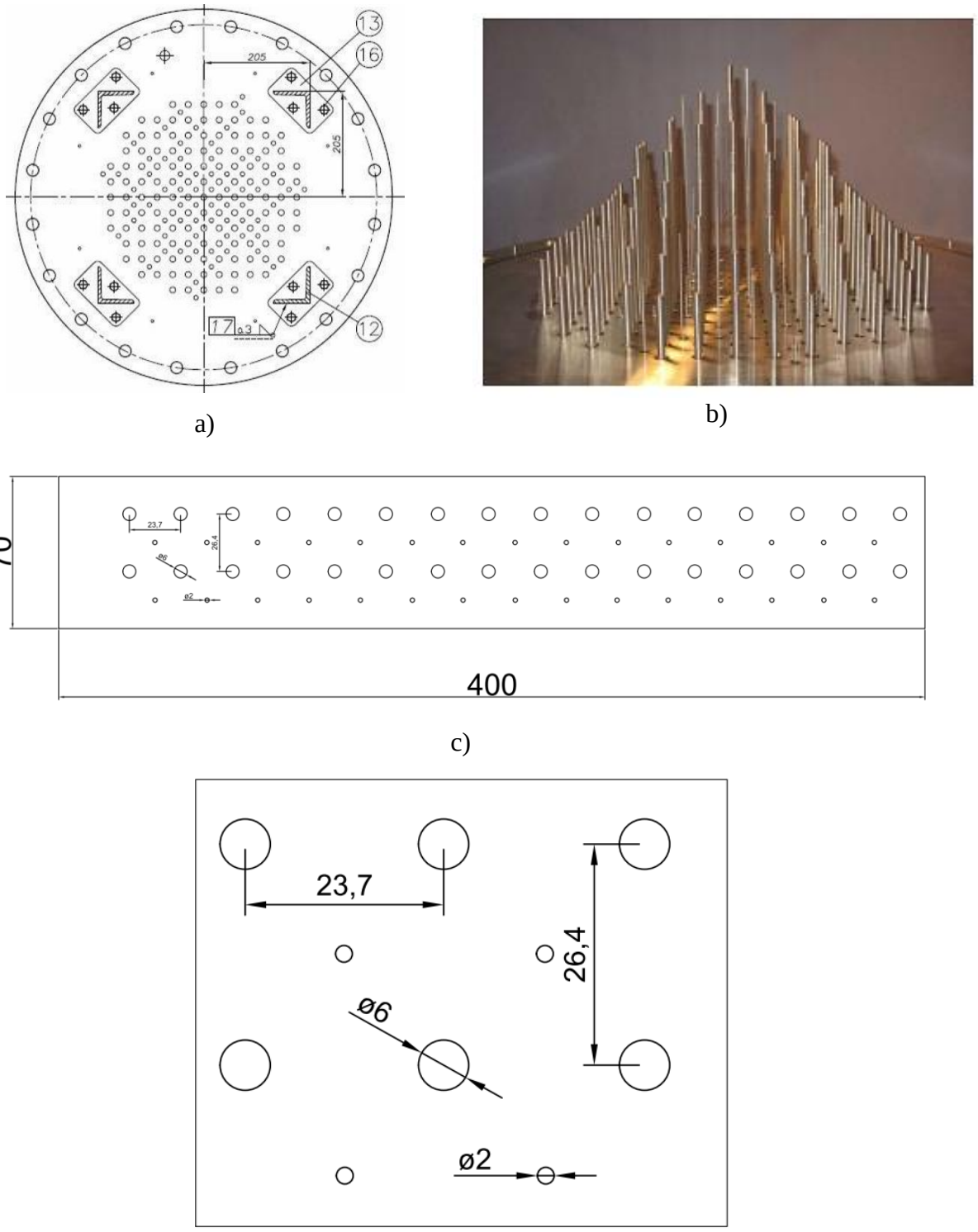

Figure 34: Schematics (a) and photographic image (b) of the heaters and TCs used in COOLOCE-1 facility [1]. Schematics of the pins arrangement in COOLOCE mockup: plate (c) and holes (d) dimensions together with pitch sizes.

The lateral pitch sizes for the pins are shown in Figure 34(d). As seen from Figure 34(d) the pitch sizes are different in transversal directions. This is due to inclined position of the pins

holding plate which is lying on top of the bed slope at angle close to critical angle of repose. When assembled, the pitch sizes of the vertically aligned pins in both lateral directions are the same. The assembled mockup is shown in Figure 35.

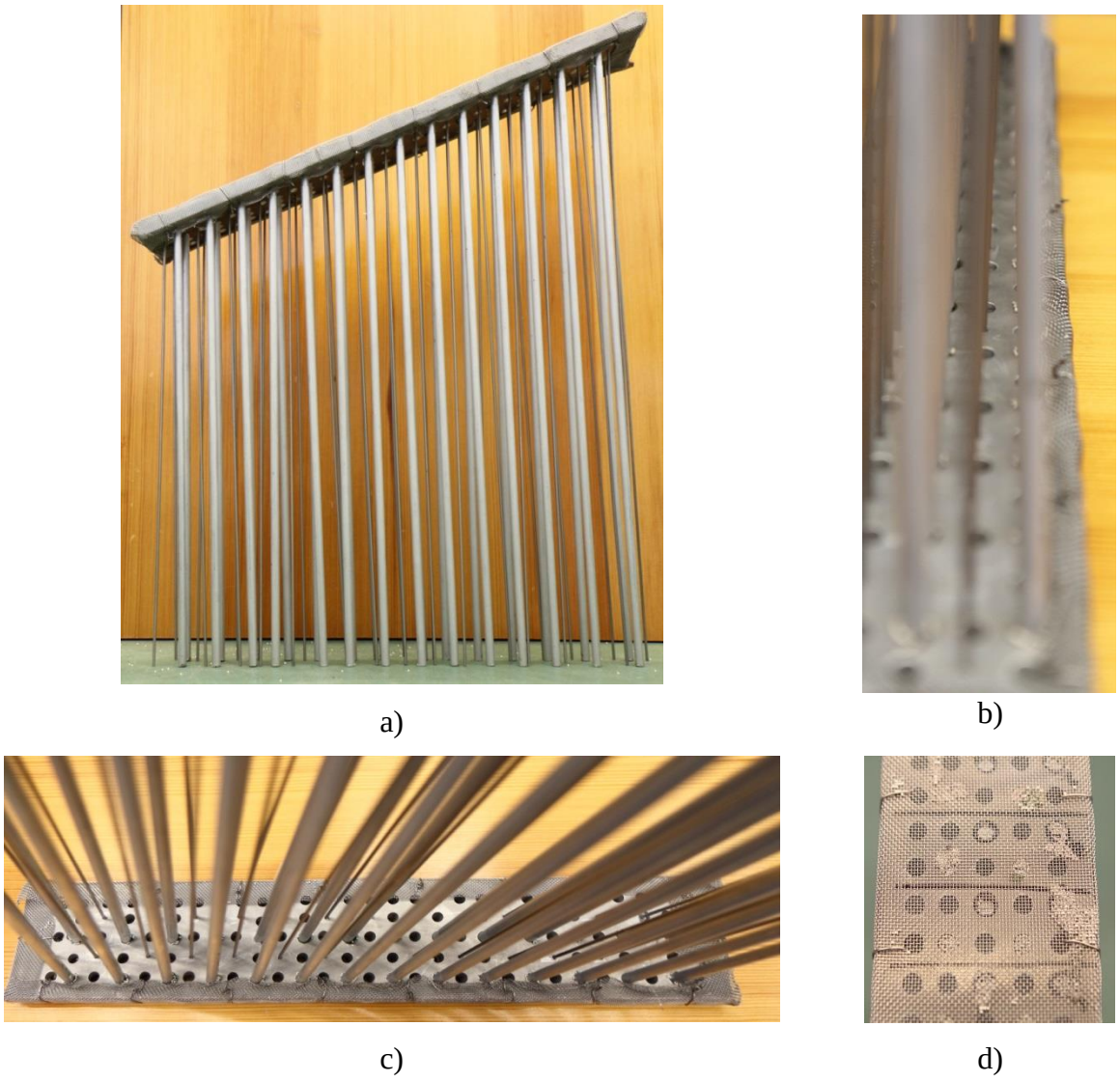

a) b) c) d)

Figure 35: COOLOCE heaters and TCs mockup: top (a) and side (b) views; pins holding plate with inner (c) and outer (d) perforated surfaces as well net protecting the particle through flow.

As shown in Figure 35(b-d) the pins holding plate is perforated with additional holes. The fine stainless steel net Figure 35(d) limits the particle flow through the perforated plate allowing only gas flow through additional holes in between pins. Beside the pins holding function, the perforated plate serves as a heap-holder.

Debris simulants: properties and characterization

As the debris simulants we use particles having different physical properties as well as size and morphology. Typical particulate debris used in PDS experiments are:

- Stainless steel cylinders, spheres and their mixtures;
- Sand gravel with size distribution and irregular morphology;
- Zirconium-silicate beads.

In this report we present the results performed with a latter particles, namely, the zirconium-silicate beads.

Zirconium-silicate beads

The VTT has performed series of tests with zirconium-silicate beads [1], [2]. For our tests we use the same beads purchased from the same supplier Alpine Hosokawa [4]. The main properties of the particles provided by supplier [4] are summarized in Figure 36(a). Size distribution of the beads in the ranges 0.8-1.0 mm is provided by manufacturer.

The size distribution of the beads has been analyzed by employing the image processing. The image (Figure 37a) of the 2001 particles has been filtered, color inverted (Figure 37b) and with MatLab image processing toolbox the average diameter of each recognized particles was estimated. The resulting statistics in beads size distribution is presented in Figure 38(a). For comparison, the size distribution of 960 beads analyzed by the VTT [5] is provided on the same graph. The cumulative fraction of the particles from both analyses is shown in Figure 38(b). A slightly larger fraction of the smaller particles in our analysis (vs VTT's) is an acceptable uncertainty and might be attributed to the measurement error. In either case the particles sizes are within the size distribution range specified by the supplier.

Data Sheet	Alpine Powerbeads SZS
Material	Zirconium Silicate sintered
Chemical Composition	ZrO_2 55 % SiO_2 35 % Al_2O_3 10 % Y_2O_3 traces HfO_2 traces
Specific weight	4.1 g/cm^3
Settled bulk density	2.5 g/cm^3
Hardness Mohs	7.2
Hardness HV5	9.4 MPa
Fracture toughness K_{IC}	2.8 MPam$^{1/2}$
Crushing load (2.0 - 2.5 mm)	1370 N
Crystallite size (av.)	370 nm
Roundness	97 %
Open porosity	0 %
Colour	white
Surface	satin finished

a)

b)

Figure 36: Properties (a) and image (b) of the 0.8-1.0 mm zirconium-silicate Alpine Powerbeads provided by supplier [4].

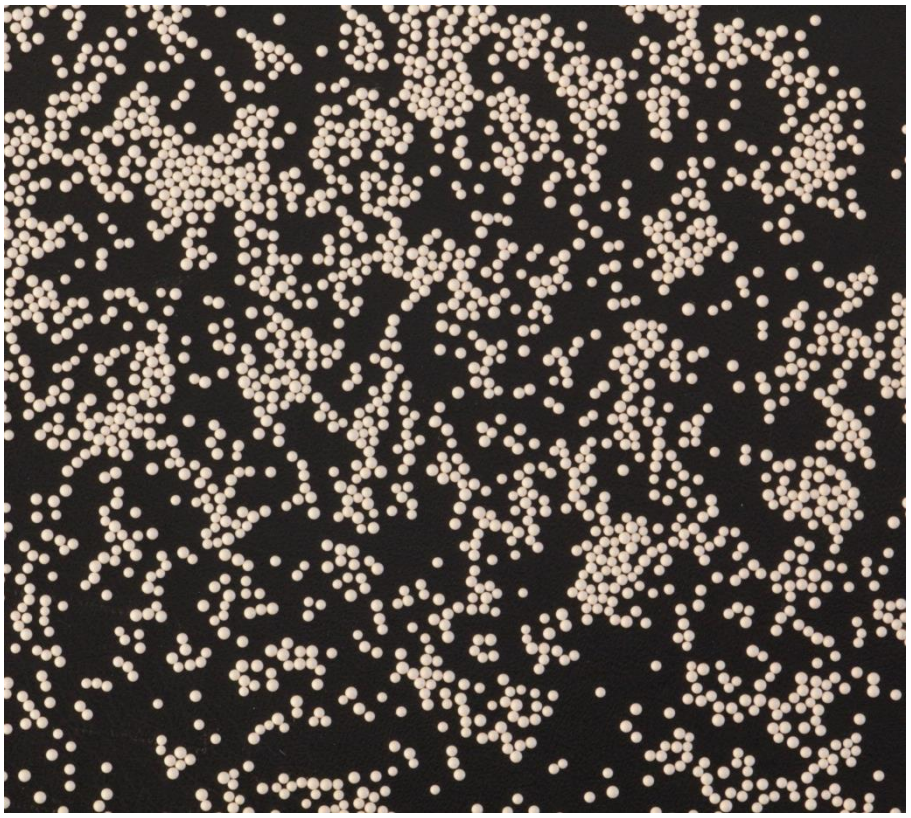

a)

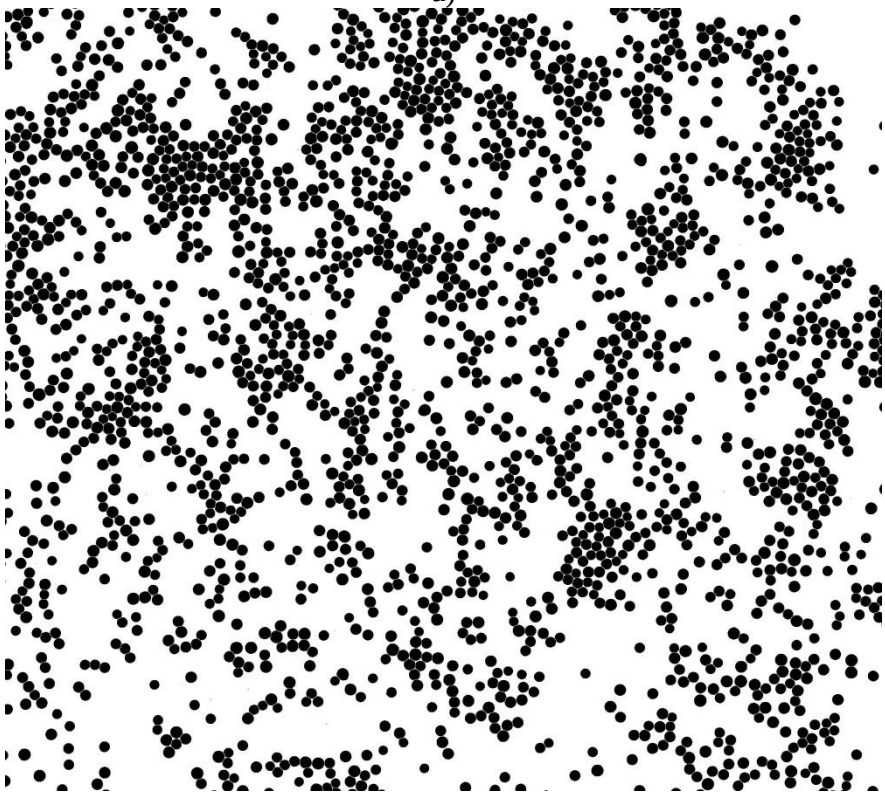

b)

Figure 37: Original (a), filtered and color inverted (b) images of the beads.

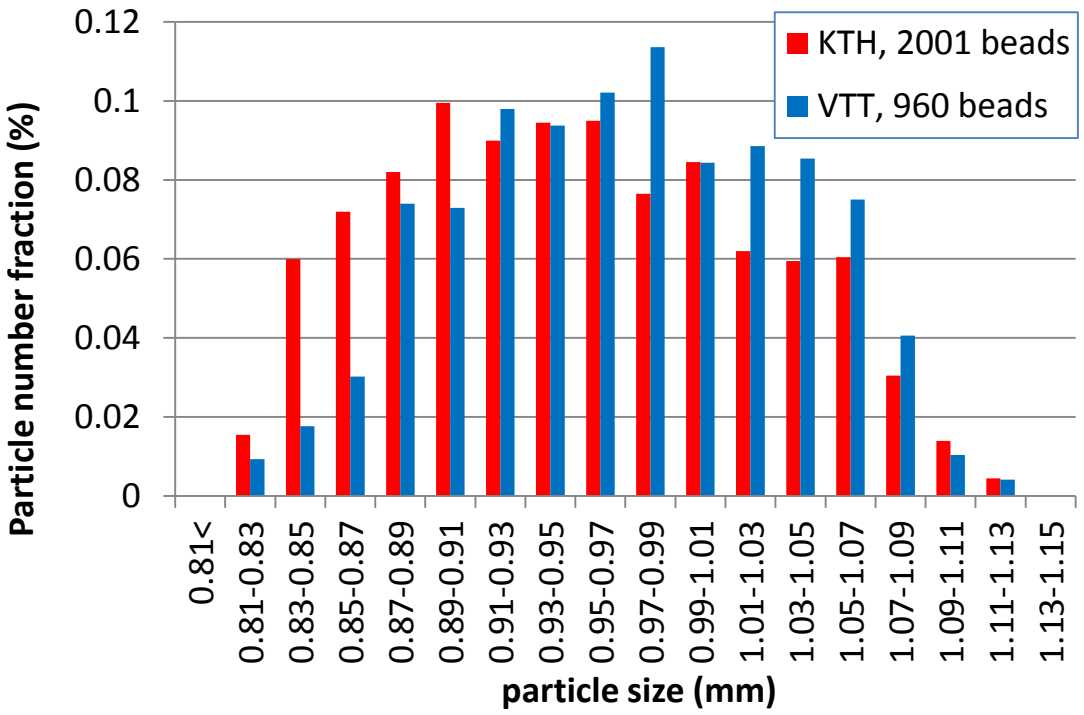

a)

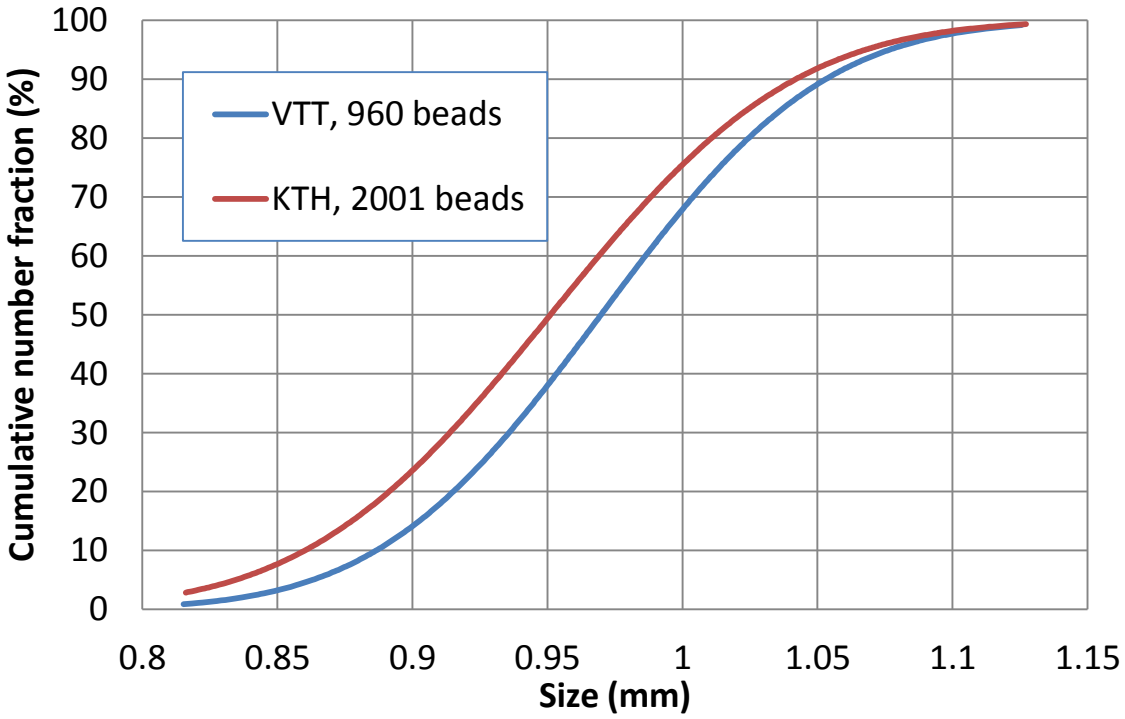

b)

Figure 38: Size distribution of the zirconium-silicate beads.

The number averaged particles size estimated by VTT and KTH are 0.97 and 0.95 mm respectively.

Experimental procedure

A typical measurement procedure used in PDS-C tests with and without (w/o) COOLOCE heaters and TC mockup is dscribed in this section. Both procedures consist of two phases: (i) debris bed preparation and (ii) test execution. In Table 9 and Table 10 important steps in the experimental procedures are provided for both types of the tests.

Table 9: Experimental procedure for preparation of the tests with and w/o mockup.

No	Step	Tests w/o mockup	Tests with mockup
1.	Installation of the COOLOCE heaters/TC mockup	-	+
2.	Particle filling	+	Is performed through a 30x70 mm opening between mockup plate and wall of the test section.
3.	Bed shaping with critical angle of repose	+	Not needed because mockup plate is at the critical angle of repose already.
4.	Installation of the heap-keeper and top flange	+	The mockup provides function of the heap holder.
5.	Plugging the opening for particle filling.	-	+
6.	Water pouring into facility	+	+
7.	Installation of the rulers for bed geometry measurements	+	+
8.	Installation of the video recording equipment	+	+

Table 10: Experimental procedures for running the tests with and w/o mockup.

1.	Activation of the video recording equipment, photographing bed and test section prior test.	+	+
2.	Activation of the gas injection at the desired flow rate	+	+
3.	Removal of the heap-keeper or lift of the mockup	Heap-keeper is removed from facility.	The mockup is lifted by ~20cm above the bed top surface.
4.			

The aforementioned (Table 9) *heap-keeper* is a perforated plate wrapped in a thin stainless steel net having the mesh size smaller than a particle size being used. The purpose of the heap-keeper is to prevent occurrence of so called *water piston effect* influencing the debris bed when gas injection is rapidly turned on. Prior the gas flow activation the porous volume of the debris bed is filled with water. Sudden gas flow activation leads to a fast momentum transfer from the gas to the water in the porous media. Since the porous media is a pile of particles (heap) the momentum is further transferred to them from the accelerated water flow. This process is far from being a prototypic to boiling and steam production in the corium debris bed caused by the decay heat at reactor scale. Therefore it has to be avoided. Such effect has been also observed by Cheng et al. in [6]. As a countermeasure authors proposed (i) gas pre-charge and (ii) pressure-adjustment approaches. The first method is discussed below. The second method requires significant modification of the test section complicating the design and operation of the facility.

A simplest solution would be to turn on gas injection controlling valve gradually from zero to a desired flow rate (pre-charge method used in [6]). In practice however, the time scale of the gas flow settling (slow process of the valve opening) can be much longer than the characteristic time scale of the particle self-leveling process. Essentially, this is valid for the high gas fluxes and low particle densities. Therefore, another method of the avoiding of the piston effect and its influence is to use the heap-holder allowing no particle flow when gas

injection is activated. After the establishment of the necessary gas flow the heap-holder is removed manually indicating the beginning of the measurements.

The main difference between operational procedures (given in Table 9) of the test with and without COOLOCE heaters/TCs mockup is that unlike to the heap-holder function described above, the mockup is not completely removed from the facility when experiment starts; instead, it is lifted-up above the debris bed while the pins (heaters/TCs mockup) remain inside the bed. In this way, we simulate the effect of the COOLOCE heaters and thermocouples resisting the particle flow. The effect of this resistance has been evaluated in our tests and results are presented in the following chapter.

4.3 Results and observations

In total 13 tests were performed: ten without the COOLOCE heaters/TC mockup and three with mockup. The test conditions and results are summarized in Table 11.

Table 11: Results from tests with- and without COOLOCE heaters/TCs mockup performed in PDS-C facility on self-leveling of the 0.8-1 mm zirconium-silicate beads.

Total air flow rate (L/s)	Superficial velocity (m/s)		Self-leveling time (s)						
	Air	Steam (assessed)	Experiments with mockup	Experiments w/o mockup					
			Tests 1-3	Tests 4-6	Tests 7-9	Tests 10-12	Test 13	mean	Standard deviation σ (s)
5	0,17	0,25	**19,2**	21,9	21,8	20,8	-	**21,50**	0,50
10	0,34	0,50	**4**	3,6	8,1	4,2	3,6	**4,88**	1,88
15	0,52	0,77	**3,9**	4	4,4	3,8	-	**4,07**	0,25

As seen from Table 11 the total air flow rate is fixed to 5, 10 and 15 L/s which correspond to the superficial velocity of the air ranging from 0.17 up to 0.52 m/s. As estimated in APPENDIX 1 the fluidization velocity of the bed consisting 0.95 mm large zirconium-silicate beads is about 0.62 m/s. The highest value of the air superficial velocity reached in our tests is 0.52 m/s. In our early studies with stainless steel particles [3] we found that the bed partial fluidization already takes place at the gas velocity equal to ~70% of the theoretical value estimated from Eq. (3) in APPENDIX 1. Indeed, for the zirconium-silicate particle pile we

observed similar phenomenon. The top of the bed is near its fluidization limit at 15 L/s total flow (0.52 m/s). This fact may explain why at the highest superficial velocity the tests with- and without COOLOCE heaters/TCs mockup show the same self-leveling time as presented in Figure 39. Note, the corresponding superficial velocity of the steam given in Table 11 and on upper axis in Figure 39 is calculated from expression (7) (APPENDIX 1).

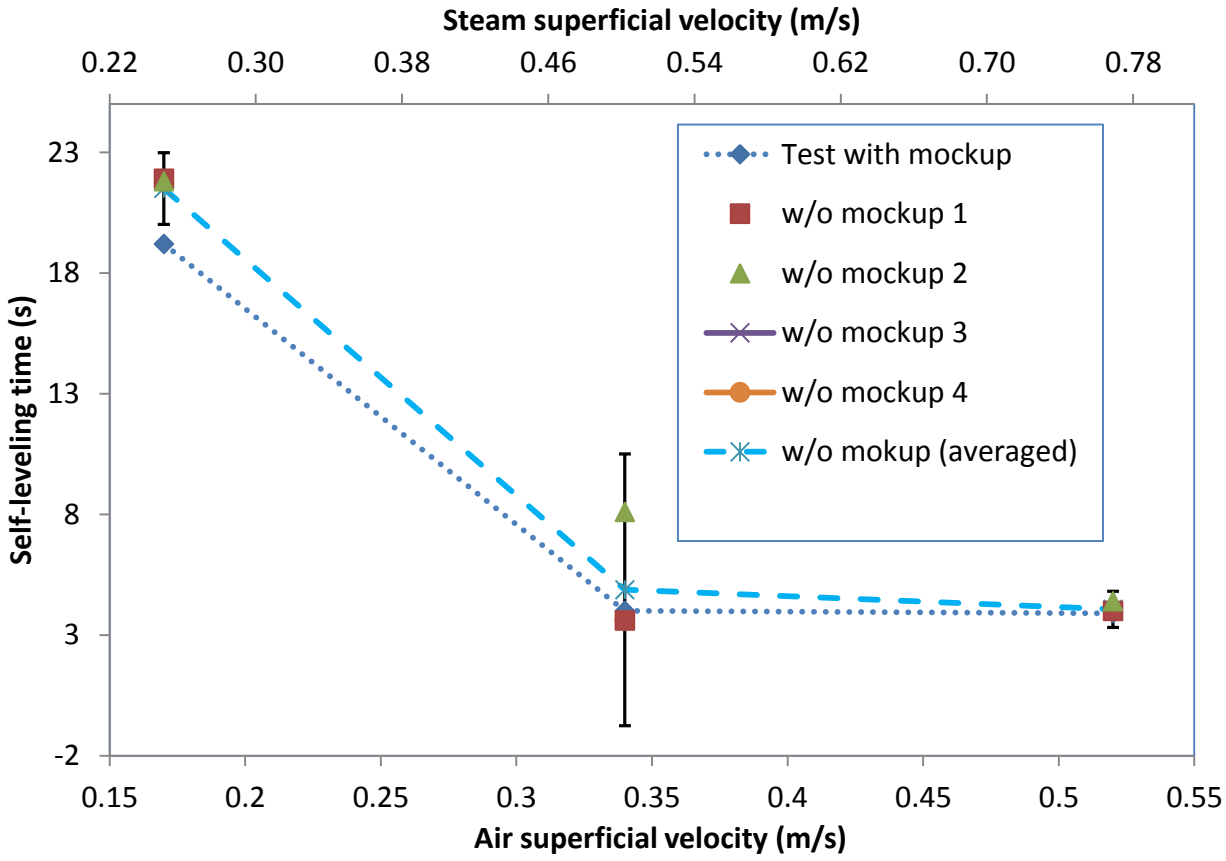

Figure 39: Results from the tests with zirconium-silicate beads: 3 tests with mockup and 10 tests w/o mockup are grouped in 4 groups. The error bars correspond to the tripled standard deviation $\pm 3\sigma$ of the characteristic self-leveling time.

For the lowest 0.17 m/s superficial velocity of the air the effect of the COOLOCE heaters/TCs mockup is noticeable. Surprisingly, at this point the particle self-leveling process with presence of the mockup is slightly faster than w/o it. Possible explanations of the observed phenomenon are:

- The partial extraction of the COOLOCE heaters/TCs mockup from the bed (see "Experimental procedure") may influence beads self-leveling by enhancing the downslope particle flux at the very beginning of the test.
- The heaters/TCs mockup pins may influence the local two-phase currents enhancing the turbulent flows which, again, might slightly increase particle flux.

Nevertheless, assuming that the measurement uncertainty of the test with and w/o mockup is the same, the self-leveling time for either case is almost the same. In other words, the light blue dashed line (single test per air velocity point, with mockup) and the blue dotted line (averaged between tests, w/o mockup) are both within the ranges of the experimental errors (Figure 39).

4.3.1 Fluidization velocities of the zirconium-silicate bed

Following the approach presented in APPENDIX 1 we calculate the minimum fluidization velocities of the zirconium-silicate beads by air and steam. In these calculations properties of the bead are used as shown in Figure 36 and Figure 38, and gas properties are calculated at atmospheric pressure and temperature of 20°.

Table 12: Minimum fluidization velocities of the zirconium-silicate beds by air and steam.

Gas	**Minimum fluidization velocity u_{mf} (m/s)**
Air	0.62
Steam	0.92

4.4 Conclusions and outlook

In total 13 exploratory tests were carried out to clarify the influence of the COOLOCE heaters and TCs mockups on particle self-leveling process. Results of the preliminary analysis suggest that there is no significant influence of the mockup pins on self-leveling, at least for the air superficial velocities ranging from 0.17 up to 0.52 m/s. There is a tendency, which might be within experimental error however, that the heaters and TCs pins may even enhance the particle self-leveling process at lower superficial velocities of the gas (<0.17 m/s for air and <0.24 m/s for steam). This finding is counterintuitive and need to be confirmed by performing more tests at even lower gas injection rates. For that, the gas injection chamber used in PDS-C facility must be redesigned in order to achieve uniform air injection below 0.17 m/s (see complete specs of the PDS-C facility in 4.2.1).

The PDS-C tests reported herein were carried out in a configuration when COOLOCE heaters/TCs mockup pins are extended over the debris bed top surface. In the previous VTT studies [1]-[2] the heaters and TCs tips are below the bed top surface. If the future self-leveling tests will be performed in the same (VTT) configuration then there will be no influence of the heaters/TCs on self-leveling process, at least at the initial stage of spreading. As it was mentioned [3] the only top most layer of the pile of particles is movable while the bed bulk is immobile. This is valid for the case when gas superficial velocity is below bed's minimum fluidization velocity.

5 REFERENCES

[1] Takasuo E., Kinnunen T., Pankkoski H. and Holmström S., "Description of the COOLOCE test facility – Conical particle bed", VTT report VTT-R-08956-10 (2010).

[2] Takasuo E., Kinnunen T., Pankkoski H. and Holmström S., reports VTT-R-07097-11 and VTT-R-02427-11 on experiments on coolability of conical particle bed, VTT (2011).

[3] Konovalenko A., Basso S., Karbojian A. and Kudinov P., "Experimnetal and Analytical Study of the Particulate Debris Bed Self-leveling", NUTHOS-9, N9P0305 (2012).

[4] Alpine Hosokowa supplier of the powerbeads, http://www.alpinehosokawa.com

[5] Private communication with VTT.

[6] Cheng A. *et al*, "An experimental investigation on self-leveling behavior of debris beds using gas injection", Experimental Thermal and Fluid Science, 48, pp. 110-121 (2013).

[7] Yakush S., Lubchenko N., and Kudinov P., "Risk-Informed Approach to Debris Bed Coolability Issue," Proceedings of the 20th International Conference on Nuclear Engineering (ICONE-20), Anaheim, CA, USA, July 30 - August 3, Paper 55186 (2012).

[8] Hofmann G., "On the location and mechanisms of dryout in top-fed and bottom-fed", Nuclear Technology, 65, (1984).

[9] Zhang J.-P., Epstein N., Grace J. R., "Minimum fluidization velocities for gas-liquid-solid three phase systems", Powder Technology, 100(2-3), pp. 113-1118, (1998).

[10] Yakush S., Lubchenko N., and Kudinov P., "Surrogate models for debris bed dryout", NURETH15-278, (2013).

[11] Britter R.E., "The spread of a negatively buoyant plume in a calm environment," *Atmospheric Environment*, 13, pp. 1241-1247, 1979.

[12] Budu A., "Debris Bed Formation at Low Temperature (DEFOR-LT experiment): Coolant flow influence on debris packing," SARNET mobility research report, Division of Nuclear Power Safety KTH, Stockholm, 2008.

[13] Dombrovsky L.A., Davydov M.V., Kudinov P., "Thermal radiation modeling in numerical simulation of melt-coolant interaction," Comp. Therm. Sci. **1** (1) 2009, pp. 1-35.

[14] Dombrovsky L.A., Davydov M.V., and Kudinov P., Thermal radiation modeling in numerical simulation of melt-coolant interaction, Proc. Int. Symp. Adv. Comput. Heat Transfer (CHT-08), May 11–16, 2008, paper 155.

[15] Dinh T.N., Konovalikhin M.J., Sehgal B.R., "Core melt spreading on a reactor containment floor," Progress in Nuclear Energy, 36 (4), pp. 405-468, 2000.

[16] Frid W. and Kudinov P., "Ex-Vessel Melt Coolability Issue in BWRs with Deep Water Pool in Lower Drywell," OECD/NEA MCCI Seminar 2010, Cadarache, France, 15th - 17th November, 2010.

[17] Frost D.L., Brucker B., Ciccarelli P., "Effect of Boundary Conditions on the Propagation of a Vapor Explosion in Stratified Molten Tin/Water Systems," Nuclear Engineering and Design 155, 311-333, 1995.

[18] Fröhlich G., "Interaction Experiments between Water and hot Melts in Entrapment and Stratification Configurations," Chemical Geology, 62, 137-147, 1987.

[19] Herbert E., "The propagation of two-dimensional and axisymmetric viscous gravity currents over a rigid horizontal surface," *J. Fluid Mech.*, **121**, pp. 43-58, 1982.

[20] Huppert H., "Flow and instability of a viscous current down a slope," *Nature*, **300**, pp. 427-429, 1982.

[21] Karbojian A., Ma W.M., Kudinov P., Davydov M. and Dinh N., "A scoping study of debris formation in DEFOR experimental facility", 15th International Conference on Nuclear Engineering, Nagoya, Japan, April 22-26, 2007, Paper number ICON15-10620.

[22] Karbojian A., Ma W., Kudinov P., and Dinh T.-N., "A Scoping Study of Debris Bed Formation in the DEFOR Test Facility", Nuclear Engineering and Design, **239**, 2009, 1653-1659.

[23] Kudinov P. and Davydov M., "Approach to Prediction of Melt Debris Agglomeration Modes in a LWR Severe Accident," Proceedings of ISAMM-2009, Böttstein, Switzerland, October 26 - 28, 2009.

[24] Kudinov P. and Davydov M., "Development of Ex-Vessel Debris Agglomeration Mode Map for a LWR Severe Accident Conditions," Proceedings of the 17th International Conference on Nuclear Engineering, July 12-16, 2009, Brussels, Belgium, Paper ICONE17-75080.

[25] Kudinov P. and Davydov M., "Development and Validation of the Approach to Prediction of Mass Fraction of Agglomerated Debris," The 8th International Topical Meeting on Nuclear Thermal-Hydraulics, Operation and Safety (NUTHOS-8), Shanghai, China, October 10-14, N8P0298, 2010.

[26] Kudinov P. and Dinh T.-N., "A Computational Study of Debris Bed Formation," ANS Transactions, 2008, paper 193463.

[27] Kudinov P. and Dinh T.-N., "An analytical study of mechanisms that govern debris packing in a LWR severe accident", The 12th International Topical Meeting on Nuclear Reactor Thermal Hydraulics (NURETH-12), Sheraton Station Square, Pittsburgh, Pennsylvania, U.S.A. September 30-October 4, 2007. Paper 247.

[28] Kudinov P., Karbojian A., Ma W.M., Davydov M., and Dinh T.-N., "A Study of Ex-Vessel Debris Formation in a LWR Severe Accident", Proceedings of ICAPP 2007, Nice, France, May 13-18, 2007, Paper 7512.

[29] Kudinov P., Karbojian A., Ma W.M., Dinh T.-N., *"The DEFOR-S experimental study of defris formation with corium simulant materials,"* Nuclear Technology, **170**, 2010.

[30] Kudinov P., Karbojian A., Ma W., and Dinh T.-N. "The DEFOR-S Experimental Study of Debris Formation with Corium Simulant Materials," Nuclear Technology, 170(1), April 2010, pp. 219-230, 2010.

[31] Kudinov, P., Karbojian, A., Tran, C.-T., Villanueva, W., "Experimental Data on Fraction of Agglomerated Debris Obtained in the DEFOR-A Melt-Coolant Interaction Tests with High Melting Temperature Simulant Materials," Nuclear Engineering and Design, under review, 2013.

[32] Kudinov P., Karbojian A., Tran C.-T., "Experimental Investigation of Melt Debris Agglomeration with High Melting Temperature Simulant Materials," Proceedings of ISAMM-2009, Böttstein, Switzerland, October 26 - 28, 2009.

[33] Kudinov P., Karbojian A., Tran C.-T., Villanueva W., "The DEFOR-A Experiment on Fraction of Agglomerated Debris as a Function of Water Pool Depth," The 8th International Topical Meeting on Nuclear Thermal-Hydraulics, Operation and Safety (NUTHOS-8), Shanghai, China, October 10-14, N8P0296, 2010.

[34] Kudinov P., Karbojian A., Ma W.M., and Dinh T.-N., "An experimental study on debris formation with corium simulant materials," Proc. ICAPP'08, Anaheim, CA USA, June 8–12, 2008, paper 8390.

[35] Kudinov P. and Kudinova V., "Influence of Water Subcooling on Fracture of Melt Debris Particle," ANS Transactions, 2009, paper 210646.

[36] Kudinov P., Ma W.M., Tran C.-T., Hansson R., Karbojian A., Dinh T.-N. "Multiscale Phenomena of Severe Accident," NKS-R and NKS-B Joint Summary Seminar, Armémuseum, Stockholm, 26th - 27th March 2009.

[37] Kudinov P., "Decomposition, Validation and Synthesis in Multiscale Problems of Severe Accident Analysis," Verification and Validation for Nuclear Systems Analysis Workshop, Center for Higher Education, Idaho Falls, ID, July 21 - July 25, 2008.

[38] Kudinov P., Kudinova V., and Dinh T.-N., "Molten Oxidic Particle Fracture during Quenching in Water," 7th International Conference on Multiphase Flow ICMF 2010, Tampa, FL USA, May 30-June 4, 2010.

[39] Lundström P., Tuomisto H. and Theofanous T.G., "Integration of severe accident assessment and management to fulfill the safety goals for the Loviisa NPP," International Topical Meeting on Probabilistic Safety Assessment, Park City, Utah, USA, September 29 - October 3, 1996.

[40] Morris M. D., "Factorial sampling plans for preliminary computational experiments," *Technometrics*, Vol. 33, No. 2, 1991, pp. 161–174.

[41] PLINIUS FP6. Final Report. "Transnational Access to the Prototypic Corium Platform PLINIUS", http://www.plinius.eu

[42] Saltelli A., Tarantola S., Campolongo F., Ratto M., Sensitivity Analysis in Practice. John Wiley & Sons, Ltd, 2004, 94 p.

[43] Shetty S. A. and Cerro R. L., "Spreading of a point source over inclined solid surfaces," *Ind. Eng. Chem. Res.*, **34**, pp. 4078-4086, 1995.

[44] Theofanous T. G., "On Proper Formulation of Safety Goals and Assessment of Safety Margins for Rare and High-Consequence Hazards," Reliability Engineering and System Safety 54, pp. 243-257, 1996.

[45] Theofanous T. G. and Dinh T.-N., "Integration of multiphase Science and Technology with Risk management In Nuclear Power reactors: Application of the Risk-Oriented Accident Analysis Methodology to the Economic, Simplified Boiling Water Reactor Design," Multiphase Science and Technology, V20(2), Pages 81-211, 2008.

[46] Vella D. and Huppert H. E., "Gravity currents in a porous medium at an inclined plane," *J. Fluid Mech.*, **555**, pp. 353-362, 2006.

[47] Yakush S. and Kudinov P., "Simulation of Ex-Vessel Debris Bed Formation and Coolability in a LWR Severe Accident," Proceedings of ISAMM-2009, Böttstein, Switzerland, October 26 - 28, 2009.

[48] Yakush S. and Kudinov P., "Transient Phenomena of Ex-vessel Debris Bed Formation in a LWR Severe Accident," ANS Transactions, 2009, paper 210830.

[49] Yakush S., Kudinov P., and Dinh T.-N., "Modeling of Two-Phase Natural Convection Flows in a Water Pool with a Decay-Heated Debris Bed," Proc. ICAPP'08, Anaheim, CA USA, June 8–12, 2008, paper 8409.

[50] Yakush S., Kudinov P., and Dinh T.-N., "Multiscale Simulations of Self-organization Phenomena in the Formation and Coolability of Corium Debris Bed," Proc. The 13th

International Topical Meeting on Nuclear Reactor Thermal Hydraulics (NURETH-13), September 27-October 2, 2009. Kanazawa City, Ishikawa Prefecture, Japan, Paper N13P1143.

[51] Robb K., Corradini M., "Melt eruption modeling for MCCI simulations", *The 14th International Topical Meeting on Nuclear Reactor Thermalhydraulics, NURETH-14 290,* Toronto, Ontario, Canada, September 25-30 (2011).

[52] Yakush S., Lubchenko N., and Kudinov P., "Risk-Informed Approach to Debris Bed Coolability Issue," Proceedings of the 20th International Conference on Nuclear Engineering (ICONE-20), Anaheim, CA, USA, July 30 - August 3, Paper 55186 (2012).

[53] Yakush S. and Kudinov P., "Effects of Water Pool Subcooling on the Debris Bed Spreading by Coolant Flow," ICAPP Proc., Paper 11416, 2011.

[54] Hofmann G., "On the location and mechanisms of dryout in top-fed and bottom-fed", Nuclear Technology, 65, (1984).

[55] Zhang J.-P., Epstein N., Grace J. R., "Minimum fluidization velocities for gas-liquid-solid three phase systems", Powder Technology, 100(2-3), pp. 113-1118, (1998).

[56] Kubasch Jens H., "Bubble Hydrodynamics in Large Pools", PhD thesis, ETH, Zurich, (2001).

[57] Ergün S., "Fluid Flow through Packed Columns," *Chemical Engineering Progress,* Vol. 48, 2, pp. 89-94 (1952).

[58] Reed A.W., "The Effect of Channelling on the Dryout of Heated Particulate Beds Immersed in a Liquid Pool," Ph.D. Thesis, Massachusetts Institute of Technology, Cambridge, 1982.

[59] Bürger M., Buck M., Schmidt W., and Widmann W., "Validation and Application of the WABE code: Investigations of Constitutive Laws and 2D effects on Debris Coolability," Nuclear Engineering and Design, Vol. 236, pp. 2164–2188 (2006).

[60] Hu K. and Theofanous, T.G., "On the Measurement and Mechanism of Dryout in Volumetrically Heated Coarse Particle Beds," Int. J. Multiphase Flow, Vol. 17, No. 4, pp. 519–532 (1991).

[61] IAPWS, The International Association for the Properties of Water and Steam, http://www.iapws.org.

[62] Thakre S., Ma W., Kudinov P., and Bechta S., "Study on Effective Particle Diameters and Coolability of Particulate Beds Packed with Irregular Multi-size Particles," APRI-8, NKS-DECOSE Project Report, 2013.

[63] Takasuo E., Kinnunen T. Pankakoski P.H., Holmström S., "The COOLOCE particle bed coolability experiments with a cylindrical geometry: Test series 3–5," Research Report VTT-R-07099-11. Espoo, 2011. 27 p.

[64] Takasuo E., Kinnunen T. Pankakoski P.H., Holmström S., "The COOLOCE particle bed coolability experiments with a conical geometry: Test series 6–7," Research Report VTT-R-07097-11. Espoo, 2011. 26 p.

[65] Takasuo E., Kinnunen T., and Holmström S., "COOLOCE particle bed coolability experiments with a cylindrical test bed: Test series 8–9," Research Report VTT-R-07224-12. Espoo, 2012. 44 p.

[66] Takasuo E., Holmström S., Kinnunen T., and Pankakoski P.H., "The COOLOCE experiments investigating the dryout power in debris beds of heap-like and cylindrical geometries," Nuclear Engineering and Design 250 (2012), p. 687-700.

[67] Takasuo E., "Debris Coolability Simulations with Different Particle Materials and Comparisons to COOLOCE Experiments," VTT report VTT0R-00257-13 (2013).

[68] Tung, V.X. and Dhir, V.K., "A hydrodynamic model for two-phase flow through porous media," Int. J. Multiphase Flow Vol. 14, No. 1, pp. 47–65 (1988).

[69] Schmidt W., "Interfacial drag of two-phase flow in porous media," Int. J. Multiphase Flow, Vol. 33, pp. 638–657 (2007).

[70] Yakush S.E., Lubchenko N.T., and Kudinov P., "Surrogate Models for Debris Bed Dryout," Proc. 15th International Topical Meeting on Nuclear Reactor Thermalhydraulics (NURETH-15), paper NURETH15-278, 16 pp.

APPENDIX 1

Gas superficial velocities reachable in PDS-C facility

In order to provide comprehensive assessments of efficacy of the particulate debris spreading, as one of the SA mitigation strategy, we have to reach air superficial velocities comparable with prototypic steam velocities. Here we perform rough estimation of the steam superficial velocities which can be achievable with steam simulant (air) in PDS-C facility. Another words, we would like to answer the question: what part of the debris bed we can simulate in the PDS-C facility in terms of superficial velocities?

Velocity of the steam flowing out at the debris bed top is a crucial parameter for the debris bed spreading. Consider a steam generating (at atmospheric pressure) corium debris bed with properties chosen within the typical ranges considered in [8], [7].

Table 13: Steam generating debris bed properties.

Debris volume	Initial bed length, L	Initial bed height, h	Porosity, ε	Slope angle, θ	Specific heat release, W	Particle density, ρ_p	Steam density, ρ_s	Latent heat of evaporation, H_e
20 m^3	4 m	2.8	0.5	35°	240 W/kg	8000 kg/m^3	0.59 kg/m^3	2.258 MJ/kg

Assuming uniform heat generation in the debris bed, the heat flux to be removed from the bed with local height h is:

$$Q_{HF}(h) = \rho_p \cdot (1-\varepsilon) \cdot W \cdot h \quad (1)$$

Then the steam superficial velocity v_{steam} as function of the bed height h can be estimated as:

$$v_{steam}(h) = \frac{Q_{HF}(h)}{\rho_s \cdot H_e} \quad (2)$$

Here we assume saturated water and only vertical steam velocity.

In the experiment we use air as steam simulant. In order to achieve similar conditions for particulate spreading we normalize the superficial velocity v_{gas} to the corresponding

minimum fluidization velocity of the debris bed u_{mf}^{gas}. The u_{mf}^{gas} is independent of the geometry and dimensions of the bed. We estimate the u_{mf}^{air} and u_{mf}^{steam} at atmospheric pressure conditions assuming identical properties of the coolant and debris bed particles. The u_{mf} can be calculated as:

$$u_{mf} = \frac{\mu_g \cdot Re_{mf}}{\rho_g \cdot d_p}, \quad (3)$$

where μ_g is the dynamic viscosity of the flowing gas and the Reynolds number Re_{mf} for the three-phase fluidization [9]:

$$Re_{mf} = \sqrt{33.7^2 + 0.0406 \cdot Ar_{lg}} - 33.7, \quad (4)$$

where the gas-phase Archimedes number with liquid-buoyed solids is

$$Ar_{lg} = \rho_g \cdot (\rho_p - \rho_c) \cdot g \cdot d_p^3 / \mu_g^2. \quad (5)$$

Due to higher gas density, the bed fluidization by air requires lower injection velocities than for the steam. Results of calculations of minimum fluidization velocity are presented in Table 14 for spherical particles with diameters of $d_p = 3.43$ mm (corresponds to 3x3 mm stainless steel (SS) cylinders used in PDS tests), particle material and coolant densities $\rho_p = 8000$ kg/m^3, $\rho_c = 1000$ kg/m^3 respectively. Eq. (3) suggests that in our laboratory conditions we can fluidize the debris bed by air flow at 2.6 m/s.

Table 14: Minimum bed fluidization velocities by air and steam for the stainless steel 3x3 mm in size cylindrical particles.

Gas	$\boldsymbol{\rho_g}$ (kg/m^3)	$\boldsymbol{\mu_g}$ (Pa·s)	$\boldsymbol{u_{mf}}$ (m/s)
Water steam	0.590	$1.2 \cdot 10^{-5}$	3.78
Air	1.225	$1.85 \cdot 10^{-5}$	2.61

Normalizing steam velocity $v_{steam}(h)$ with respect to minimum fluidization steam velocity we get:

$$\frac{v_{steam}(h)}{u_{mf}^{steam}} = \frac{\rho_p \cdot (1-\varepsilon) \cdot W \cdot d_p}{H_e \cdot \mu_g \cdot Re_{mf}} \cdot h \equiv \frac{\rho_p \cdot (1-\varepsilon) \cdot W \cdot d_p \cdot \tan\theta}{H_e \cdot \mu_g \cdot Re_{mf}} \cdot L. \quad (6)$$

The superficial velocity of the injected air in our PDS laboratory tests can be scaled down from the superficial velocity of generated steam in SA conditions according to the following (see Table 14):

$$v_{air} = \frac{u_{mf}^{air}}{u_{mf}^{steam}} \cdot v_{steam} \cong 0.69 \cdot v_{steam}. \quad (7)$$

Normalized superficial steam velocity as a function of bed's length and height is plotted in Figure 40 for different particle size and bed porosities. As it can be seen in Figure 40a, with small 1 mm particles the bed is fluidized at the top, while for larger particles and the same gas velocity fluidization limit is not reached (Figure 40b).

The green and blue points in Figure 40 represent the normalized gas velocities achievable in PDS-2 and PDS-C facilities respectively. PDS-2 facility can be used to simulate particulate debris spreading with prototypic steam flow rate in the vicinity of the debris bed leading edge. PDS-C facility can provide high gas flow rate typical for a top part of a tall debris bed go up to fluidization limit.

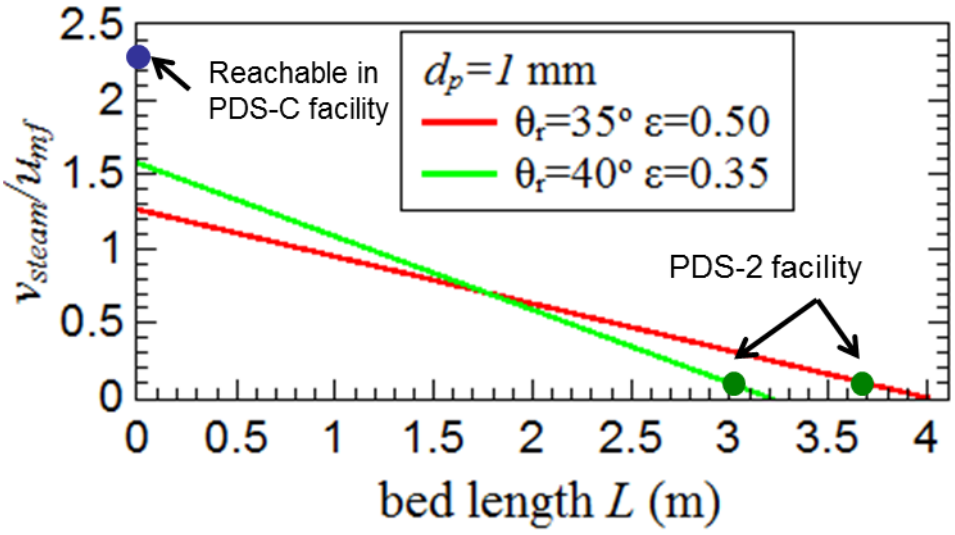

a)

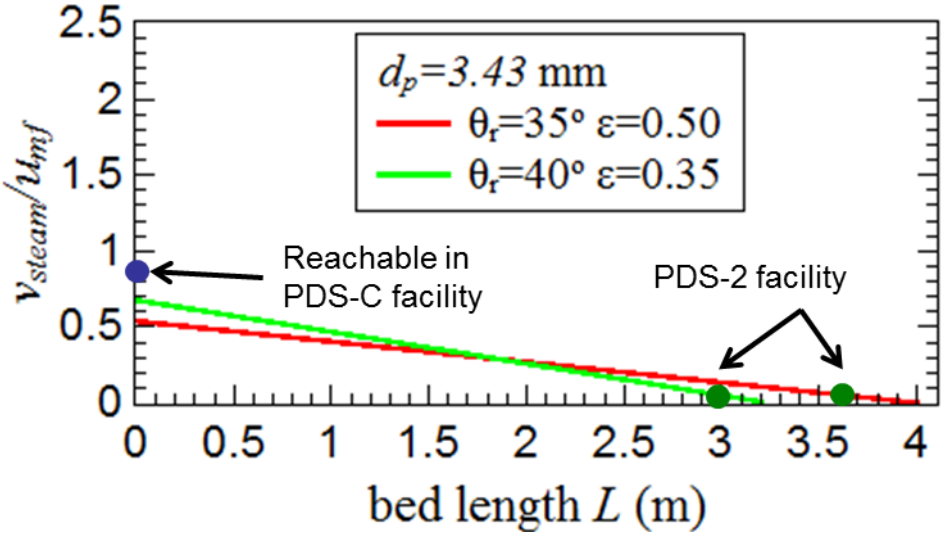

b)

Figure 40: Normalized superficial velocity of the steam as function of debris bed length with particles of different sizes: a) for 1 mm particles; b) for 3.43 mm particles. The green and blue points show air velocities reachable in PDS-2 and PDS-C facilities respectively.

Title	Investigation of debris bed formation, spreading and coolability
Author(s)	Pavel Kudinov, Alexander Konovalenko, Dmitry Grishchenko, Sergey Yakush, Simone Basso, Nazar Lubchenko, Aram Karbojian
Affiliation(s)	Division of Nuclear Power Safety, Royal Institute of Technology, KTH, Sweden
ISBN	978-87-7893-362-1
Date	August 2013
Project	NKS-R / DECOSE
No. of pages	88
No. of tables	14
No. of illustrations	40
No. of references	70

Abstract

The work is motivated by the severe accident management strategy adopted in Nordic type BWRs. It is assumed that core melt ejected from the vessel will fragment, quench and form a coolable debris bed in a deep water pool below the vessel. In this work we consider phenomena relevant to the debris bed formation and coolability.

Several DEFOR-A (Debris Bed Formation – Agglomeration) tests have been carried out with new corium melt material and a melt releasing nozzle mockup. The influence of the melt material, melt superheat, jet free fall height on the (i) faction of agglomerated debris, (ii) particle size distribution, (iii) ablation/plugging of the nozzle mockup has been addressed.

Results of the DECOSIM (Debris Coolability Simulator) code validation against available COOLOCE data are presented in the report. The dependence of DHF on system pressure from COOLOCE experiments can be reproduced quite accurately if either the effective particle diameter or debris bed porosity is increased. For a cylindrical debris bed, good agreement is achieved in DECOSIM simulations for the particle diameter 0.89 mm and porosity 0.4. The results obtained are consistent with MEWA simulation where larger particle diameters and porosities were found to be necessary to reproduce the experimental data on DHF. It is instructive to note that results of DHF prediction are in better agreement with POMECO-HT data obtained for the same particles. It is concluded that further clarification of the discrepancies between different experiments and model predictions.

In total 13 exploratory tests were carried out in PDS (particulate debris spreading) facility to clarify potential influence of the COOLOCE (VTT) facility heaters and TCs on particle self-leveling process. Results of the preliminary analysis suggest that there is no significant influence of the pins on self-leveling, at least for the air superficial velocities ranging from 0.17 up to 0.52 m/s. Further confirmatory tests might be needed at lower gas injection rates.

Key words Severe accident, Nordic BWR, debris bed formation, debris bed coolability

Available on request from the NKS Secretariat, P.O.Box 49, DK-4000 Roskilde, Denmark.
Phone (+45) 4677 4041, e-mail nks@nks.org, www.nks.org